Master Thesis

Studies on dark rates induced by radioactive decays of the multi-PMT digital optical module for future IceCube extensions

Supervisor:
Prof. Dr. Alexander Kappes

Second examiner:
Dr. Carlos Guerrero Sánchez

A thesis submitted in fulfilment of the requirements for the degree of

Master of Science *at* Westfälische Wilhelms-Universität Münster
and
Máster Interuniversitario en Física Nuclear *at* Universidad de Sevilla

by

Martin Antonio Unland Elorrieta

AG Kappes
Institut für Kernphysik

Münster, December 2017

Declaration of Academic Integrity

I hereby confirm that this thesis on "Studies on dark rates induced by radioactive decays of the multi-PMT digital optical module for future IceCube extensions" is solely my own work and that I have used no sources or aids other than the ones stated. All passages in my thesis for which other sources, including electronic media, have been used, be it direct quotes or content references, have been acknowledged as such and the sources cited.

Münster, 28 December 2017 _____

I agree to have my thesis checked in order to rule out potential similarities with other works and to have my thesis stored in a database for this purpose.

Münster, 28 December 2017 _____

"*Every thesis should have a quote...*"

Raffaela Solveig Busse

Contents

1 Introduction

Since the beginnings of humankind, the fascination with the universe has been the main driver for learning about nature and its laws. The motion of the stars and their patterns influenced peoples life enormously for thousands of years, keeping the track of seasons and time. The science of astronomy took a gigantic leap forward with the invention of the optical telescope in the 1600s century, which enabled the systematic study of the universe.

In the last century, astronomy across the electromagnetic spectrum - ranging from gamma-ray satellites to radio observatories - has established itself as a solid tool for studying objects of our universe. However, with the discovery of cosmic rays and the development of the Standard Model, we became aware that not only photons can be a source of seemingly unlimited knowledge. In this context, with the recent detection at LIGO and VIRGO of the gravitational wave GW170814, the product of two merging black holes [1], the era of multi-messenger astronomy has officially begun.

Nevertheless, one of the first milestones of multi-messenger astronomy can be traced back to exactly two decades ago: the detection of several neutrinos at the Kamiokande-II, IMB and Baksan neutrino observatories from SN1987A - a supernova so close to earth that it was easily visible to the naked eye [2].

Neutrinos are ideal messengers of galactic events since they are produced in many different processes and they can travel almost freely through the universe. However, although their low interaction probability constitutes their biggest advantage as cosmic messengers, it also makes their detection a very difficult task. Nevertheless, scientists have taken on the challenge and various large-volume neutrino detectors have been built across the earth. IceCube, currently the biggest among them, is the first cubic kilometre sized neutrino observatory and it was designed to detect high energy neutrinos from astrophysical sources. It is located deep in the glacial ice at the South Pole, where several strings with optical sensors are deployed - the "eyes" of the detector.

IceCube is in full operation since 2011 and it has already discovered a flux of high-energy neutrinos of cosmic origin with energies up to $\mathcal{O}$(PeV) [3, 4], making it the first experiment to prove the feasibility of neutrino astronomy. This provides the motivation for new IceCube extensions that will dramatically boost IceCube's performance. In this context, new concepts are being considered for the optical sensors that will be deployed in these upgrades, taking advantage of the advances in technology and the knowledge gained through the years of IceCube's operation. One novel concept is the multi-PMT Digital Optical Module, or short mDOM. This module includes an array of small-size photomultipliers inside a pressure vessel, instead of housing a single larger one, like in the current IceCube modules.

As the deep ice at the South Pole is almost free of optical activity, the light produced by the modules themselves represents the dominant background source. Therefore, a very important aspect of the development of the mDOM is to understand this noise to estimate the overall background of the detector and its influence on the signal processing of real events. In this regard, two important light sources are Cherenkov and scintillation photons produced by radioactive decays inside the module's pressure vessel. The former, Cherenkov radiation, has already been studied in the framework of a Bachelor thesis considering ^{40}K decays [5], an important source of Cherenkov light inside the vessels. However, it did not completely explain the observed background. Investigations on the luminescence produced by these decays have been limited, although studies have already shown its influence on pressure spheres of the AMANDA experiment [6, 7]. This thesis aims to contribute to the understanding and characterisation of these background processes and their impact on the mDOM performance.

Part I

Basics

2 Neutrino astronomy

This chapter provides a brief introduction to the detection of high-energy neutrinos with the IceCube Observatory. This detector is part of the rapidly-developing neutrino astronomy, therefore the next section will present one of the main motivations for this investigation field.

2.1 The cosmic ray riddle

At the beginning of the 20th century, Victor Hess discovered that the Earth is constantly being bombarded by charged particles, the **cosmic rays**. Ever since, the energy and composition of this flux have been measured with precision and today are known in great detail. They are ionised nuclei, being about 90 % protons, 9 % α-particles and the rest heavier nuclei [8 (p. 6)]. Their most outstanding feature is their high-energy, as the spectrum of these particles spans several orders of magnitude and events with energies from $\sim 10\,\mathrm{GeV}$ up to $\mathcal{O}(\mathrm{EeV})$ have been observed [8 (p. 12)].

Despite the vast studies done with cosmic rays, the origin and production mechanism of these particles remains unclear. In this context, several models that could explain the observed phenomena have been proposed and can be classified into two classes. A **top-down** scenario assumes that cosmic rays are decay products of heavy remnants of the early universe, such as topological defects or dark matter particles. These models, however, have recently been essentially excluded due to constraints from experimental observations [9]. In contrast, **bottom-up** theories suggest that low-energy charged particles are gradually accelerated to the observed energies. In this regard, various potential accelerating galactic and extra-galactic objects have been suggested.

A promising source in the galactic region are **SuperNove Remnants** (SNR). After the detonation of a supernova, a shock wave of the star's material is released at enormous velocities into the interstellar medium. This provides the necessary conditions for the acceleration of cosmic rays. Indeed, based on their energy release, SNRs are thought to be the main galactic source of cosmic rays. On the other side, the charged particles with the highest energies are considered to be accelerated outside the Milky Way. A candidate for the acceleration of this extra-galactic component are **Active Galactic Nuclei** (AGN). AGNs are compact regions in the centre of a galaxy, source of extremely intense electromagnetic radiation. This radiation is believed to be caused by a supermassive black hole surrounded by a dense accretion disc, from which mass is drawn. The most distinctive feature of AGNs is, however, the two jets of extremely relativistic matter emitted perpendicular to the accretion disk. In these jets, shock waves propagate, which are assumed to efficiently accelerate particles to very high energies [10].

Nevertheless, a definitive identification of the source of cosmic rays is impeded by the fact that as particles propagate from the acceleration zone, they are deflected by intergalactic magnetic fields. Therefore, the directional information of the particles is

lost before they arrive on Earth. To identify the sources, it is necessary to study the neutral component of cosmic rays. As the charged particle is being accelerated, they can interact hadronically with the surrounding matter, producing neutrinos and γ-rays. These daughter particles feature also very high energies, as their energy spectrum is expected to follow that of the cosmic rays.

In the case of γ-rays, their use for the search of extra-galactic sources is limited, as their mean free path is restricted by their interaction with the interstellar medium and the cosmic microwave background. For galactic sources, these effects start to be prominent for rays with energies over 100 TeV [11]. Nevertheless, with the increasing technical capabilities, neutrino astronomy has become plausible and an increasingly important tool in the exploration of the source of cosmic radiation. The next section introduces the fundamental properties of this particle and the mechanisms used in the neutrino astronomy for its detection.

2.2 Neutrino properties and interactions

Neutrinos are elementary particles included in the lepton family and thus an integral part of the Standard Model of particle physics. They are quasi-massless[1], do not possess electrical charge and being leptons, they do not undergo strong interactions. Thus, neutrinos can only interact through the weak force.

These particles come in three flavours: electron, muon and tau neutrinos, corresponding to the three charged leptons. A variety of experiments in recent decades have proven that the neutrino lepton flavour is not conserved since the flavour of a neutrino flux can partially change after propagation in vacuum or matter. This process is referred to as neutrino oscillation. Until now, the only consistent explanation for this property is a nonzero neutrino mass, opposed as initially considered in the Standard Model [12].

The neutrino properties make their direct detection impossible and it has to be carried out via charged secondary particles produced through interactions. At high energies (>10 GeV), these interactions are dominated by deep inelastic scattering with nucleons. Depending on the exchanged boson, there are two branches in which neutrinos will engage - the neutral current (exchange of a Z^0) or the charged current (exchange of a $W^{\pm}$):

$$\nu_l + N \xrightarrow{Z^0} \nu_l + X, \qquad \nu_l + N \xrightarrow{W^{\pm}} l + X, \tag{2.1}$$

where ν_l represents a neutrino (or an antineutrino) with the lepton flavour l, N denotes a nucleon (proton or neutron), l the emitted lepton (or antilepton) and X represents the additional rest products of the interaction, which can be one or more hadronic particles. In equation 2.1 the lepton flavour is strictly conserved, which may seem conflicting with the aforementioned neutrino oscillation. It has to be emphasised that the flavour change is a consequence of the flavour mixture of mass eigenstates after propagation. The violation of the lepton flavour number in an interaction implies CPT symmetry breaking [13], a violation that at this time has not been confirmed by experiments [14].

As neutrinos posses a very small cross-section, they rarely interact with matter. Therefore, large interaction volumes are needed for the detection of a sufficient number of these

[1] Although the neutrino mass is not exactly known, they are so light that the gravitational force can be neglected in their interactions.

particles. This is especially true for naturally occurring neutrinos, like the neutrinos from astrophysical sources, since their flux is quite low compared to, e.g. neutrinos produced in reactors.

2.3 Detection of high-energy neutrinos via Cherenkov radiation

As we already saw, neutrinos cannot be measured directly. The charged secondary particles emitted in interactions such as the ones in the equation 2.1 can, however, be detected by different techniques. The most widespread method involves detection via the Cherenkov effect, which is used, e.g. for the detection of high-energy neutrinos in large-volume neutrino telescopes such as ANTARES, BDUNT, NESTOR and IceCube [15, 16, 17, 18]. This effect will be explained in this section. Nevertheless, depending on the energy range and the issue of study, other techniques have been used, such as radiochemical methods(e.g. the GALLEX/GNO and SAGE experiments [19]), tracking calorimeters (MINOS, NOνA [20]) and radio detectors (ANITA, RICE, ARA [21, 22, 23]).

The Cherenkov effect takes place when a charged particle passes through a dielectric at speeds greater than the phase velocity of light in that medium. The electric field of the particle polarises the medium (small displacements undergone by a vast number of electrons) and on the de-excitation of the electrons (return to their normal position), radiation is emitted. If the charged particle is slower than the phase velocity of this radiation, the emission interferes destructively. If this is not the case, i.e. it is faster than light in the medium and the wavelets of the track are in phase overlapping constructively on a wavefront, causing the coherent emission of photons [24]. A sketch of this process is shown in figure 2.1. The Cherenkov radiation is released in the form of a cone with an opening angle θ relative to the particle's trajectory. This angle is defined by the velocity of the wavefronts $v_w = \frac{c}{n}$, which depends on the refractive index of the medium n, and the velocity of the charged particle $v_p = \beta \cdot c$, where β is the ratio of v_p to the speed of light c. Following figure 2.1 this angle is given by:

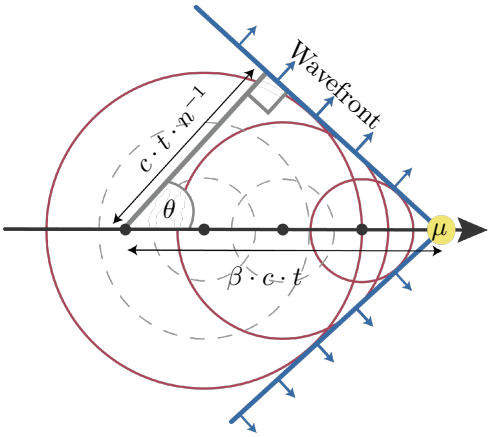

Fig. 2.1: Schematic of Cherenkov radiation, in this case, being emitted by a muon μ.

$$\cos(\theta) = \frac{c \cdot t \cdot n^{-1}}{\beta \cdot c \cdot t} = \frac{1}{\beta \cdot n}. \tag{2.2}$$

Employing the condition for the Cherenkov effect $\beta > n^{-1}$, we can directly determine the minimal kinetic energy E_{th} of a charged particle for the production of Cherenkov light as follows:

$$E_{\text{kin}} = (\gamma - 1) m_0 c^2 = m_0 c^2 \left(\frac{1}{\sqrt{1-\beta^2}} - 1\right) > E_{\text{th}} = m_0 c^2 \left(\frac{1}{\sqrt{1-n^{-2}}} - 1\right) = m_0 c^2 \left(\sqrt{\frac{n^2}{n^2-1}} - 1\right), \tag{2.3}$$

where m_0 is the invariant mass of the particle and $\gamma = \frac{1}{\sqrt{1-\beta^2}}$ is the Lorentz factor. Hence, the energy threshold only depends on the refractive index of the medium. After inserting the characteristic index for ice $n = 1.31$, the needed kinetic energy will be $\sim 55\,\%$ of its rest energy. For larger refractive indices, this energy threshold gets lower, as for a typical glass, with $n = 1.48$, only $\sim 36\,\%$ of the particle's rest energy is necessary. For an electron, this results in $\sim 0.28\,\mathrm{MeV}$ and $\sim 0.18\,\mathrm{MeV}$, respectively.

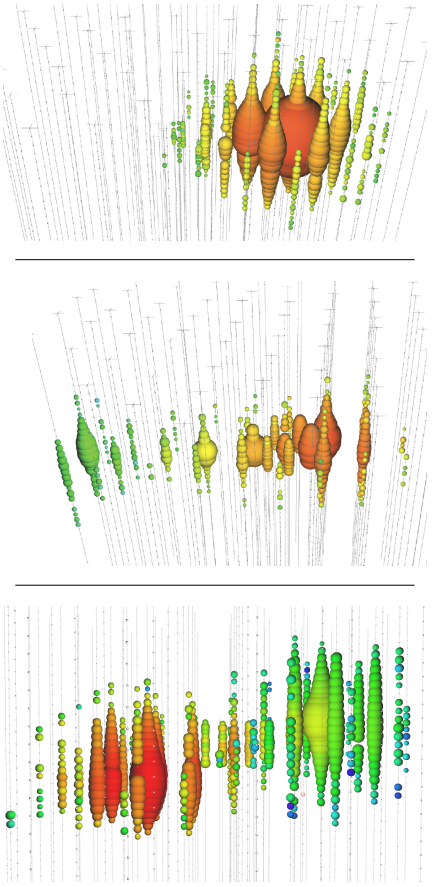

Fig. 2.2: Light deposition signatures of showers (top), track (middle) and double-bang events (bottom). The colour indicates the arrival time of the photos, going from red (early) to blue (later), while the size of the spheres illustrates the amount of detected light. Figures taken from the IceCube MasterClass `https://goo.gl/jXorcb`.

The spectrum of the emission and the number of photons radiated per unit length can be approximated by the Frank-Tamm formula [25]

$$\frac{d^2N}{dxd\lambda} = \frac{2\pi\alpha}{\lambda^2} \cdot \left(1 - \frac{1}{\beta^2 n(\lambda)^2}\right),$$

where N is the number of emitted photons and $\alpha \approx \frac{1}{137.04}$ is the fine structure constant. It is noteworthy that the emission spectrum, in the first order, is proportional to λ^{-2}, although there is a small dependence on the refractive index of the medium $n(\lambda)$. By recording the number of emitted photons and its time distribution, different light patterns can be identified, with which it is possible to reconstruct the energy and the direction of the charged particle.

The light signatures produced by leptons after a charged current neutrino interaction are reasonably distinctive depending on their flavour as their lifetime and probability of interaction vary. These signatures start at the interaction vertex, where a hadronic cascade, originating from the debris of the hit nucleon, takes place; this produces a near-spherical mark. Electrons or positrons travel very short distances as electromagnetic cascades are quickly generated as a result of scattering in the medium, bremsstrahlung and pair production. Altogether, their signatures resemble a point source with maximum photon production in the centre and are called **showers**. In contrast, highly energetic muons can travel very long distances before they decay or are stopped and thus produce a **track**-like signature. Tau neutrinos will emit a tauon, which, after a short distance, decays via weak interaction into a muon, electron or producing light mesons. These particles will create an electromagnetic or a hadronic cascade, respectively. As spherical light emission is produced by both cascades, the hadronic cascade at the interaction vertex and the one originated from the tau decay, the signature is referred as a **double-bang**. An example of these three signatures can be seen in figure 2.2.

A shower signature is also created by all neutrino flavours undergoing a neutral current interaction, as it only induces a hadronic cascade. The energy of the neutrino can be well reconstructed from the total light deposition with these kinds of signatures as all

the energy is deposited inside of a relatively small volume. However, owing to its almost spherical shape, the direction reconstruction is limited to only the time information. Track signatures, on the other side, allow for very precise directional reconstruction, although to derive the initial energy of the neutrino accurately, the interaction vertex has to be measured within the detector.

The IceCube Observatory uses this method for the detection of neutrinos. In the next section, different parts of this detector and its main features are discussed.

2.4 The IceCube Neutrino Observatory

IceCube is the first kilometre-scale neutrino detector and is located at the South Pole, starting at 1450 metres below the surface, with a total of 5160 optical sensors for detecting the Cherenkov light produced by particle interactions [18]. A sketch of the Observatory is shown in figure 2.3. The primary array consists of 78 strings (cables) with a length of 1 km distributed over a square kilometre, each holding 60 digital optical modules (DOMs) in 17 m vertical intervals. The horizontal inter-string distance is 125 m, which allows the investigation of neutrinos in an energy range between 100 GeV and $\mathcal{O}$(PeV). The DOMs incorporate a 10-inch-diameter photomultiplier tube (PMT) facing down, inside a glass pressure vessel, with circuit boards that allow near-autonomous operation. PMTs are extremely sensitive devices that are capable of measuring single photons. These are described later in this thesis in chapter 3.

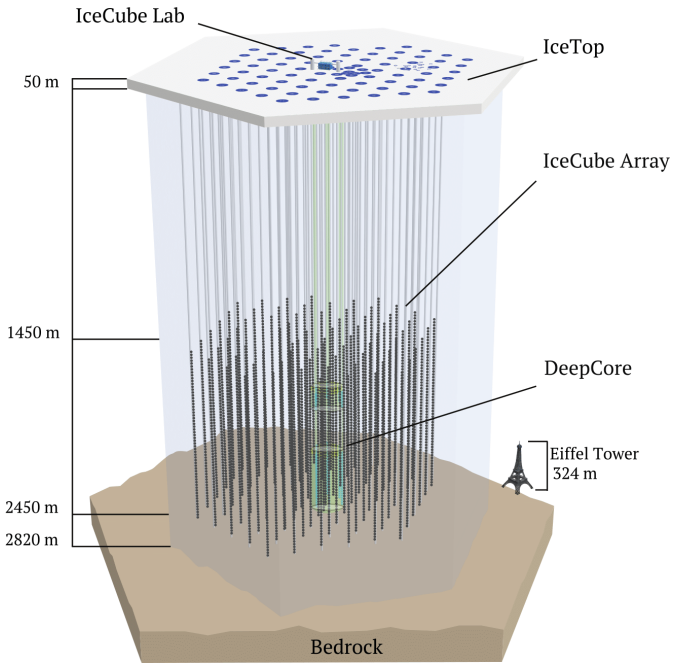

Fig. 2.3: Diagram of the IceCube Observatory at the South Pole. Figure courtesy of the IceCube Collaboration.

Eight additional strings separated, on average, by about 72 m are located at the centre of the detector. The modules are deployed at depths ranging from 2100 m to 2450 m, with an inter-sensor spacing of only 7 m. This more densely instrumented sub-detector is called *DeepCore* and is optimised to detect neutrinos of energies in the order of tens of GeV.

On the surface is located *IceTop*, which consists of water tanks near the top of each string, with two DOMs each, forming a square kilometre air shower array. This can be used as a veto against atmospheric neutrinos and as a detector for cosmic rays in the 300 TeV to 1 EeV region. All the cables from the detector are routed to the IceCube Laboratory, which is the operation building of the detector located at the surface in the centre of the array.

The IceCube's commissioning was completed 2011 and since then it has already discovered a flux of high-energy neutrinos of cosmic origin [3]. An overview of the recent

findings of IceCube with regard to astrophysical neutrinos and cosmic rays can be found in [26]. Nevertheless, the modest number of events limits the efficiency of this observatory. Therefore, a substantial expansion of the detector is sought, *IceCube-Gen2*, aiming at an instrumentation of up to 10 km^3 of glacial ice with novel technology [27].

2.4.1 IceCube-Gen2

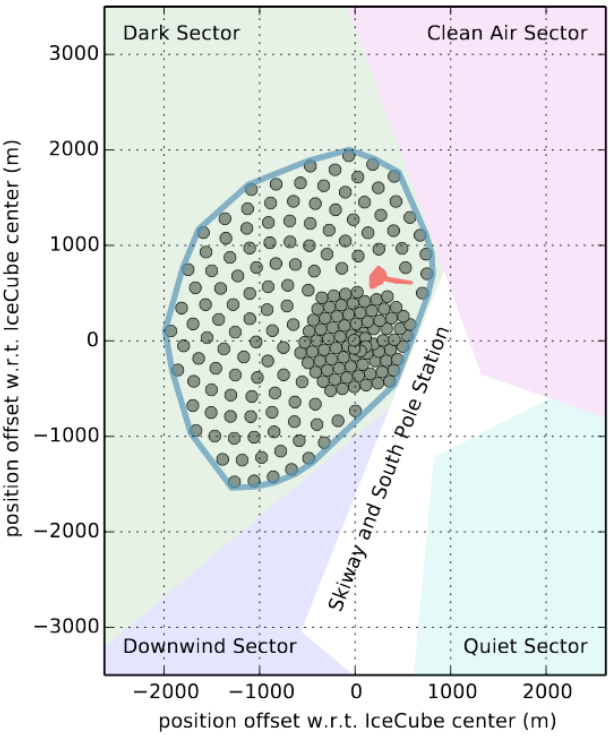

Fig. 2.4: Benchmark detector string layout with a string-to-string distance of about $\sim$ 240 m. The new 120 strings surround the more densely instrumented IceCube detector. Other geometries and sets of spacing are under consideration. Figure taken from [27].

The benchmark detector layout for IceCube-Gen2 considers the extension of 120 new strings, aiming for the detection of high-energy neutrinos, sometimes called *HEA* (High-Energy Array)[27].

Following the calibration and the building of IceCube, the optical properties of the glacial ice are now known in detail over a range of great depth. The absorption length of the ice for Cherenkov light is larger than initially assumed and exceeds 100 m-200 m, depending on the depth. This enables the instrumentation of considerably larger volumes with lower string densities than observed at IceCube. In this context, spacings between 240 m and 300 m are being considered. An example string layout is illustrated in figure 2.4. The larger spacing results in a higher energy threshold above $\sim$ 50 TeV, but it does not represent a loss of astrophysical neutrino signal. Owing to the size of the detector, the HEA should be capable of measuring neutrinos up to the $\mathcal{O}$(EeV) level.

Besides the HEA, an extension of DeepCore is being proposed: *PINGU*, a dense array for the detection of low-energy neutrinos, which will target precision measurements of the atmospheric oscillation parameters and the neutrino mass hierarchy [27]. An expansion of the IceTop array is also considered in the scope of IceCube-Gen2.

The detector sensitivities for neutrino point sources scale approximately with the square-root of the increase in its cross-sectional area, but linearly with the angular resolution. The latter can be further improved with different approaches, e.g. advanced reconstruction methods and a more detailed model of the ice properties. In this respect, new optical sensors are being proposed, which will increase not only the angular resolution but also the overall efficiency.

Two new concepts for optical sensors are being studied. On the one hand, the employment of wavelength-shifting and light-guiding techniques for an increased sensitivity to UV photons and hence the Cherenkov spectrum is represented by the WOM project

(Wavelength-shifting Optical Module) [28]. On the other hand, the segmentation of the active area of the modules using several PMTs is being investigated. There are two approaches for this: the DEgg, which consist of two 8" PMTs facing downwards and upwards [29] and the mDOM (multi-PMT Digital Optical Module), which features multiple small photomultiplier tubes [30]. A more detailed introduction to the latter is presented in the next section.

2.4.2 The multi-PMT digital optical module

The mDOM consists of 24 3-inch-diameter PMTs facing multiple directions, as illustrated in figure 2.5. In contrast, the current IceCube DOM is shown in figure 2.6. The mDOM PMTs are mounted surrounded by a reflector, which increases the sensitive area of the module [31 (p. 160)], on a 3D-printed holding structure. An active base is attached to the end of the PMT and provides the latter with high-voltage and reads out its output. The signals are digitised by the mainboard, located in the equatorial plane at the centre of the module. All these components are enclosed by a glass pressure vessel that protects the module against rough external conditions. Between the vessel and the internal components of the module, there is a layer of optical gel, which acts as an optical coupler, thereby preventing light reflections due to the different refractive indices of glass and air.

The segmentation of the sensitive area results in a range of advantages in comparison to the conventional single-PMT DOM, such as:

- a larger effective area (hypothetical geometrical area of the module assuming 100 % detection efficiency), since 24 3-inch PMTs provide a larger total photocathode surface than one 10-inch PMT. Moreover, the mDOM has a near homogeneous 4π angular acceptance in contrast with the DOM, where the sensitivity for the downward light is almost zero.
- intrinsic directional sensitivity, as the PMT orientation entails information about the direction of the detected light. In the case of the DOM, this is very limited due to the large field of view of its PMT.
- better photon-counting, as the photons are detected among the different PMTs, their numbers and arriving times can be reconstructed more easily, unlike a multi-photon waveform from a single photomultiplier. Consequently, multiple PMTs also feature a better performance with regard to saturation.

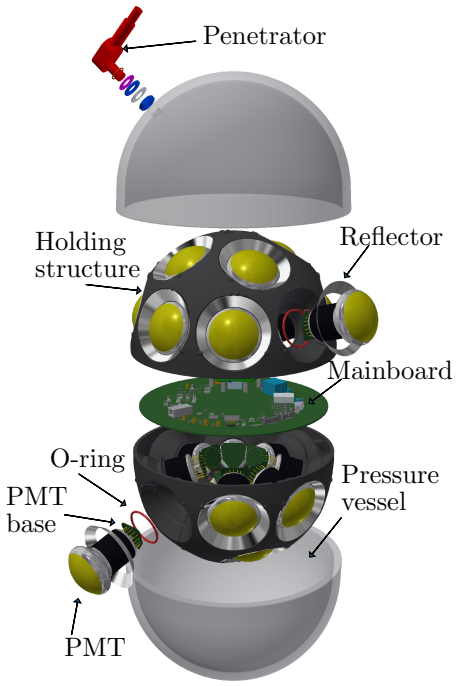

Fig. 2.5: Explosion view of the mDOM with its main components. Courtesy of the IceCube Collaboration.

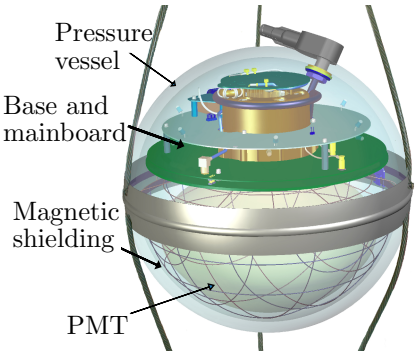

Fig. 2.6: Rendering of the current IceCube DOM. Courtesy of the IceCube Collaboration.

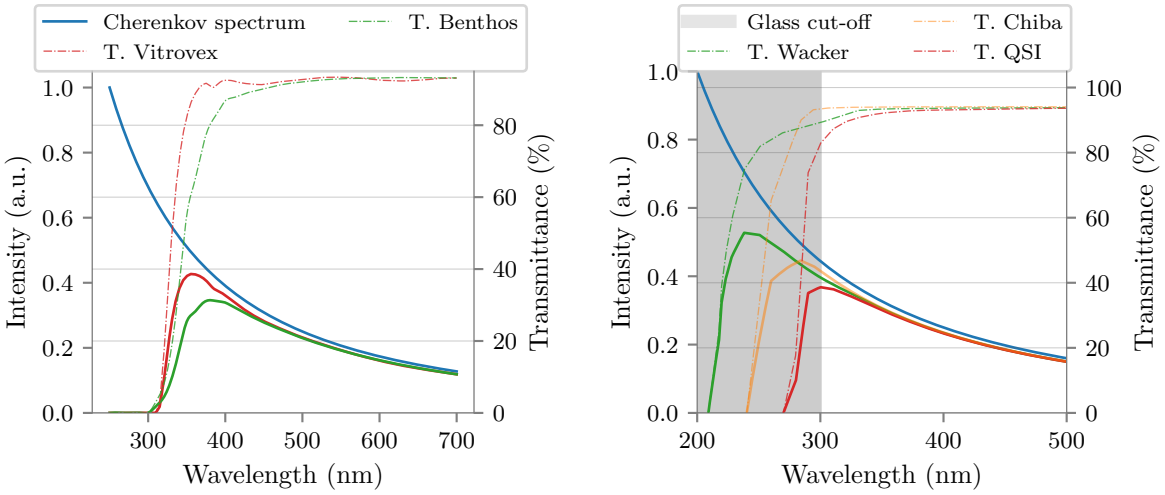

Fig. 2.7: Left: Wavelength dependence of the transmittance of the glass brand Vitrovex and Benthos in dashed lines. The unmodified and the transmitted Cherenkov spectrum is shown with solid lines. **Right:** Wavelength dependence of the transmittance of light of the gel brand Wacker, Chiba and QSI are shown in dashed lines. The unmodified and the transmitted Cherenkov spectrum are shown with solid lines. The grey region represents the range, where there is no light transmission due to the absorption of the glass vessel.

• the possibility for the development of reconstruction algorithms based on local coincidences, i.e. correlated signals in several PMTs from a single module. This enables novel methods for background suppression, PMT self-calibration [31 (p. 215)] and a higher efficiency and better reconstruction of low-energetic signals, such as supernova neutrinos, as shown in recent studies [32].

Aside from the technological improvements being made with the active constituents of the module, the optical properties of the passive components can also be enhanced. From this perspective, alternative brands for the vessel glass and the optical gel are being considered.

The main function of the pressure vessel is to endure pressures up to 700 bar. Owing to the temperature gradient of the glacier, the water freezes from the top downwards, resulting in a high-pressure excess of up to 690 bar [18]. Consequently, the vessel has to be quite thick (over 1 cm at the current DOM), which makes the transparency of the material very important as a portion of the light will be absorbed in it. The current operating neutrino telescopes use vessels made of borosilicate glass. The transmission spectrum of this material exhibits a wavelength cutoff at around 300 nm, depending on the glass thickness and the manufacturer. In this respect, the Vitrovex brand, the standard glass used by Nautilus GmbH., presents an improved transmission in the UV region compared to the one currently used in the DOMs called Benthos, as illustrated in figure 2.7. For the mDOM's vessel, which has a wall-thickness of 13 mm, this difference results in $\sim 13\,\%$ more Cherenkov photons, in the range of 300 nm to 700 nm, being detected.

The silicon-based optical gels tend to feature better transparency in the UV range, reducing their influence on the overall performance of the module compared to the glass. Nevertheless, brands offering higher transmittance to the gel currently used in IceCube (QGel 900 from QSI) are being considered for the mDOM, such as SilGel 612 from Wacker and the optical gel produced in Chiba, Japan, for the DEgg module. Their transmission at

5 mm[2] thickness is shown in figure 2.7. As the transmission cutoff of the glass is located at larger wavelengths than the one of the gels, the difference regarding the number of transmitted photons in the interval between 300 nm and 700 nm is of only a few percentage points.

However, while aiming to choose the best material, there are other factors to be taken into account. Different brands exhibit various levels of trace radiation, which is an important aspect of the measured background, as decay products can produce Cherenkov light as well as scintillation photons. This thesis focuses on this topic and investigates the influence of the radioactive isotopes presented in the material on the overall noise of the mDOM and DOM, since a detailed understanding of background production mechanisms is crucial for the signal processing and reconstruction. In this context, both glass brands, Benthos and Vitrovex, and the QSI QGel 900 and Wacker SilGel 612 gel are investigated[3]. The optical gel used in Chiba was unfortunately not available for measurements.

[2]The thickness of the gel-layer in front of the PMT varies between 2 mm and 25 mm depending on the location.

[3]Hereinafter in this work, the optical gels QGel 900 and SilGel 612 will be referred to by the name of their manufacturers, QSI and Wacker, respectively.

3 Photomultiplier tubes

As seen in the previous sections, the heart of the optical modules is their photomultiplier tubes (PMTs). These devices convert photons into measurable electrical signals and are extremely sensitive. Their amplification process by the emission of secondary electrons enables the detection of single photons.

This section provides a short introduction to these devices as they are key to understanding the measurements performed in this work.

3.1 Construction and operation principle

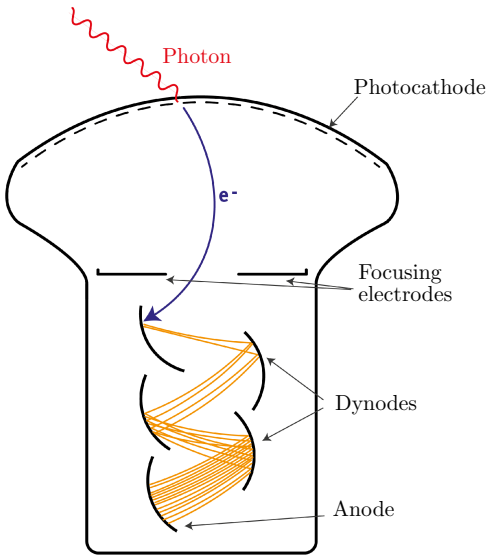

Fig. 3.1: Schematic of a photomultiplier tube with its main constituents. The red sinusoidal line represents a photon that emits a photoelectron (blue line) at the photocathode. The secondary electrons from the dynodes are represented by yellow lines.

Figure 3.1 shows the essential components of a PMT. The first stage of photon detection takes place at the photocathode. This is a thin layer of photosensitive material, which can absorb photons and convert them into electrons (photoelectrons) via the photoelectric effect. These photoelectrons are focused and electrostatically accelerated towards the electron multiplier, which consists of a series of electrodes (dynodes). When an electron strikes a dynode, it liberates secondary electrons, which are then guided towards the next dynode and finally the anode, which delivers the output signal. For this to happen, a high voltage is applied to the cathode, dynodes and anode by a voltage divider. The intensity of this potential demonstrates step-wise change between the different components so that the electrons are always predominantly accelerated towards the next stage.

The electrons that arrive at the anode can be read out directly as a charge or as a voltage signal. In the first case, the charge of the PMT pulses that arrive within a certain time window is integrated by a current-measuring device (e.g. picoammeter), resulting in a current value. This operation mode is called current or analogue mode and is used when the PMT is illuminated with a steady intensity of light, or the time information of individual pulses is not needed.

In pulse or photon-counting mode, the output is supplied to a resistor, which results in a voltage pulse (e.g. employing an oscilloscope). This way single pulses can be analysed by extracting the maximum information from the data, which provides an advantage over the current mode in low-light-intensity measurements.

3.2 Main parameters

Several parameters and properties characterise the performance of a PMT. This section provides an overview of the most relevant PMT features for this thesis. An introduction to this topic can be found in [33] and [34], while PMTs are also covered extensively in the textbook [35].

3.2.1 Quantum efficiency

The **quantum efficiency (QE)** is the number of photoelectrons emitted from the photocathode divided by the number of incident photons. This property is wavelength dependent and is mainly determined by the photocathode material and the optical properties of the PMT entrance window. Photocathodes are compound semiconductors of alkali metals that have a low work function. There are several kinds of materials currently employed, although for this work the relevant ones are bialkali compounds (Sb-Rb-Cs, Sb-K-Cs) [33 (p. 30)]. The standard bialkali exhibits a maximal QE of ∼25 % for wavelengths around 400 nm, but by improving its crystallinity, the QE can be increased to ∼35 % (Super Bialkali, SBA) and over 40 % (Ultra Bialkali, UBA) [36]. Typical QE curves for standard bialkali, SBA and UBA photocathodes are shown in figure 3.2.

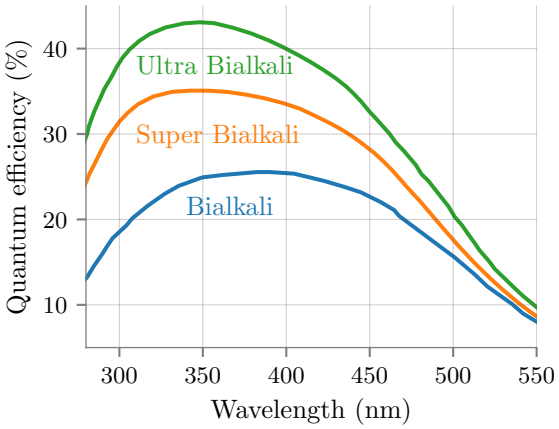

Fig. 3.2: Quantum efficiency of standard bialkali, SBA and UBA with a borosilicate glass entrance window. Data was taken from [36].

Bilalkali photocathodes also feature high sensitivity down in the ultraviolet (UV) region, but this is limited by the transmission of the window material. The windows are most commonly made of borosilicate glass, which exhibits a transmission cutoff at around 300 nm, absorbing photons with wavelengths under this boundary. For an improved QE in the UV range, windows made from, e.g. synthetic silica (cutoff at ∼ 160 nm) or UV glass (cutoff at ∼ 185 nm) can be used [33 (p. 36)].

3.2.2 Gain and collection efficiency

The **gain** g of the PMT is the mean number of electrons measured at the anode after the emission of one photoelectron from the photocathode, and it is the product of the individual dynode contributions. The latter is described by the secondary emission coefficient δ_i, i.e. the average number of electrons emitted by the dynode d_i for every incoming primary. The emission coefficient is directly proportional to the energy of the primary particle (up to a certain energy threshold), which makes the gain a function of the applied voltage. Nonetheless, there are loss processes, which are owing to the multiplier's geometry and positioning of the dynodes, determining the inter-dynode collection efficiency c_i, that is the fraction of electrons that arrive from dynode d_{i-1} to d_i. For the first dynode d_0, it is the ratio between the released photoelectrons at the photocathode and the photoelectrons

that reach this dynode. Hence, the gain can be expressed as follows:

$$g = \prod_{i=1}^{N} \delta_i c_i, \tag{3.1}$$

where N is the total number of dynodes in the multiplier system [34]. Defining the ideal gain as $g_{\text{ideal}} = \prod_{i=1}^{N} \delta_i$, it is also possible to specify a global **collection efficiency** for the PMT CE, where $CE = \frac{g}{g_{\text{ideal}}}$, which is the fraction between the detected and the emitted photoelectrons.

A high gain is usually desired, as this achieves a better signal to noise ratio because the photoelectrons can be distinguished better from the electrical noise. Asides from this, assuming that the processes at all stages of the multiplier obey a Poisson distribution, the relative variance of the output charge will be proportional to $\frac{1}{g}$. Therefore, a higher gain results in a lower variance of the measured charge. This allows a better reconstruction of the number of photons detected at a given time.

3.2.3 Time response

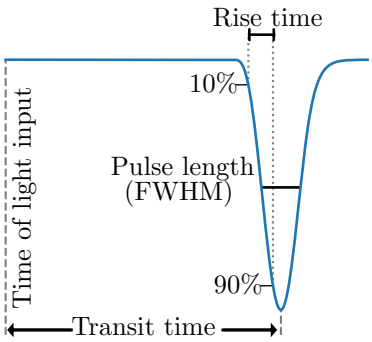

Fig. 3.3: Schematic of the photomultiplier time response parameters.

The output pulse of a PMT can be characterised primarily by three parameters. First, there is the **rise time**, which is defined as the time needed for the pulse to rise from 10 % to 90 % of the peak height (see figure 3.3). Then, there is the **signal length**. This is usually described by the full width at half maximum (FWHM) of the PMT pulse, which is usually about 2.5 times the rise time [34 (p. 2-10)]. The latter is, however, only true in the case of a Dirac delta input. Light input pulses always have a certain width, which lengthens the signal.

The interval between the arrival of a light pulse onto the photocathode and the detection of its signal at the anode is called the **transit time**. This time, which is in the order of several tens of nanoseconds, depends on multiple factors and it fluctuates from pulse to pulse. First, there is a geometric component for this variation, as the primary path lengths between the photocathode and the first dynode are different, depending on the photoelectron's emission location. A second factor stems from the spread of the initial velocities of photoelectrons with respect to their initial energy and direction, which causes different transit times, even for particles emitted from the same point on the photocathode [34 (pp. 4-12)]. This jitter of the pulse is called **transit time spread (TTS)** and is usually defined as the FWHM or the standard deviation of the transit time distribution. The TTS should be kept as low as possible as it determines the time resolution of the photomultiplier.

3.2.4 Dark rate and dark current

A PMT always will produce a measurable signal, even in total darkness. This output is called dark rate in the case of a PMT operated in pulse mode and dark current for a PMT in analogue mode. Depending on the nature of these dark signals, they can be classified

into two categories: random and correlated noise. The origin of this background and their dependence on external factors will be the topic of this section.

Random background:

• **Thermionic emission** is the main source of the discrete component of the background and is caused by the spontaneous emission of electrons, which are collected by the multiplier system as a normal pulse. These electrons are released when their thermal energy surpasses the work function of the photocathode $W_{\text{p-th}}$, which is, in principle, always possible, as the electrons in the photocathode follow Fermi statistics. Consequently, this effect is strongly temperature-dependent, causing more dark signals with increasing temperature. Contrarily, this effect can be strongly suppressed by cooling down the PMT so that at negative temperatures its contribution to the total dark rates/current is negligible. The current density of this process is $\propto T^2 \cdot \exp(-W_{\text{p-th}} \cdot T^{-1})$, where T is the temperature (Richardson's law [34 (p. 3)]).

• **Field emission** is the emission of electrons induced by the electrostatic field between the dynodes due to quantum tunnelling. As this effect does not greatly depend on temperature, it is also called *cold emission*. It does depend on the applied voltage, however, as the current density is $\propto \mathcal{E}^2 \cdot \exp(-W_{\text{d-th}}^{3/2} \cdot \mathcal{E}^{-1})$, where $\mathcal{E}$ represents the electric field strength and $W_{\text{d-th}}$ the work function of the dynodes (Fowler-Nordheim formula [37]). Consequently, this is one of the principal factors that determines a practical limit to the set gain [34 (pp. 3,4)].

• **Leakage current**, also called ohmic leakage, is a steady charge flow originated from non-perfect insulating materials used in the tube. The insulation resistance is in the order of $10^{12}\,\Omega$, meaning that for a PMT with an applied voltage of 1 kV, the leakage current may reach the nanoampere level (Ohm's law) [33 (p. 70)].

• Other effects that contribute to random noise are, e.g. radiation from isotopes inside the tube glass envelope, such as ^{40}K, which produces scintillation and Cherenkov radiation. Aside from this, there are external factors, such as cosmic rays and environmental gamma rays that may be a background source depending on the experimental setup [33 (pp. 70,71)].

Correlated background:

• **Late pulses** may occur several nanoseconds after the initial pulse. These are caused mainly by photoelectrons that backscatter from the first dynode or any supporting metal structure in the vicinity. This backscattering process may be elastic, meaning that the signal is first emitted after the photoelectron hits the dynode again. If the backscattering process is inelastic, the photoelectron releases some of its energy as it backscatters at the dynode, releasing secondary electrons. If the photoelectron is detected upon the second impact, two pulses are detected from only one initial photoelectron. Another source of late pulses include photons emitted by the last dynodes and anodes, which glow under electron bombardment in case of intense signals. In this case, a second pulse is measured after a time equal to the transit time of the PMT [38, 35 (pp. 435-439)].

• **Afterpulses** are signals that can be measured a few microseconds after the initial pulse. Photoelectrons in their path to the dynode system may ionise residual gases or release particles from the electrodes. This positively charged ion is accelerated toward

the photocathode and releases several photoelectrons on impact with it. The duration of this process depends on the ion mass and the size of the PMT [35 (pp. 440-445)].

• **Pre-pulses** arise from electrons released by photons incident on the first dynode after crossing the photocathode without being absorbed. As one dynode multiplication stage is missing, the generated pulses are, depending on the set gain, around a factor 10 smaller than a typical single-photoelectron pulse (SPE) and arrives early by an interval equal to the time normally needed by electrons to hit the first dynode (a few nanoseconds)[35 (p. 438)]. As the photon producing the pre-pulse do not get absorbed at the photocathode, this phenomenon should not be seen strictly as correlated background (unless the PMT gets hit by several photons at the same time) but rather as a feature measurable in investigations of pulse-time distributions, as the one present in section 7.1.3.

3.3 Calibration and the photoelectron spectrum

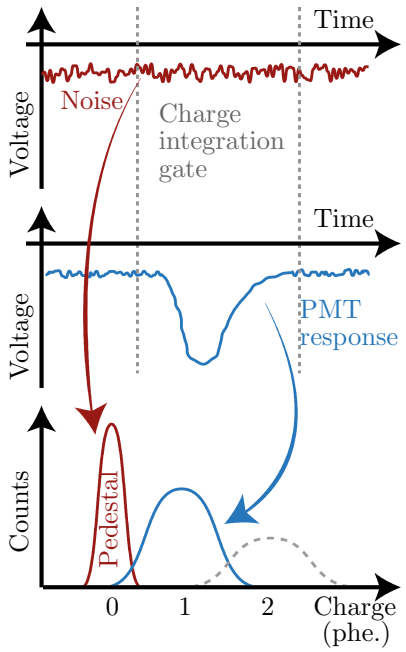

Fig. 3.4: Qualitative sketch of the charge spectrum acquisition procedure. Based on [31 (p. 50)].

Since there is an intrinsic spread between the parameters among different PMTs, it is important to calibrate the used tube, i.e. to know the charge distribution generated by a certain number of photoelectrons. This can be achieved by saving the charge of PMT signals generated by a pulsed light source. The principle is illustrated in figure 3.4 for a PMT operated in pulse mode. The PMT signal is externally triggered by the reference signal of the light source and it is integrated with a constant integration window. The result is a value proportional to the charge of the signal[1]. As the gain is not constant, the distribution of the charge of one photoelectron will have a certain variance (blue line in figure 3.4). If the intensity of the light source is low enough, sometimes no PMT signal will be measured after the trigger, and, therefore, the baseline will be integrated. The distribution of this charge is called the **pedestal** (red curve in figure 3.4).

The calibration is then done by deconvoluting the obtained charge spectrum using a realistic PMT response function. In this work, the method developed by Bellamy et al. [39] is used. Here the response function of the PMT $S_{\text{real}}(q)$ is described as a convolution between an ideal PMT charge distribution $S_{\text{ideal}}(q)$ and a background function $B(q)$:

$$S_{\text{real}}(q) = \int S_{\text{ideal}}(\overline{q}) \cdot B(q - \overline{q})\, \mathrm{d}\overline{q}. \tag{3.2}$$

The ideal response of the PMT S_{ideal} is itself a convolution between the distribution of the number of photoelectrons emitted after one pulse of the light source and a function that describes the response of the dynode system. The number of photoelectrons n released

[1] If the measurement is performed in pulse mode, the integration value has units in Weber and has to be divided by the input resistance of the oscilloscope in order to get the charge of the signal.

after each light pulse is represented by a Poisson distribution $P(n,\mu)$, with the average μ, which depends on the intensity of the light source and the detection efficiency of the PMT. The response of the multiplication system for n photoelectrons can be approximated by a Gaussian distribution $G_n(q)$ with mean nQ_1 and sigma $\sqrt{n}\sigma_1$, where Q_1 is the average charge at the PMT output when one electron is collected, and σ_1 is the corresponding standard deviation of this charge. Thus

$$\begin{aligned} S_{\text{ideal}}(q) &= P(n,\mu) \otimes G_n(q) \\ &= \frac{\mu^n \mathrm{e}^{-\mu}}{n!} \otimes \frac{1}{\sqrt{2\pi n}\sigma_1} \exp(-\frac{(q-nQ_1)^2}{2n\sigma_1^2}) \\ &= \sum_{n=0}^{\infty} \frac{\mu^n \mathrm{e}^{-\mu}}{n!} \frac{1}{\sqrt{2\pi n}\sigma_1} \exp(-\frac{(q-nQ_1)^2}{2n\sigma_1^2}). \end{aligned} \tag{3.3}$$

It is to be noted that this function approaches a delta peak for $n \to 0$ (non-existent pedestal), as no noise is included. The latter is described by the background response function $B(q)$. On the one hand, it represents low charge processes (such as the leakage current) that produce the pedestal, with a Gaussian of standard deviation σ_0. On the other hand, it also describes the additional charge measured in the signal stemming from discrete processes (e.g. thermionic emission and field emission) as an exponential decay with charge constant α^{-1}:

$$B(q) = \frac{(1-\omega)}{\sigma_0\sqrt{2\pi}} \exp(\frac{-q^2}{2\sigma_0^2}) + \omega \cdot \Theta(q) \cdot \alpha \cdot \exp(-\alpha q), \tag{3.4}$$

where ω represents the probability for measuring discrete processes in the signal and $\Theta(q)$ represents the step function.

Solving equation 3.2 results in a rather complex expression that is difficult to be treated as a fitting function. For cases where the discrete background intensity is low, the background of the nonpedestal part of the spectrum can be treated as an effective additional charge $Q_{\text{sh}} = \omega\alpha^{-1}$, which means that the background response function for $n \geq 1$ is reduced to

$$B(q)|_{n\geq 1} = \frac{1}{\sigma_0\sqrt{2\pi}} \exp(\frac{-(q-Q_0-Q_{\text{sh}})^2}{2\sigma_0^2}),$$

where Q_0 is the mean charge of the pedestal. In this case equation 3.2 can be approximated to

$$S_{\text{real}} \approx B(q-Q_0) \cdot \exp(-\mu) + S_{\text{ideal}}(q-Q_0-Q_{\text{sh}})|_{n\geq 1}, \tag{3.5}$$

which is the equation 3.4 modulated by the probability of measuring no photoelectrons $P(0,\mu) = \exp(-\mu)$, describing the pedestal, while the non-pedestal part is represented by the ideal PMT response from equation 3.3 shifted by the pedestal position Q_0 and the mean charge contribution from discrete background processes Q_{sh}.

Once the calibration has been performed, the gain g of the PMT can be derived via

$$g = \frac{Q_1}{e}, \tag{3.6}$$

where e is the elementary charge.

4 Luminescence of semiconductors

Under the term "luminescence" are classified phenomena, which concern the absorption of energy and the subsequent emission of light. This is a very broad topic as it is a property of different materials (gases, such as in gas-discharge lamps, organic and inorganic semiconductors, such as in (O)LEDs and scintillators, etc.) and are produced by different processes (material excitation by photons, called photoluminescence; photons from biochemical reactions known as bioluminescence; the release of absorbed energy on heating the material, thermoluminescence, etc.). This chapter focuses on a general description of the production of light in semiconductors after excitation by high-energetic particles, such as alpha particles and electrons, also known as scintillation.

4.1 Basic mechanism of radiative transitions

Essentially, the photon emission in a luminescence process stems from an electronic transition between an initial state of energy E_i and a final state E_f, where $E_i > E_f$. Assuming an electron population N_i in the state i, the electrons will spontaneously decay from the higher energy level to the lower state with the probability per unit time $A_{\mathrm{i}\to\mathrm{f}}$, thereby emitting a photon with an energy $h\nu = E_i - E_f$[1] with a rate expressed as

$$\dot{N}_\mathrm{i} = -A_{\mathrm{i}\to\mathrm{f}} \cdot N_\mathrm{i} \qquad \to \qquad \frac{dN_\mathrm{i}}{N_\mathrm{i}} = -A_{\mathrm{i}\to\mathrm{f}} \cdot dt. \tag{4.1}$$

The solution of equation 4.1 is an exponential decay

$$N_\mathrm{i}(t) = N_\mathrm{i}(0) \cdot \exp\left(-A_{\mathrm{i}\to\mathrm{f}} \cdot t\right) = N_\mathrm{i}(0) \cdot \exp\left(-t/\tau_{\mathrm{i}\to\mathrm{f}}\right), \tag{4.2}$$

where $N_\mathrm{i}(0)$ is the initial population and $\tau_{\mathrm{i}\to\mathrm{f}} = A^{-1}_{\mathrm{i}\to\mathrm{f}}$ is the lifetime of the transition [40 (p. 210)]. These are general relations for any two-level radiative transitions, such as in the case of atomic spectral lines, where the two energy levels are atomic orbitals.

In a crystal lattice, the electronic energy levels of neighbouring atoms overlap and split due to Pauli's exclusion principle, thereby being condensed into a band structure. The outermost occupied orbital of the atoms forms the valence band (VB), while the lowest unfilled energy band is the conduction band (CB). In semiconductors, these bands are separated by a bandgap without allowed electron states, with a width of $E_g < 5\,\mathrm{eV}$ [41 (p. 366)]. Hence, electrons in the valence band can be externally excited to the conduction band, e.g. by means of the absorption of a photon with energy $E \geq E_g$, leaving an unfilled position in the valence band also called a hole. The recombination of this electron-hole pair can be radiative, emitting a photon with a wavelength corresponding to the energy released $E \leq E_g$. The deepest level of the conduction band and the maximal-energy state

[1] Indeed, even in this simplified picture, the photons follow a narrow spectral linewidth due to the energy-time uncertainty principle.

of the valence band each corresponds to a certain momentum of the lattice (wave vector). If these wave vectors are the same, the band gap is called a direct gap; otherwise, it is referred as an indirect gap. In the case of the latter, the momentum of electrons and holes are not the same and a phonon-assisted transition is needed for the absorption and the emission of a photon. As this requires an extra particle, the probability of such a process is lower than in the case of direct transitions and thus the fundamental emission in indirect-gap semiconductors is relatively weak [42 (p. 23)].

In the case of radioactive decays inside the glass, the excitation of electrons is caused by high-energy charged particles. The energy released by these particles ($\mathcal{O}$(keV)-$\mathcal{O}$(MeV)) is much larger than the binding energies of atomic electrons ($\sim 10\,\mathrm{eV}$) and thus they lose their kinetic energy almost completely due to the excitation and ionisation of bound electrons in the material. During this process, the particles may also produce high-energy electrons (also called delta rays) that lose their energy exciting more electron-hole pairs. When the energy of the generated electrons is lower than the bound energy, they thermalise by intraband, radiative and nonradiative transitions. Let us first focus on the radiative processes inside semiconductors.

The emission spectra of a semiconductor can be divided between *intrinsic* (fundamental or edge emission) and *extrinsic*, also known as activated or characteristic emission [42 (p. 22)]. The intrinsic emission is caused, as its name suggests, due to the inherent properties of the material, viz. the aforementioned recombination of electrons and holes across the conduction and the valence band of the lattice, which is the inverse mechanism responsible for the fundamental optical absorption edge. On the other hand, the emission activated by impurities in the crystal is extrinsic in nature since they originate from energy levels in the band gap. This can be made much more intense than the intrinsic case, depending on the kind of activator and its concentration, which is the base of luminescent materials and phosphor technology. Figure 4.1 summarises a simplified picture of radiative transitions found in semiconductors. The first process (a) describes the intrinsic emission of $h\nu \cong E_g$ by the recombination of states close to the band edges. Nevertheless, normally, it results in a broad emission spectrum owing to the thermal distribution of charge carriers (see section 4.2). The next three processes (b) describe extrinsic emissions arising from decays that start and/or finish on energy levels of impurities (called donor, in the case of states near the CB and acceptors near the VB). As mentioned earlier, this can stem from impurity atoms, but also from lattice defects, such as dislocations, which can produce both shallow and deep energy levels. The last process (c) depicts the excitation and the radiative deexcitation through an impurity of incomplete inner shells, such as rare-earth ions (lanthanides). For these elements, the energy difference in the 5d and the 4f-shell is in favour of the 5d occupancy, thus leaving a vacant 4f-shell. The electrons of this shell are screened by the electrons in the outer orbitals and are therefore barely affected by the crystal lattice [40 (p. 221)]. This gives rise to well-defined energy transitions that can be easily recognised. Since lanthanides are commonly found in nature, they may

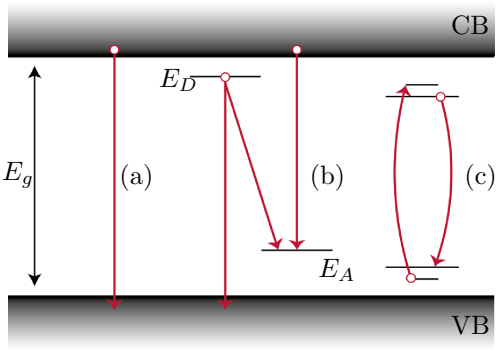

Fig. 4.1: Schematic diagram showing transitions between the conduction band (CB), the valence band (VB) and donor (E_D) and acceptor (E_A) levels. Based on [42 (p. 25)]

be a relevant trace luminescence centre for studies in this thesis.

As already denoted, the emission and the absorption of light in solids is a consequence of symmetric processes. This relation is illustrated in the next section, as it helps to explain luminescence properties exhibited in a material.

4.2 Absorption and emission of photons

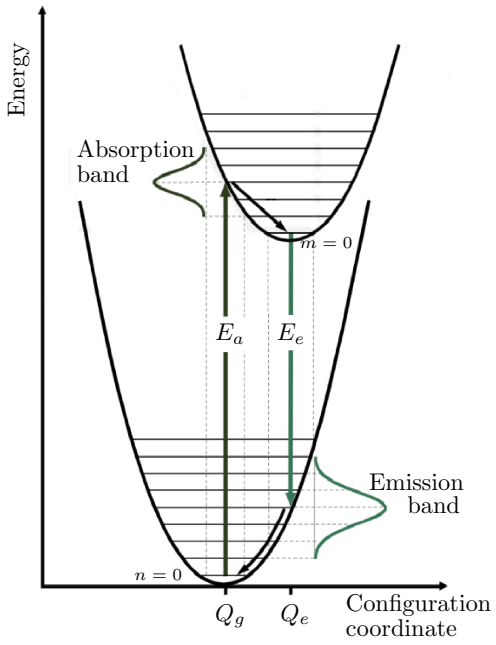

Fig. 4.2: Configurational coordinate diagram for a radiative recombination involving the emission of phonons. From [43] and modified.

The process of absorption and emission from luminescent point defects can be elementary described using a configuration coordinate diagram (see figure 4.2), which is a representation of the effects of the relaxation of the crystal following optical transitions [44 (p. 4)]. Here, Q_g and Q_e represent the distances of the nucleus in the ground (lower curve) and excited state (upper curve), respectively, and E_a and E_e are the energies at which the absorption and the emission are the most intense. At a temperature of 0 K the electron occupies the lowest vibrational level of the electronic ground state ($n = 0$) and any transition to the excited state will take place from this level. As the electron transitions are faster than the relaxation of the position of neighbouring atoms, the absorption occurs adiabatically represented by a vertical transition in the diagram (the Frank-Condon principle [44 (p. 4)]). The absorption transition carries the electron to an excited vibrational state and vertically projecting the endpoints of the $n = 0$ results in the width of E_a. After the absorption, the configuration relaxes through the emission of phonons to the zero vibration level of the excited state ($m = 0$) and the electron returns to the ground state, in this example via a vertical luminescence emission corresponding to the energy E_e. Analogously, projecting the endpoints of the $m = 0$ results in the width of the E_e emission band. The energy difference between E_a and E_e is called the Stokes shift. The greater the number of phonons involved in the transition, the larger will be this shift. Conversely, with a considerable overlap of the lowest vibrational states $n = 0$ and $m = 0$, the transition can occur without emission of any phonon and $E_e = E_a$. This is known as the zero-phonon-line. The transitions involving phonons form the phonon sideband, which lies at higher energies than the zero-phonon-line for absorption processes and at lower energies for radiative transitions.

As the temperature rises, higher vibrational states $n > 0$ are populated and more transitions occur from these levels to higher vibrational levels of the excited electronic state, resulting in broader absorption bands. The distribution of intensity between the zero-phonon-line and the sideband is also strongly temperature dependent. For example, at room temperature the probability for a $n = 0 \leftrightarrow m = 0$ transition is negligible [42 (pp. 30-32)] since the energy is high enough to emit a lot of phonons.

4.3 Nonradiative transitions

So far, only a de-excitation via radiative transitions has been assumed. However, the absorbed energy can be dissipated to the crystal lattice through different processes without the emission of photons, which are categorised as nonradiative transitions. Depending on the material, there are many kinds of such transitions and thus only the two most important processes, which occur in all inorganic semiconductors, are going to be explained in this section.

The principal nonradiative relaxation involves multiphonon emission, also known as thermal quenching. This effect is best appreciated by constructing a configuration coordinate diagram (see figure 4.3a). When the excited state and the ground state energy curves overlap at an energy thermally accessible, the electron can escape the excited state and return to the minimum energy generating phonons. The energy is therefore given up as heat to the lattice. The probability of thermal quenching P_{nr} is temperature-dependent as the electron in the excited state must overcome the barrier W, and is given by

$$P_{\mathrm{nr}} = C \cdot \exp\left(-\frac{W}{k_{\mathrm{B}}T}\right), \tag{4.3}$$

where k_{B} is Boltzmann's constant, T the temperature and C is a constant (units s^{-1}) [45].

Another source of nonradiative transitions are surface recombinations, since a continuum of states may join the conduction with the valence band, dissipating the excitation energy through the emission of phonons. These energy levels arise due to the abrupt change of the band structure of the bulk of the crystal, in addition to impurity atoms and oxide layers present on the surface. Furthermore, localised state bridges across the energy gap can be produced by crystal defects, such as pores, dislocations and grain boundaries [46 (p. 7)]. Although these recombination centres are very localized, the effect extends over the electron diffusion length. The configuration coordinate diagram of this effect is shown in figure 4.3b.

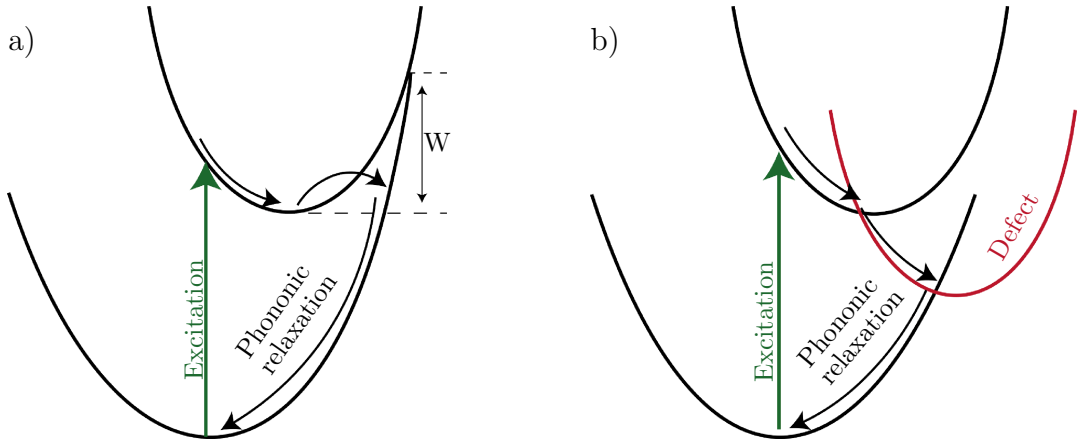

Fig. 4.3: Configuration coordinate diagram for two nonradiative transitions, **a)** thermal quenching [46 (p. 6)] and **b)** energy level crossing due to defects and bounderies effects [47].

4.4 Quantum yield and lifetime

As introduced in the beginning of section 4.1, the lifetime of a transition is $\tau = A^{-1}$, where A is the probability of decay per unit time. If for a transition competitive radiative and nonradiative processes are present, the observable lifetime τ is given by

$$\tau^{-1} = k_{\mathrm{r}} + k_{\mathrm{nr}} = \tau_{\mathrm{r}}^{-1} + \tau_{\mathrm{nr}}^{-1}, \tag{4.4}$$

where k_{r} and k_{nr} are the radiative and nonradiative rate constants respectively $A = k_{\mathrm{r}} + k_{\mathrm{nr}}$ and τ_{r}^{-1}, τ_{nr}^{-1} are the respective lifetimes [44 (p. 31)]. In general τ_{nr}^{-1} is the product of several nonradiative recombination processes and hence $\tau_{\mathrm{nr}}^{-1} = \sum_i \tau_{\mathrm{nr,i}}^{-1}$. Therefore the observable lifetime is dominated by the fastest time constant.

For example, in case of one transition of lifetime τ_0 and only considering thermal quenching, following equation 4.3, the total probability of decay per unit of time is given by

$$P(T) = \frac{1}{\tau_0} + C \cdot \exp\left(-\frac{W}{k_{\mathrm{B}}T}\right) \tag{4.5}$$

and thus the lifetime of the transition will follow the temperature dependence:

$$\tau = \frac{\tau_0}{1 + \tau_0 \cdot C \cdot \exp\left(-\frac{W}{k_{\mathrm{B}}T}\right)}. \tag{4.6}$$

Hence, the lifetime in this system decreases with higher temperatures. Furthermore, by measuring τ at different temperatures, it is possible to calculate the thermal quenching parameters C and W. However, there may be other non-negligible processes that show some temperature dependence, such as phonon-assisted indirect transitions, where the probability is $\propto \coth(\frac{E_{ph}}{k_{\mathrm{B}}T})$ for phonons with energy E_{ph} [45].

In a heterogeneous sample, where many luminescence centres are available, the time distribution of the fluorescence decay $I(t)$ can be described with a multiexponential model

$$I(t) = \sum_i \alpha_i \exp\left(-\frac{t}{\tau_i}\right), \tag{4.7}$$

where τ_i are the lifetimes of the transitions present in the sample and α_i, its relative intensity.

The internal quantum yield or radiative recombination efficiency η is defined as the ratio of luminescence photons emitted to the total recombination rate

$$\eta = \frac{k_{\mathrm{r}}}{k_{\mathrm{r}} + k_{\mathrm{nr}}} = \frac{\tau}{\tau_{\mathrm{r}}} = \frac{1}{1 + \tau_{\mathrm{r}}/\tau_{\mathrm{nr}}}. \tag{4.8}$$

Following equation 4.6, for a lattice where thermal quenching is the principal nonradiative transition, the recombination efficiency features a temperature dependence given by

$$\eta(T) = \frac{1}{1 + \tau_0 \cdot C \cdot \exp\left(-\frac{W}{k_{\mathrm{B}}T}\right)}, \tag{4.9}$$

and, therefore, an increase in temperature is expected to result in a lower value for the efficiency [44 (p. 32)]. However, as the determination of k_{r} and k_{nr} is not trivial, as every process involved has to be well known, usually the yield ε is given as a parameter for the

recombination efficiency, especially in the case of scintillator physics. The scintillation yield is the average number of emitted photons per unit of absorbed energy (MeV^{-1}) and thus the expected number of radiative transitions $\langle N \rangle$ after the absorption of the energy E is given by

$$\langle N \rangle = \varepsilon \cdot E. \tag{4.10}$$

The yield can be more easily determined experimentally than the recombination efficiency, and thus it enjoys common usage. However, the response to different energies is not always proportional and the yield varies between different particles. Both effects are the product of clusters of electronic excitations as a charged particle will produce many electron-hole pairs in a short distance. Luminescence centres can only provide one electron-hole and, if there are more electron-hole pairs in the ionisation volume than luminescent centres, the number of radiative transitions will decrease. Furthermore, the probability of Auger-like processes, where the energy of an electron is transferred to another one, increases with the charge carrier density, thus reducing the luminescence efficiency [48]. Henceforth, the higher the stopping power, the lower the yield shown by a sample and, for example, measurements of lithium glass scintillators show that the yield for 1 MeV protons, deuterons and alpha particles is lower than the one for 1 MeV electrons by a factor 2.1, 2.8 and 9.5, respectively [41 (p. 255)]. This is, nevertheless, highly material dependent.

5 Geant4 simulation for optical modules

Throughout this thesis, different simulations are necessary for correcting or interpreting results, as well for estimating the mDOM background inside the ice. These are done with Geant4, which is a software toolkit based on C++ developed at CERN and KEK for the simulation of particles passing through matter using Monte-Carlo methods. It is used by a vast number of experiments in different fields, such as high energy physics, medical science and astrophysics [49].

Various aspects are included in the simulation: the geometry of the setup and the materials properties involved in it, the particles of interest, the physics processes and models governing the interactions, the storage and visualisation of events for the post-processing of the data. An extensive set of physical models are already included in the Geant4 base code for a wide range of energy ranges, which have been widely validated with different experiments [50].

In this thesis, a modified version of the simulation initially written in the framework of two PhD thesis [31, 51] for the simulation of the mDOM response is used.

5.1 Geometry

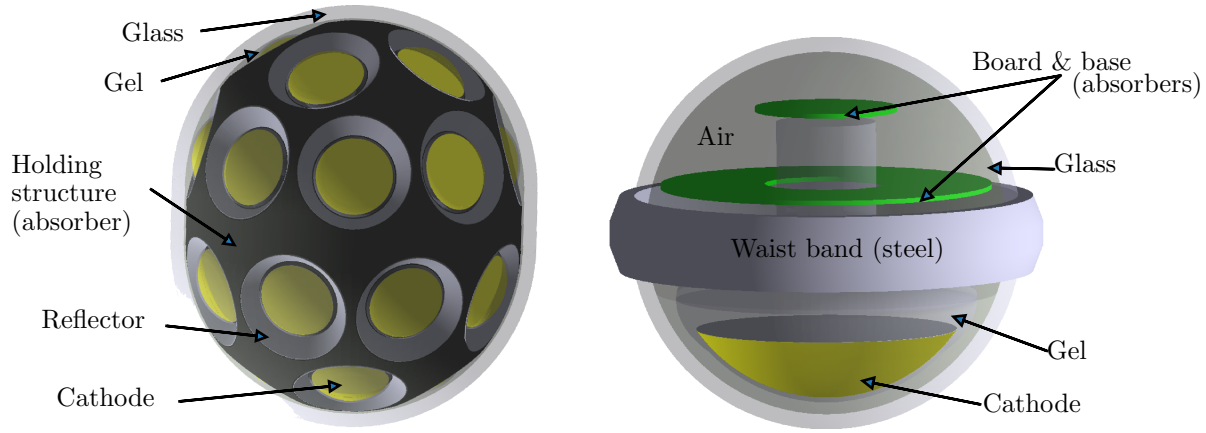

Fig. 5.1: Left: model of the mDOM as implemented in Geant4. Optical properties derived from measurements are applied to the main components. The holding structure is defined as an absorber, i.e. any photon that is in contact with it is deleted. **Right:** model of the DOM. The lower part of the module is filled with a gel volume and the rest with air. The board and base are defined as absorbers.

The simplest geometry definition in Geant4 is based on constructing with primitive building volumes (spheres, cylinders, ellipsoids, cubes, etc.), whose shape can be further adjusted by means of boolean operations. To each of these volumes is assigned a material, which also has a table of physical properties that define the possible interactions with particles (if a volume does not have any physical properties assigned, particles are not

affected by it). Within the scope of the module simulation, the most important properties are the refractive index and absorption length of the materials, as these determine completely the behaviour of photons. Within this context, the properties of glass and gel from different brands can be chosen, including the ones of interest for this work: Vitrovex glass, Benthos glass, QSI gel and Wacker gel.

Different geometries that replicate the measurement setups where simulated in the framework of this thesis. These are shown in their respective sections. For chapter 9, however, the detailed module geometries written by Lew Classen [31] are used, which are illustrated in figure 5.1. These feature the main components of the mDOM and DOM, with dimensions that fit information from technical drawings.

5.2 Physics and primary particles

A simulation starts with the generation of a primary particle including its initial properties (energy, location, direction, etc.). This particle then interacts with the simulated geometry and, if applicable, also produces secondary particles, depending on the implemented processes. The simulation of a single primary particle is called an **event**. Figure 5.2 shows two examples. The figure on the top illustrates the decay of a ^{40}K nucleus inside the pressure vessel of the DOM, producing Cherenkov and scintillation photons. The second example presents the cumulative output of three events, where the emission of alpha particles from a source was simulated for the study of air luminescence (see section 8.3.2). As different simulations were done in this thesis, the primary particle used are mentioned in their respective sections.

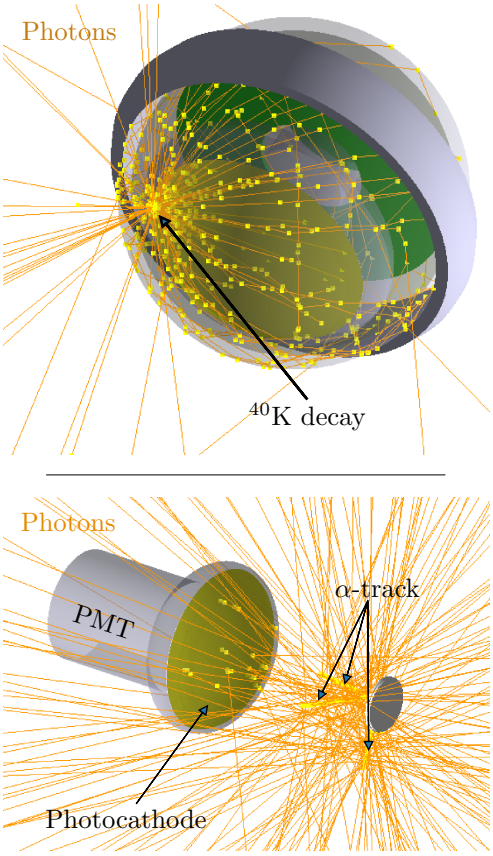

Fig. 5.2: **Top**: One event of a ^{40}K decay inside the DOM glass. The orange lines represent the trajectories of single photons. The positions of interactions are marked by yellow dots. **Bottom**: Cumulative output of three events of alpha particles exiting the air, which then scintillates.

As mentioned, Geant4 provides already a library of physics models. The user only has to specify the particles and processes that should be taken into account to compile a so-called **physics list**. Table 5.1 summarises the particles and interactions considered in the model used in this work.

For the simulation of the scintillation, the default class of Geant4, *G4Scintillation*, was modified in the scope of this thesis. The original code only allows the simulation of single or double exponential decays and was thus extended to triple exponential decays. Also, in the default class it is only possible to set either an universal scintillation yield for all particles, where the amount of emitted photons increases linearly with the particle energy (as in equation 4.10), or the user can provide tables for each particle with the number of emitted photons at different energies of the particle. The latter is intended for materials with

non-linear behaviour, which are, however, not considered in this thesis. Hence, a third option was added, enabling the definition of different scintillation yields depending on the particle, instead of using the same for each.

Finally, for the simulation of radioactive decays, the property table of the isotopes was modified, so that every nucleus decays with a lifetime of 0 s. This is done for being able to save the time of the interactions, without losing information in the nanosecond scale due to the limited value range of the float bit width.

Table 5.1: Particles and physics processes included in the simulation with their corresponding classes. The mDOMScintillation class is a modified version of G4Scintillation (see text).

Particle	Process	Geant4 Class
Optical photon	Absorption	G4OpAbsorption
	Optical processes at medium interfaces	G4OpBoundaryProcess
	Mie scattering	G4OpMieHG
Gamma	Pair production	G4LivermoreGammaConversionModel
	Compton effect	G4LivermoreComptonModel
	Photoelectric effect	G4LivermorePhotoElectricModel
Electron	Scattering	G4eMultipleScattering
	Ionisation	G4LivermoreIonisationModel
	Brehmsstrahlung	G4eBremsstrahlung
	Cherenkov radiation	G4Cerenkov
	• For positron: annihilation	G4eplusAnnihilation
Ions	Scattering	G4hMultipleScattering
	Ionisation	G4ionIonisation
	Radioactive decay	G4RadioactiveDecay
Alpha	Scattering	G4hMultipleScattering
	Ionisation	G4ionIonisation
All particles above excepting photons	Material scintillation	mDOMScintillation

5.3 Photon handling

For the simulations done in this thesis, there will always be a "detector" volume, which will save the information of certain particles that interact with it. In the case of the simulation of PMTs, this is the photocathode. After an optical photon hits this volume, its information (wavelength, hit location and time, mother particle, etc.) is saved in different vectors and then "killed", i.e. the simulation of the photon is stopped. The saved information can be then processed and saved.

In the scope of this thesis, a PMT response class was written for a more efficient data post-processing. This considers the quantum efficiency of the PMT[1] and also its time

[1] Based on the code written by Cristian Lozano in the framework of the thesis [32].

response. The QE is simulated at the moment the photon hits the photocathode. Here, a random number between 0 and 1 is generated; if this number is smaller than the QE for the wavelength of the photon, the hit is considered for further processing.

To take into account the TTS and time response, a random value sampled from a Gaussian distribution with mean 0 s and standard deviation equal to the TTS of the PMT is added to the arrival time of the detected photons. Then the hits are ordered regarding their hit time and it is tested if the PMT could have measured every photon separately. For this, two aspects are considered. In some experimental setups, there is a dead time after the detection of a PMT pulse. In this case, all simulated hits inside the dead time are deleted. If there is no dead time and only a bare PMT is simulated, when two or more photons are detected inside a small time windows an SPE pulse for every photon is generated, forming a waveform. The SPE pulse must be provided by the user. An example is shown in figure 5.3. With this waveform, it is possible to check if the hits were temporally resolved above the trigger level of the measuring device. If for a hit this is not the case, i.e. it was inside the pulse of the previous photon and the threshold was not surpassed a second time, this hit is deleted. Every hit also has an "amplitude" array, which considers the number of photons detected in it. For example, if a hit is followed by three other photons that were not temporally resolved, this hit will have an amplitude of four. This is important for post-simulation processing of the data, as SPE pulses may not be detected, because of the trigger level of the device, and the number of hits has to be corrected[2].

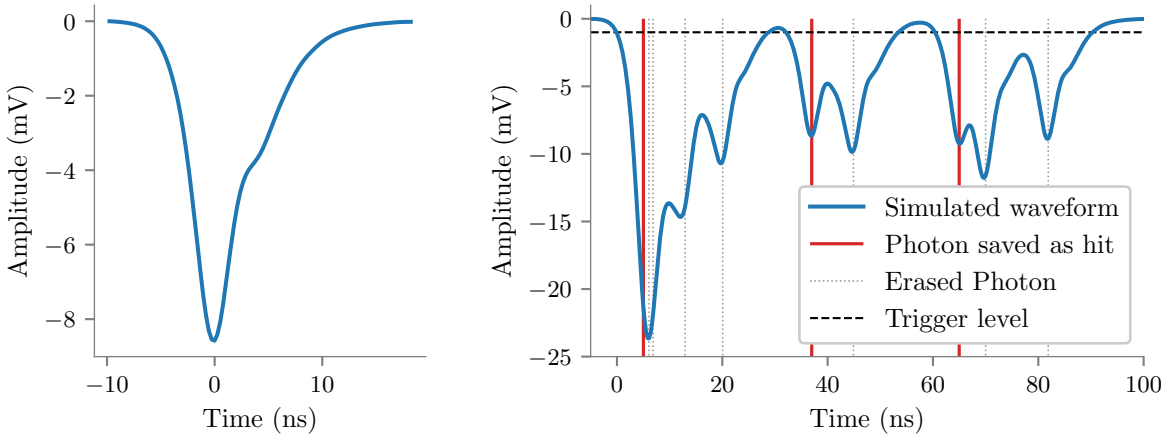

Fig. 5.3: Right: Average SPE measured with a PMT Hamamatsu R12119-02. **Left:** Example for a simulated waveform in Geant4 for the counting of hits.

[2]This is not simulated right away, as the percentage of SPE loss in a measurement can change rather quickly depending on different parameters (see 7.1.2). Therefore, the most efficient option is to save every photon that was temporally resolved, and then do a post-processing for the consideration of these factors.

Part II

Studies on dark rate from radioactive decays

6 Determination of material radioactivity

Essential for this work is to know how much radioactivity is expected to be found in the optical modules. One method for measuring isotope activities is gamma spectroscopy. This can be done with a scintillator or a semiconductor detector. For measurements where the isotopes in the sample are not known usually the latter is used, as it yields a much higher energy resolution and therefore the gamma energies can be better distinguished and classified. Hence, this chapter will focus only on spectroscopy using semiconductor detectors.

In 2016, measurements were done at the University of Alberta, Canada, at a low-level counting setup for, among others, a Vitrovex and a Benthos glass sample. The results of these measurements needed geometry correction factors that were calculated in this work. Also, for the sake of better statistics, more measurements were carried out in the scope of this thesis.

At the beginning of this chapter, a small introduction to Gamma spectroscopy is given (6.1). The second part (6.2) is devoted to the analysis of the measurements of Alberta and at the final part, the measurements done in the scope of this work are explained and evaluated (6.3). An extensive description of gamma spectroscopy and semiconductor detectors can be found in [52] and [41], and a more specific description for low-level counting in [53].

6.1 Introduction to gamma spectroscopy

With gamma spectroscopy it is possible to calculate the unknown concentration of radionuclides by evaluating the energies and intensities of gammas emitted by decays in a sample. These gammas interact with the detector medium, releasing ionising electrons by the photoelectric effect, Compton scattering or pair production. In the case of a semiconductor detector, which is based on a p-n junction, the ionising electrons produce a number of electron-hole pairs proportional to the absorbed energy. These charge carriers are then collected and amplified, for then being read out as a voltage pulse. The amplitude of this signal is digitised by a multichannel analyser.

A typical pulse-height spectrum is shown in figure 6.1. On the right side of this spectrum is

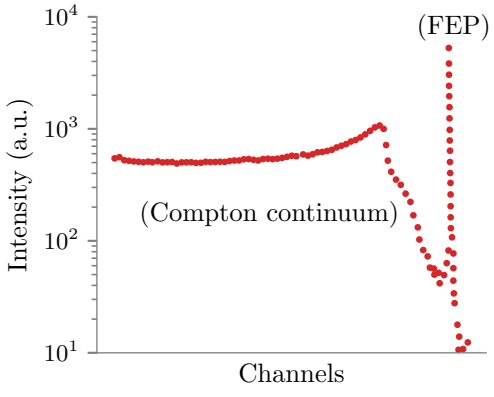

Fig. 6.1: Pulse-height spectrum of a monoenergetic gamma-ray source. Data taken from [53].

the full energy peak (FEP) produced when the gamma energy is totally absorbed. At lower energies of the FEP is located the Compton continuum, measured when the gamma scatters in the detector but then escapes without being fully absorbed. The calibration from channel to energy can be done by measuring a known radioactive source and relating the centre position of its FEPs to the gammas energy. In this manner, one can later estimate the gamma-ray energy of a sample by determining the position of the FEPs in the spectrum, which ultimately leads to the identification of the decaying isotope. The concentrations of the radionuclide can be then calculated by evaluating the area under its FEPs.

For a total number number of counts (net peak area) S_0 from a FEP corresponding to the energy E_0, the activity of the emitter isotope A_0 can be calculated using

$$A_0 = \frac{S_0}{t_\mathrm{m} \cdot \varepsilon(E_0) \cdot I_0}, \tag{6.1}$$

where t_m is the duration of the measurement, $\varepsilon(E_0)$ the absolute detection efficiency for gammas with energy E_0 and I_0 the gamma-ray intensity (probability of emission of the particular gamma-ray after a decay). The efficiency $\varepsilon(E)$ depends on the geometry of the setup, and on the energy of the gamma quantum, as the interaction probability for the photoelectric effect is energy dependent. It can be calculated using Monte Carlo simulations, taking into account the geometries and materials of the detector and the source, and on the distance between them.

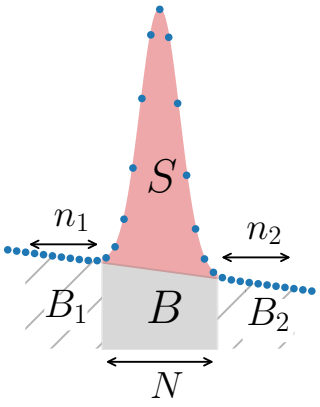

Fig. 6.2: Sketch of the parameters for the calculation of net peak area.

Since in a normal gamma spectrum there are many FEPs with different energies, the peaks are superimposed on a background formed by the Compton continuum stemming from more energetic gamma-rays. Therefore, for the estimation of the net area peak, it has to be corrected for the Compton background contribution. There are different approaches for this evaluation [54], but as long as the spectrum does not exhibit poor counting statistics, there is no much difference between their results. In this thesis, it will be assumed a linear continuum under the FEP, which is described in [54]. Here, the average background count per channel is calculated immediately before and after the peak. This value is then subtracted from the peak. If the FEP is found across N bins, and the background continuum before and after the FEP is spread over n_1 and n_2 channels, which have a total of B_1 and B_2 events, then the total counts in the FEP originating from the background B is

$$B = \frac{N}{2}\left(\frac{B_1}{n_1} + \frac{B_2}{n_2}\right) \tag{6.2}$$

and hence the net area will be $S = T - B$, where T is the total number of counts under the FEP. Figure 6.2 shows a sketch of this calculation.

Not all the measured FEPs will originate from radionuclides in the sample. There is also a contribution from decays occurring in the detector and materials in its vicinity, and radiation from cosmic rays. Therefore, it is important to reduce these external sources by

shielding the detector with materials with a high atomic number, like lead. Anyway, it is necessary to make a background measurement (that is, without any sample in the detector complex), since it is not possible to completely eliminate the external background. The gamma spectra have to be then corrected with this background measurement.

The levels of background radiation of the detector determines the sensitivity of the system. If a background measurement of time t_0 has B counts at a specific FEP, then the uncertainty of this measurement will be $\sigma_\mathrm{B} = \sqrt{B}$, as it follows Poisson statistics. For a signal from a sample to be statistically valid, it has to produce at least $\sqrt{B}$ counts, which means there is a lower boundary $L(t_0, E_0)$ for the measurable activities, which depends on the detection system and the measured time. Following equation (6.1) this can be determined to be

$$L(t_0, E_0) = \frac{\sigma_\mathrm{B}(E_0)}{t_0 \cdot \varepsilon(E_0) \cdot I_0} = \frac{\sqrt{B(E_0)}}{t_0 \cdot \varepsilon(E_0) \cdot I_0} \tag{6.3}$$

for a FEP corresponding to an energy E_0.

The background measurements of the setup of Alberta and Münster, are presented in figure 6.3. It is noticeable that for most energies, the background of the system in Alberta is almost one order of magnitude lower. This makes it more suitable for finding gamma-rays of inferior intensities and isotopes with small activities. Therefore, the isotope identification will be done from the measurements made in Canada, which are presented in the next section. Nevertheless, it will be shown that the setup of Münster is sensitive enough for measuring most of the isotopes in the sample, allowing to calculate activities with similar relative uncertainties.

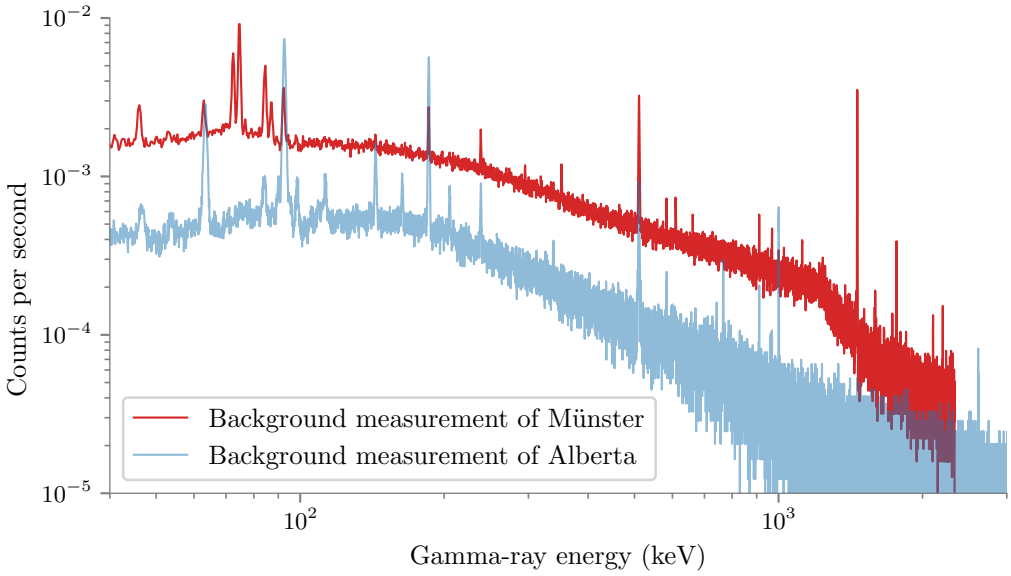

Fig. 6.3: Background measurement of the detection system in the University of Alberta and the University of Münster.

6.2 Identification of isotopes present in the samples

The Vitrovex glass sample measured in Alberta has a cylindrical shape and weights (575 ± 5) g, which was provided by the company. The sample of Benthos glass is a fragment from a half vessel of an IceCube DOM, and weights (341 ± 5) g. The measurement

of the first sample lasted 1.8 days and of the latter 3.1 days[1]. The results from the Vitrovex sample are shown in figure 6.4. For the identification of most of the peaks, the software Prospect Genie 2000 was used, which provides a gamma-ray energy library. All gamma-rays can be identified to be originating from only 12 different isotopes. These nuclides, except for ^{40}K, are part of one of the three natural decay chains: ^{235}U , ^{238}U and ^{232}Th. The radionuclides from these series with their most intensive gamma-emissions are summarised in table 6.1.

Table 6.1: Most intense gamma-ray energy of each isotope from the ^{238}U ,^{235}U and ^{232}Th chain. In bold and italic are the isotopes that were measured in both, the spectrum of the Benthos and Vitrovex sample.
n.e. Isotope does not emit gamma-rays.
†: Regarding its intensity, the isotope should have been measured, if the chain is in secular equilibrium.

^{238}U Chain			^{235}U Chain			^{232}Th Chain		
	Energy (keV)	Intensity (%)		Energy (keV)	Intensity (%)		Energy (keV)	Intensity (%)
^{238}U	n.e.		***^{235}U***	185.7	57	^{232}Th	63.81	0.263
^{234}Th	63.29	3.7	^{231}Th	89.95	6.6 †	^{228}Ra	n.e	
^{234}Pa	1001.03	0.84	^{231}Pa	300.06	2.41	***^{228}Ac***	911.2	25.8
^{234}U	53.2	0.12	^{227}Ac	99.6	0.006	***^{228}Th***	84.37	1.19
^{230}Th	67.7	0.38	^{227}Th	235.96	12.9 †	^{224}Ra	240.99	4.1 †
^{226}Ra	186.2	3.64	^{223}Ra	269.5	13.9 †	^{220}Rn	549.73	0.11
^{222}Rn	510	0.08	^{219}Rn	271.2	10.8 †	^{216}Po	804.9	0.002
^{218}Po	n.e.		^{215}Po	n.e		***^{212}Pb***	238.63	43.6
^{214}Pb	351.93	35.6	^{211}Pb	404.85	3.78	***^{212}Bi***	727.33	6.67
^{214}Bi	609.32	45.5	^{211}Bi	n.e.		^{212}Po	n.e.	
^{214}Po	799.7	0.01	^{207}Tl	897.77	0.263	***^{208}Tl***	583.19	85
^{210}Pb	46.54	4.25	^{207}Pb	n.e.		^{208}Pb	n.e.	
^{210}Bi	n.e.							
^{210}Po	803.06	0.001						
^{206}Pb	n.e.							

For the estimation of the absolute detection efficiency, a Geant4 simulation provided by Pawel Mekarski from the University of Alberta was used. The detector geometry is already defined in this code, while the geometry of the samples was incorporated into the program in the scope of this work. The efficiency is calculated by simulating N_T gamma-rays stemming isotropically from the sample and saving the energy deposited in the active volume of the germanium crystal. The result of this is a histogram similar to the response function seen in figure 6.1. Then, integrating the FEP of this histogram, one gets the number of gamma-rays N_D that were totally absorbed in the detector, which ultimately leads to the efficiency $\varepsilon = \frac{N_D}{N_T}$.

Once the efficiency is simulated and calculated for every gamma-ray energy of the identified isotopes, it is possible to determine the decay rate of the radionuclides. For

[1]Respectively 159 741 s and 264 998 s.

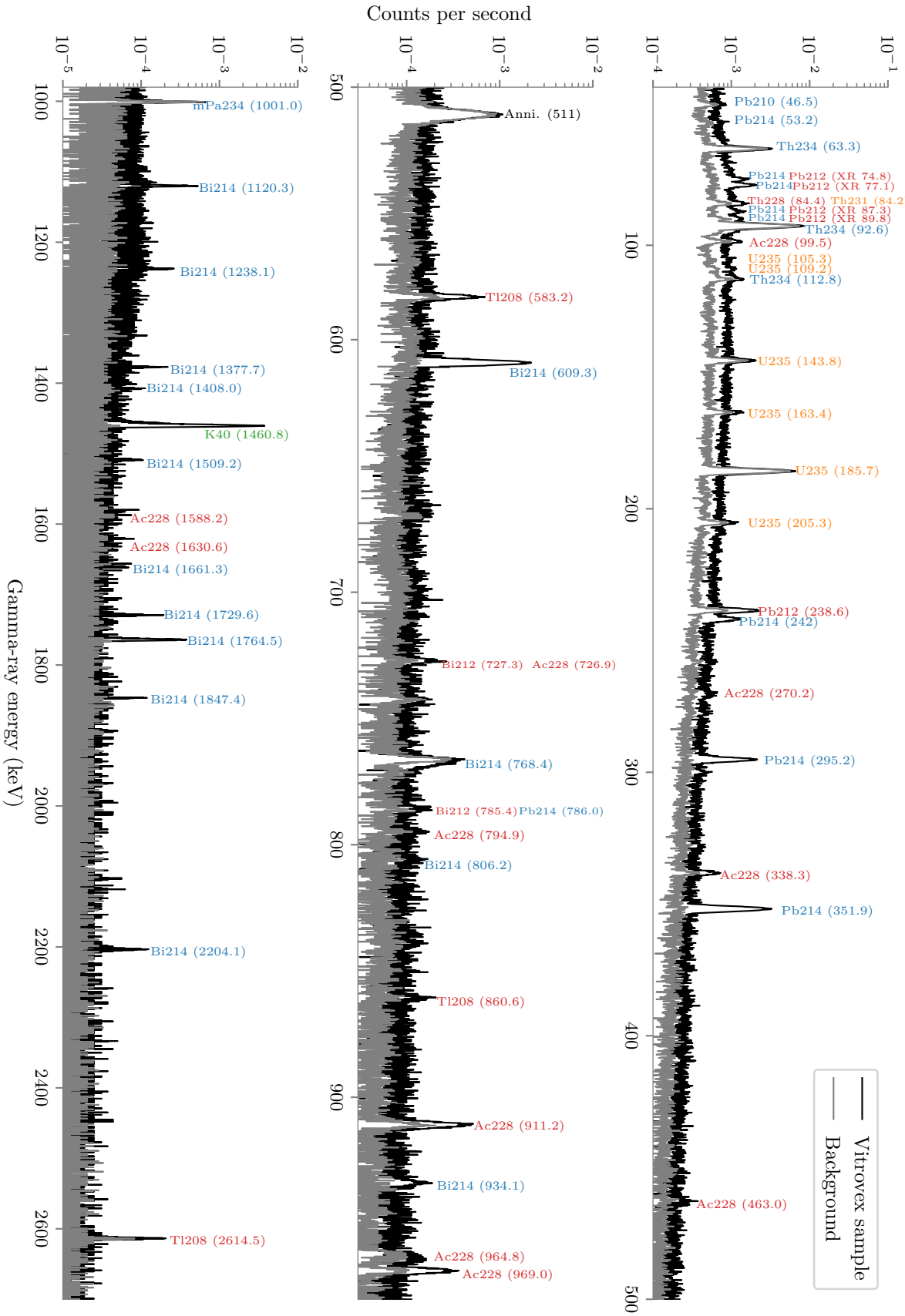

Fig. 6.4: Gamma spectrum of the measurement of the Vitrovex glass sample and the background done at the University of Alberta.

this, only the most intense gamma-rays were used, which did not overlap with other lines. In table 6.2 the resulting mass-specific activity $\frac{A}{m}$ are provided for each isotope. Here the total activity of the sample calculated with equation (6.1) is divided by its mass m for better comparison between specimens of the same material.

Table 6.2: Mass-specific activities from the samples measured at the University of Alberta. For the case of the ^{238}U- and ^{232}Th series, the average activity of their isotopes are also given.

	Mass-specific activity (Bq/kg)	
	Vitrovex	Benthos
^{214}Bi	4.24 ± 0.14	3.41 ± 0.16
^{214}Pb	5.19 ± 0.15	3.85 ± 0.12
^{234}Th	4.49 ± 3.3	1.81 ± 2.6
^{238}U-Chain	4.69 ± 0.10	3.67 ± 0.10
^{228}Ac	1.42 ± 0.24	0.84 ± 0.21
^{212}Pb	1.04 ± 0.20	0.72 ± 0.12
^{208}Tl	0.97 ± 0.14	0.78 ± 0.17
^{232}Th-Chain	1.07 ± 0.10	0.76 ± 0.09
^{235}U-Chain	0.62 ± 0.16	0.30 ± 0.12
^{40}K	66.2 ± 1.2	5.3 ± 0.6

In nature, the three decay chains are approximately in secular equilibrium, as long as the soil has been undisturbed for a long time [55]. This means, it is to be expected that all isotopes listed in table 6.1 should have the same decay rate within its decay series. Consequently, once the activity of an isotope from a chain is known, one can calculate the expected number of detected gamma-rays originated from a specific isotope, by solving for S_0 in the equation (6.1). This was done for all undetected isotopes from the series. Four FEP from the ^{235}U- and one from ^{232}Th-chain, should have been detected in the measurement if the assumption of secular equilibrium were to be correct. Nevertheless, all their gamma-rays that were intense enough to be detected, had a similar energy of another FEP with higher activity. For example, the line from ^{223}Ra and ^{219}Rn with an energy of 269.5 keV and 271.2 keV, from the ^{235}U-chain, lie in between a line from ^{228}Ac with an energy of 270.2 keV from the ^{232}Th-series, which has a higher activity. Hence, both isotopes could have been detected, but cannot be distinguished from other lines within the detector resolution. This is also the case for the 269.5 keV-gamma-ray ^{224}Ra and the 89.95 keV from ^{231}Th (see figure 6.4).

It is noteworthy that the activities of isotopes of a single series do not agree within their error, but are similar. Hence, the assumption of secular equilibrium is only an approximation. Nevertheless, it will be assumed that all isotopes of the series have the same activity, using the average of measured activities, which also can be found in table 6.2. In the case of the ^{235}U-series, only one isotope in the chain was measured, namely ^{235}U, and therefore its activity is assumed for the rest of radionuclides of the series.

It is to notice that the Benthos sample has a far lower concentration of radioisotopes than the Vitrovex one, especially of ^{40}K, which is more than twelve times higher in the

latter. This would imply that choosing the Benthos glass would yield lower dark rates from luminescence, assuming that both glasses have the same scintillation properties. This raises the question, whether the "cleanliness" of the glass samples is an intrinsic property of the brand, or if there is a high variance between specimens of the same material. To check up on this, new measurements were done in the scope of this work. Also, specimens of the two optical gel brands, Wacker and QSI, were produced and examined. The next section presents the results of these measurements.

6.3 Activity variance between samples

The Vitrovex sample tested in Canada was one of a set of three that were delivered from the company. These samples were available for measurements, together with two half pressure vessels of the same shape, one made from Benthos and one from Vitrovex glass. The latter is an old specimen of the early 2000s. As these samples have distinct geometries, the detector will have very different absolute detection efficiencies between these samples. While the smaller cylindrical samples can be placed near the germanium detector, the half vessel will use a larger volume, reducing the solid angle from where the gammas will be detected. The efficiency was therefore simulated preparatory to the measurement so that its duration could be estimated in such a way, that the measured spectra had similar statistical uncertainties. For this, a Geant4 code with the geometry of the detection system provided by Volker Hannen was integrated into the software used in the last section. The results can be found in figure 6.5.

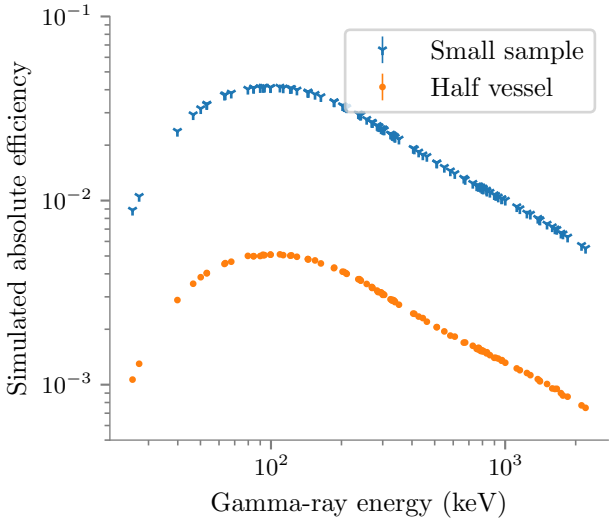

Fig. 6.5: Absolute detection efficiency of the expected gamma-rays for both geometries, the cylindrical small samples (Vitrovex) and the half vessels (Vitrovex and Benthos).

The detection efficiency for the cylindrical samples is, as expected, almost one order of magnitude larger than the one for the half vessels. However, the mass of these samples differs also by one order of magnitude, thus a similar measuring duration should deliver comparable statistical uncertainties. The evaluation of the peaks was the same as in the last section. The calculated activities are presented in table 6.3[2].

First of all, it can be noticed that the measurements for both small Vitrovex samples yielded a similar result to the one in table 6.2. The biggest divergence between these samples were the results for the isotopes from the ^{232}Th-Chain and ^{40}K with around 20-30% difference. The Vitrovex vessel shows greater deviations, which exhibits almost twice the amount of radionuclides from the ^{238}U- and ^{232}Th-series and none measurable ^{40}K.

[2]The gamma spectra from these measurements are shown in appendix A.

This is also the case for the Benthos vessel, which presents a higher amount of the natural series, but a far lower ^{40}K activity, than the sample in table 6.2.

Table 6.3: Mass-specific activities from the samples measured in this work. For the case of the ^{238}U- and ^{232}Th series, the average activity of their isotopes is also given. The last two rows present the measurement duration and the weight of the samples respectively. VV stands for Vitrovex and BT for Benthos.

	Mass-specific activity (Bq/kg)				
	VV 1	VV 2	VV vessel	BT vessel	Wacker & QSI gel
^{214}Bi	4.01 ± 0.16	4.29 ± 0.17	8.14 ± 0.20	5.14 ± 0.17	<0.15
^{214}Pb	4.82 ± 0.12	4.83 ± 0.14	8.83 ± 0.18	5.29 ± 0.16	<0.11
^{234}Th	5.2 ± 0.9	4.8 ± 1.2	5.1 ± 0.8	4.7 ± 0.7	<0.76
^{238}U-Chain	4.53 ± 0.10	4.61 ± 0.19	8.42 ± 0.13	5.20 ± 0.12	<0.11
^{228}Ac	1.31 ± 0.21	1.34 ± 0.22	2.37 ± 0.24	1.71 ± 0.22	<0.26
^{212}Pb	1.42 ± 0.10	1.34 ± 0.11	2.03 ± 0.12	1.04 ± 0.11	<0.10
^{208}Tl	1.38 ± 0.20	1.32 ± 0.21	2.06 ± 0.28	1.16 ± 0.25	<0.15
^{232}Th-Chain	1.39 ± 0.09	1.34 ± 0.09	2.27 ± 0.10	1.16 ± 0.09	<0.10
^{235}U-Chain	0.56 ± 0.07	0.61 ± 0.07	0.75 ± 0.08	0.61 ± 0.09	<0.05
^{40}K	53.6 ± 1.7	57.5 ± 1.8	<0.99	1.0 ± 1.4	<1.32
Measurement duration (s)	256419	262815	265731	269667	251533 315285
Sample mass	(641 ± 5) g	(604 ± 5) g	(4.37 ± 0.01) kg	(4.43 ± 0.01) kg	(649 ± 5) g (651 ± 5) g

The fact that the three small samples from Vitrovex have similar activities, but deviate a lot from the vessel, may imply that the amount of radioactivity is dependent on the production batch, as probably the same source for the raw material is used for each one. Also, K_2O is often added in different production steps of the glass, but is not an imperative, since it can be replaced with Na_2O [6]. This could explain that some samples have high activities of ^{40}K and other no measurable amounts. For a better understanding of this deviation, the production steps from samples should be known by direct communication with the manufacturers. This is especially the case for the Vitrovex vessels, as the three small samples, which were produced in late 2015, have higher ^{40}K activities than the older Vitrovex vessel. If this difference is caused merely by a production step, it could be avoidable. Also, the new Vitrovex vessels designed for the mDOM should be examined with gamma spectroscopy. This could not be done in the scope of this work, as the detection system was too small for them. But it would be appropriate, as the production of the smaller Vitrovex samples may be different to the one of the vessel.

The gamma-spectra from the gel samples did not yield any measurable activity. This does not exclude them from the studies of this thesis, as they could still have luminescence properties. Thus, a decay originating from the vessel could deposit some energy in the gel layer, which could then emit scintillation photons.

7 Characterisation of PMTs

To accurately simulate and calculate the scintillation properties, it is necessary to fully know the response of the detectors. This chapter presents the quantum efficiency, gain and TTS of the PMT used in this work (Hamamatsu R12199-02, SN ZB6180).

7.1 Gain and TTS

7.1.1 Setup

The setup for the gain and TTS measurement is illustrated in figure 7.1. The photomultiplier is positioned in a light-tight box and illuminated with a pulsed LED[1], which is triggered by a pulse generator[2]. The latter also triggers the oscilloscope[3], allowing for effective background suppression. The light of the diode is fed into the dark box by means of an optical fibre terminated by a diffuser, achieving a homogeneous illumination of the photocathode. The dark box is placed in a climate chamber for temperature regulation. As there is a temperature gradient between the chamber and the inside of the dark box, a remotely controlled temperature and humidity sensor is attached to the base of the PMT. In order to set the same PMT voltage throughout all the measurements, the maximum for the first coarse of the high voltage supply is used, which is $(996 \pm 1)\,\mathrm{V}$.

The signal of the PMT is amplified[4], digitised by the oscilloscope and processed online in a computer with a Python code, saving the charge, amplitude and leading edge time of the main pulse. This was done for $3 \cdot 10^5$ pulses every 5 °C from 20 °C to −50 °C. With this

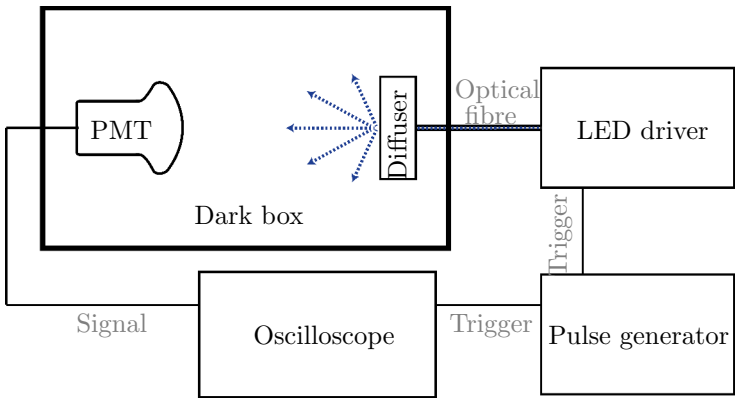

Fig. 7.1: Experimental setup for the determination of gain and TTS of a PMT. The dark box is placed inside a climate chamber for temperature regulation (not shown in the figure).

[1] PicoQuant PDL 800-B with LED PLS-8-2-719.
[2] RIGOL DG1032Z
[3] PicoScope 6404C
[4] Fast amplifier NE 468

data, the gain and TTS were determined as a function of the temperature. The results are shown in the following sections.

7.1.2 Gain

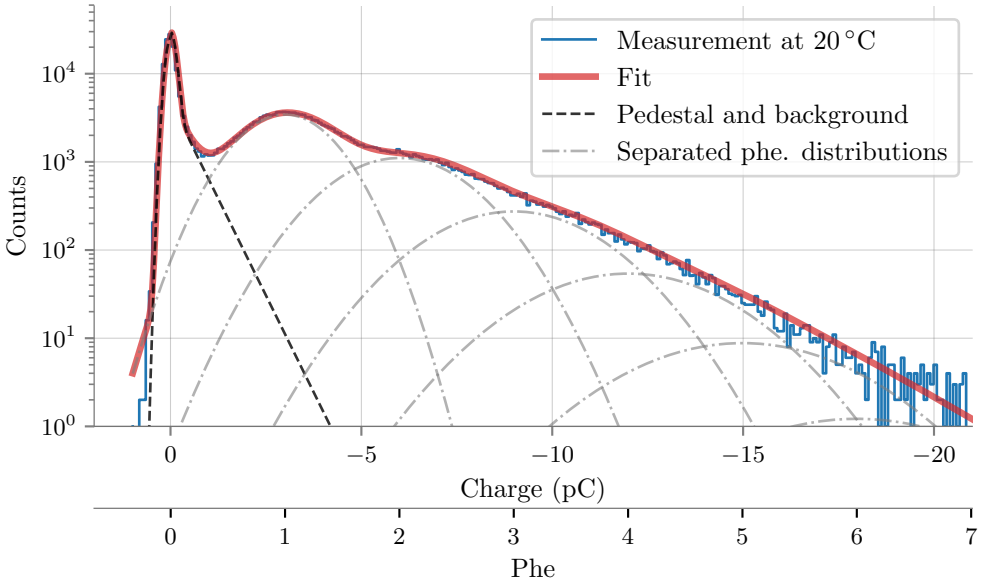

Fig. 7.2: Charge histogram for the measurement at a temperature of 20 °C. The data is fitted with the function introduced in eq. 3.5. The resulting Gaussians represent the deconvoluted phe. distributions, while the pedestal includes an exponential that represents noise and background processes.

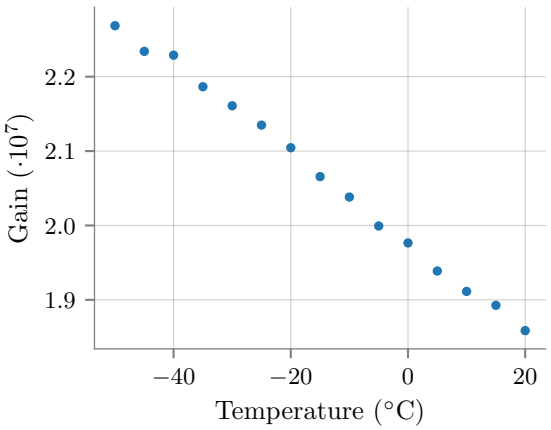

Fig. 7.3: Gain of PMT with an amplifier at different temperatures. Uncertainties from the fit are smaller than the data point markers.

For the determination of the gain, the measured charge is arranged into a histogram, which is then fitted with the distribution from equation 3.5. However, the discrete background distribution Q_{sh} is set to zero, as it breaks the linearity between charge and the number of photoelectrons in the interval 0 - 1 phe. This does not change the results by much, as a regression with the full distribution 3.5 also yields $Q_{\text{sh}} \approx 0$. An example fit is shown in figure 7.2. From this result, the mean charge of one photoelectron pulse Q_1 is obtained and the gain can be calculated by the equation 3.6. Figure 7.3 shows the obtained gain values at different temperatures.

In concordance with other measurements with this PMT model [31 (p. 103)], the gain grows with lower temperatures, reaching at −50 °C an increase of ∼ 22 % compared with respect to the measurement at 20 °C. The reason for this behaviour is not

known to date, although a rise on the secondary emission with lower temperatures has been observed with different electrode materials [56], which may imply an increase of the dynode's work function with the temperature.

The increase of the mean charge of one-phe pulses with decreasing temperatures has as a consequence that the number of undetected SPE events due to a constant amplitude trigger (as in the case of the PMT rate measurements) will also be temperature dependent. This effect is explained and quantified in the next section.

Photoelectron loss due to trigger

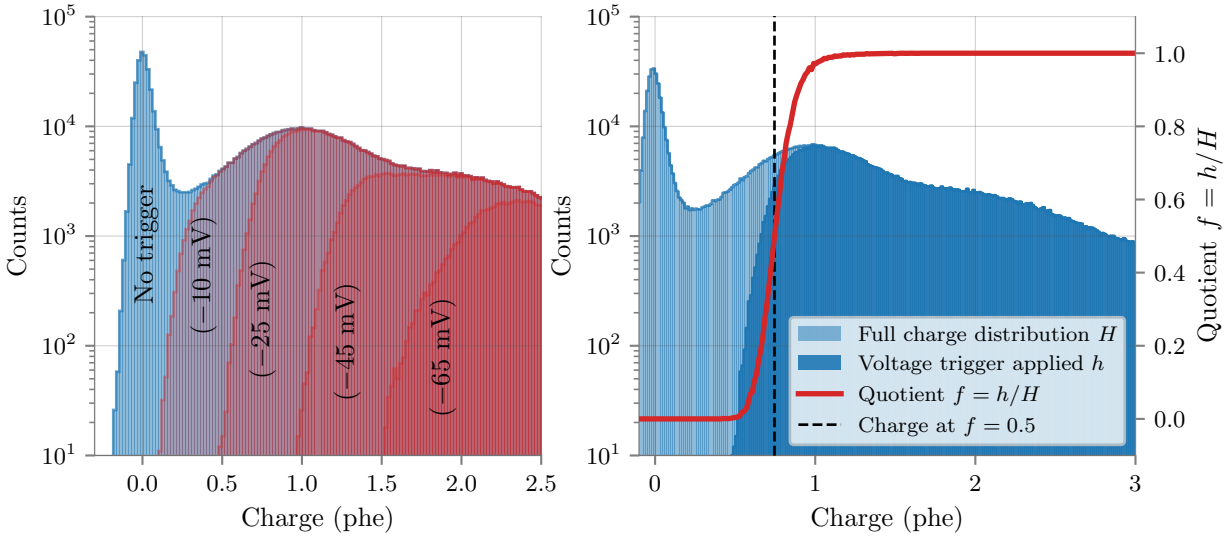

Fig. 7.4: Left: Effects of applying a voltage amplitude trigger to the measured pulses on the charge histogram. The charge is limited to higher phe numbers, but it does not exhibit a steep cut-off. **Right:** Example of the procedure for determining the threshold in terms of phe. The charge histogram of triggered pulses is divided by the full charge distribution bin-wise. The charge at which the quotient is 0.5 is defined as the charge threshold equivalent to a voltage trigger level. Data from the measurement done at −50 °C.

In order to separate the PMT signals from the noise, it is necessary to apply a trigger level. This means a voltage amplitude threshold has to be set if the PMT signal is being read out in pulse mode. Although both, the charge and amplitude of the pulses, increase linearly with the number of input photons, there is no direct translation from a pulse amplitude to its charge. This can be seen in the left plot of figure 7.4, where the charge distribution with different voltage thresholds is depicted. With lower amplitude thresholds, only pulses with larger charge are measured, but there is no steep cutoff. Consequently, it is necessary to set a condition that defines the charge threshold. Following the convention, this is the charge at which 50 % of the photoelectrons is lost[5].

As already explained, in the measurement the voltage and charge of the pulses are saved simultaneously. Therefore, from the same data set, the charge distribution of pulses that surpasses a specific voltage threshold can be made. The corresponding charge trigger to this amplitude threshold can be calculated by dividing the charge distribution with trigger applied h by the full charge distribution H and finding the point at which the

[5]Oleg Kalekin, personal communication, 18.08.2017

quotient is $f = 0.5$. As the division is done bin-wise, f can only take discrete numbers. Therefore, the 0.5 point is found by fitting the interval between 0.2 and 0.8 with a linear function. The plot on the right of figure 7.4 shows this procedure.

By calculating the trigger equivalent in phe for voltage thresholds between $-80\,\mathrm{mV}$ and $-2.4\,\mathrm{mV}$ the line illustrated in figure 7.5 is obtained. At high voltage threshold values (near zero), most of the data stems from the noise. In the charge distribution, these correspond to events in the pedestal, which have a charge close to near zero. Nevertheless, these pulses can have relatively large amplitudes, due to their fast fluctuation around the baseline. This produces a sharp line at the beginning of the curve of the left plot in figure 7.5. After leaving the zone of the pedestal, the line shows an expected affine behaviour, although this then turns into a linear one at around 1.2 phe.. The cause of this change is at the time of writing unclear. A possibility could be a long LED pulse duration, which would reduce the maximum voltage of the PMT pulse by increasing its length, but not the total charge. Another possibility is a restricting slew rate effect of the electronics, which also could lengthen the PMT signal[6]. The values in the range of interest for this work < 1 phe. should not be affected by these effects.

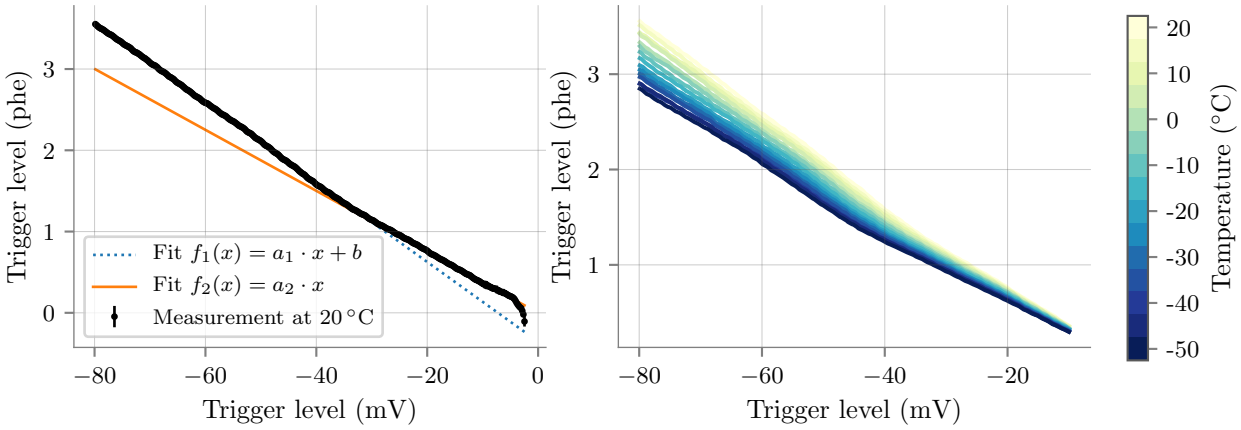

Fig. 7.5: Left: Charge trigger equivalent in phe. against the set amplitude trigger in mV. The curve features a kink at around ~ 1.2 phe., going from an affine function to a linear one. **Right:** Charge trigger equivalent in phe. against the set amplitude trigger in mV at different temperatures. The increase in gain with lower temperatures effectively reduces the trigger level.

The right plot of figure 7.5 shows the charge threshold at different temperatures. As a consequence of the increase in gain with lower temperatures, the charge equivalent to a constant voltage trigger sinks. The rate measurements presented in the next chapters will use a voltage threshold of $-18\,\mathrm{mV}$, since noise appeared at low temperatures. The evaluation of the relation at this amplitude in figure 7.5 yields the trigger values shown in figure 7.7.

With the deconvoluted charge distribution it is also possible to calculate the fraction of undetected photoelectrons due to the set trigger. For this, the one photoelectron Gaussian distribution is multiplied by the already calculated quotient f between the triggered charge distribution and the full charge histogram. The area of this distribution $A_{\mathrm{triggered}}$ will be therefore smaller than the one of the original single photoelectron Gaussian A_{full}, and the

[6]Oleg Kalekin, personal communication, 14.09.2017

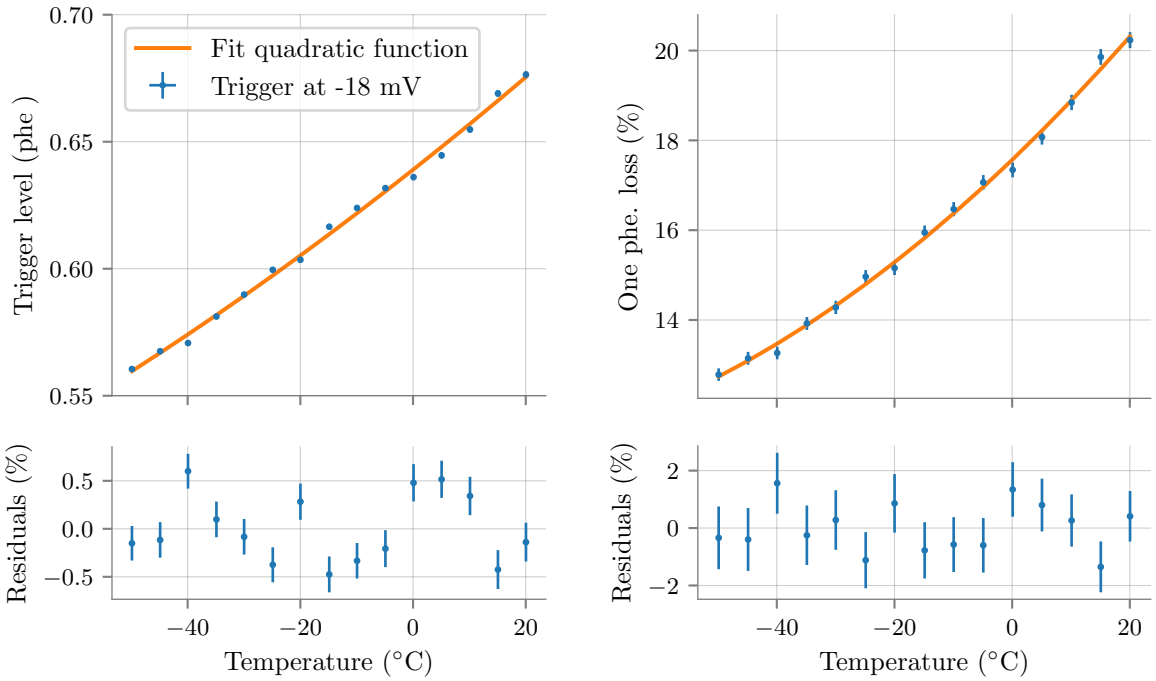

Fig. 7.7: The increase of the gain with lower temperatures effectively reduces the charge trigger level and therefore the number of undetected photons. **Left:** Trigger level in phe. against temperature in °C for a constant amplitude trigger at −18 mV. **Right:** Percentage of undetected one photoelectrons due to a constant trigger of −18 mV at different temperatures.

percentage of undetected photoelectrons can be calculated by

$$\frac{A_{\text{full}} - A_{\text{triggered}}}{A_{\text{full}}} \cdot 100\,\%. \qquad (7.1)$$

The SPE charge distributions at 20 °C and −50 °C for a trigger of −18 mV are presented in figure 7.6. As expected, the measurement at −50 °C loses fewer photoelectrons than the one at 20 °C owing to the gain difference. The percentage of one photoelectron loss is shown in the left picture of figure 7.7.

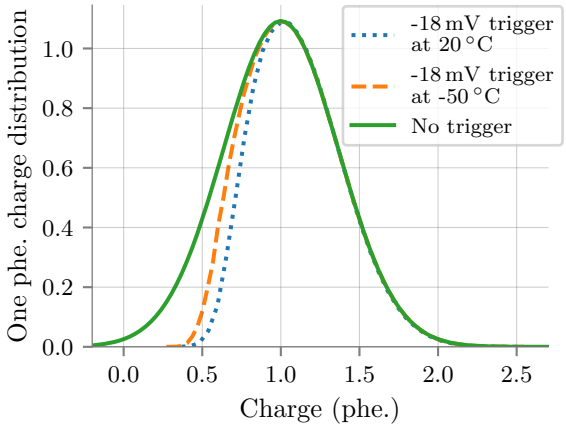

Fig. 7.6: Deconvoluted single photoelectron distribution with and without voltage trigger applied at 20 °C and −50 °C. With the integration of these Gaussian functions, it is possible to calculate the percentage of undetected photoelectrons due to the set trigger level.

The trigger charge equivalent and photoelectron loss results were fitted with a quadratic function $f(T) = \sum_{i=0}^{2} a_i T^i$ for its use in calculations of the next chapters. The fit coefficients of the charge trigger level in dependence of the temperature are $a_1^t = (0.639 \pm 0.001)\,\text{phe}$, $a_2^t = (1.760 \pm 0.006)\,10^{-3}\text{°C}^{-1}\text{phe}$ and $a_3^t = (3.3 \pm 1.7)\,10^{-6}\text{°C}^{-2}\text{phe}$, which yield relative errors below 0.5 % relative to the data points of the measurement. In the case of the photoelectron loss percentage the fit coefficients are $a_1^{pl} = (17.57 \pm 0.06)\,\%$, $a_2^{pl} =$

$(0.126 \pm 0.004)\,°C^{-1}\%$ and $a_3^{pl} = (5.8 \pm 1.1) \times 10^{-4} °C^{-2}\%$. Here the fit residuals are lower than 1.7 %.

7.1.3 Transit time spread

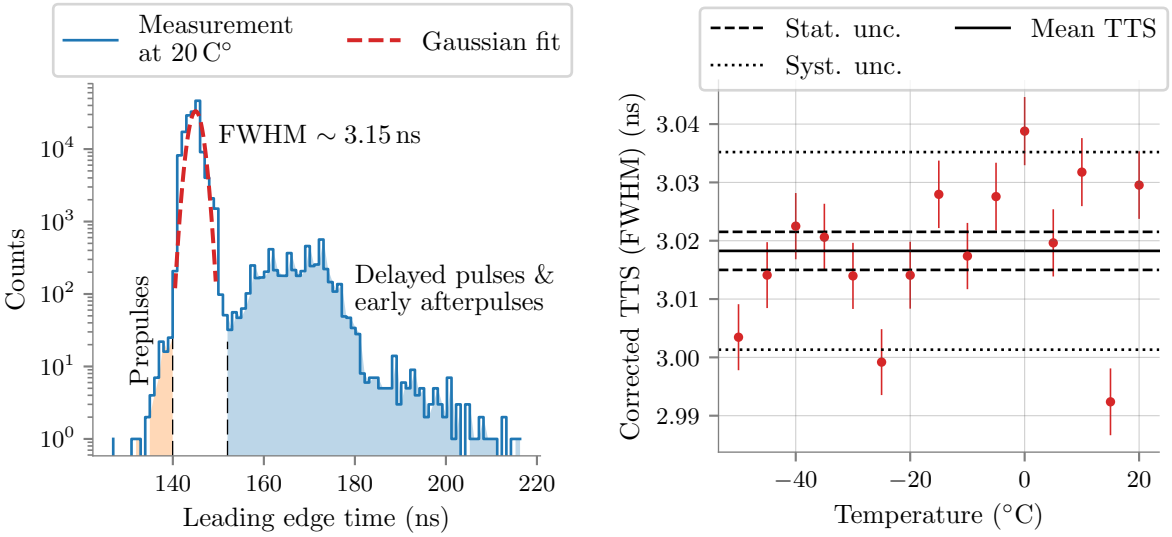

Fig. 7.8: Left: Leading edge time distribution of the measurement at 20 °C. In addition to the transit time spectrum, other effects like prepulsing and delayed pulses can be found (see section 3.2.4). **Right:** Calculated TTS of the PMT used at different temperatures. The mean and its statistical (stemming from the fit) and systematical error (including the uncertainties from σ_{LED}) are marked with a line.

With the raw data of the measurement described at the beginning of the chapter it is also possible to calculate the transit time spread. The time at which each PMT pulse surpassed the −15 mV (∼ 0.5 phe) voltage level was saved (leading edge time). The resulting time distribution features a characteristic main peak, as seen in the left figure 7.8. The TTS is defined as the FWHM[7] of this peak. Hence, one can fit a Gaussian function and the FWHM is calculated with $FWHM = 2 \cdot \sqrt{2 \cdot \ln 2} \cdot \sigma_{\mathrm{fit}}$, where σ_{fit} is the standard deviation of the fitted Gaussian. This, however, is a convolution of the time responses of all components of the measurement, which makes the measured distribution wider. The TTS can be calculated by subtracting these contributions:

$$TTS_{\mathrm{PMT}} = 2 \cdot \sqrt{2 \cdot \ln 2} \cdot \sigma_{\mathrm{PMT}} = 2 \cdot \sqrt{2 \cdot \ln 2} \cdot \sqrt{\sigma_{\mathrm{fit}} - \sigma_{\mathrm{LED}} - \sigma_{\mathrm{jit}} - \sigma_{\mathrm{sam}}}, \tag{7.2}$$

where $\sigma_{\mathrm{LED}} = (300 \pm 30)\,\mathrm{ps}$[8] comes from the non-zero duration of the light source, $\sigma_{\mathrm{jit}} = 30\,\mathrm{ps}$ the jitter of the external trigger, $\sigma_{\mathrm{sam}} = 230\,\mathrm{ps}$ caused by the sampling period of the oscilloscope $T = 800\,\mathrm{ps}$[9]. This was measured for a temperature range between 20 °C and

[7] Sometimes the TTS is defined as the standard deviation σ of the distribution. In this work always the FWHM will be assumed unless otherwise noted.

[8] The length of the light pulse depends on the set intensity of the LED. These values are provided by the company. The uncertainty of σ_{LED} covers most of the given value range, excluding the ones at very high intensities.

[9] Assuming a flat distribution of length T, the standard deviation is calculated by $\sigma_{\mathrm{sam}} = \frac{T}{\sqrt{12}} = 230\,\mathrm{ps}$.

−50 °C yielding the results shown in figure 7.8. The TTS does not seem to be affected by temperature, in concordance with other measurements done with this PMT model [31 (p. 103)]. In the subsequent calculations and simulations in this thesis the average value (3.018 ± 0.017) ns will be used.

7.2 Quantum efficiency

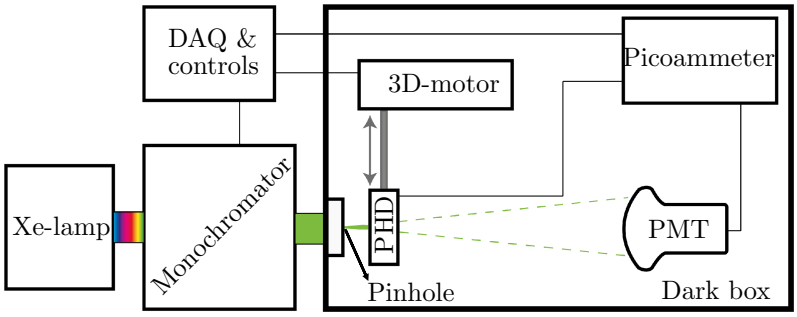

Fig. 7.9: Schematic drawing of the quantum efficiency setup. The photodiode is attached to a 3D-motor allowing to move the PHD into or out of the monochromatic light ray. The photocurrents of the PMT and PHD are measured by the picoammeter, which sends the data to the computer outside the dark box.

This section examines the wavelength dependence of the quantum efficiency (see 3.2.1) of the PMT. The experimental setup used for this measurements is illustrated in figure 7.9. The light of a Xenon-lamp[10] is fed into a remotely controllable monochromator[11], which selects a wavelength section of the whole spectrum. The resolution of the monochromator in this setup is (1.2 ± 0.6) nm (the slit aperture is 0.15 mm, see section 8.1.1). This monochromatic light is then guided through a pinhole into a dark box, where the PMT, a photodiode (PHD) and the picoammeter (a high precision amperemeter) are located. Additionally, the PHD is attached to a 3D-motor, which can move the diode into and out of the monochromatic light ray. The diode is calibrated (its QE is known) and is used for the acquisition of the reference photocurrent. The light beam diverges, illuminating most of the photocathode of the PMT, which is placed at a distance of ~ 1 m from the pinhole, but is also completely measured by the photodiode (which has a smaller sensitive area than the PMT) once it is located right in front of the pinhole.

In order to eliminate the effects of the collection efficiency, the PMT is connected to a base, which applies only the high voltage between the photocathode and the first dynode, while shorting out the multiplier system of the PMT. This way, photoelectrons can hit anywhere at the inner structure contributing to the output, although this reduces enormously the amplitude of the signal, as there is almost no electron multiplication. The applied high voltage during the measurement was 200 V, similar to the typical potential between the cathode and first dynode in normal operation. Due to the almost nonexistent gain ~ 1 from the PMT and PHD, the read-out is performed by the picoammeter, which is connected to a computer.

[10] LSDH102 lamp housing with a 75 W LSB511 Xe bulb by LOT QuantumDesign.
[11] MSH-300 with grating MSG-T-1200-300 by LOT QuantumDesign.

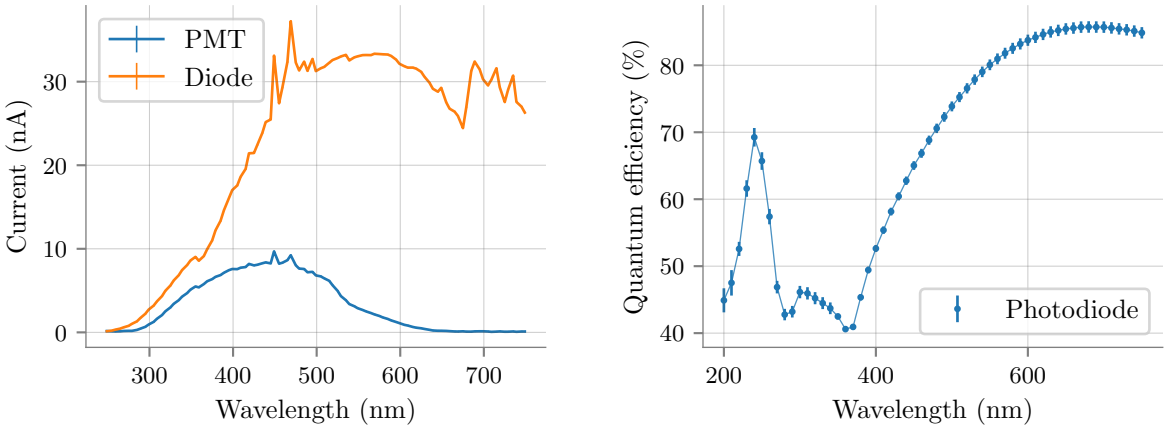

Fig. 7.10: Left: Current measured with the photodiode and the photomultiplier against the selected wavelength of the Xenon lamp spectrum. The statistical errors are smaller than the line width. **Right:** Quantum efficiency of the photodiode.

In this measurement, the average of 20 current measurements at each wavelength between 250 and 750 nm were taken in 5 nm steps, once with the photodiode and once with the PMT. Also, before and after the measurement the dark current of the devices is measured. For this the wavelength 1200 nm is selected, as the detectors are not sensitive in this range, and, in the case of the PMT, the photodiode is placed in front of the pinhole. For the dark current of the diode, the PHD is moved out of the light beam, in order to avoid incident light.

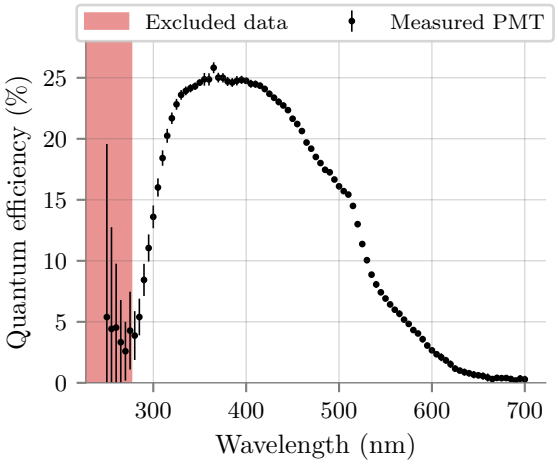

Fig. 7.11: Measured quantum efficiency in dependence of the wavelength.

The measured photocurrents are shown in figure 7.10. As there is practically no amplification, the currents of the two devices can be directly compared and the quantum efficiency of the PMT $QE_{\mathrm{PMT}}(\lambda)$ is derived from the known efficiency of the photodiode $QE_{\mathrm{diode}}(\lambda)$ (see figure 7.10) by

$$QE_{\mathrm{PMT}}(\lambda) = \frac{I_{\mathrm{PMT}}(\lambda) - DC_{\mathrm{PMT}}}{I_{\mathrm{diode}}(\lambda) - DC_{\mathrm{diode}}} \cdot QE_{\mathrm{diode}}(\lambda), \tag{7.3}$$

where $QE(\lambda)$ is the quantum efficiency for the wavelength λ, $I(\lambda)$ the measured current at λ and DC the average dark current.

Figure 7.11 shows the calculated QE of the PMT. It is to notice, that the uncertainty of the measurement increases in the UV-region. This is a measurement artefact due to the low intensity of the measured photocurrent, which drops to levels similar to the dark current. Also, the QE rises in the interval 250-265 nm, most probably attributable to effects from scattered light inside the monochromator. A small fraction of the output from the monochromator is scattered light from every wavelength of the light source. The spectrum of the Xenon lamp in the UV region is very dim and hence the intensity of the contamination can be similar or larger than the one from the selected wavelength,

overestimating the QE of the device being measured. Therefore the data points between 250-280 nm are excluded from every further calculation.

7.3 Average SPE pulse

As introduced in section 5.3, the Geant4 simulation used in this thesis can form waveforms given a curve that represents a single photoelectron pulse. Therefore the average SPE from the PMT in this setup is needed. For this, the PMT dark rate pulses are measured at room temperature, considering only the signals with a charge in the interval $Q_1 \pm \sigma_1$, where Q_1 is the mean charge of the SPE and σ_1 its standard deviation obtained from the calibration. In order to match the positioning of the pulses, each one is shifted so that its minimum lies at $t = 0$. The result of averaging ~ 3700 of such pulses is illustrated in figure 7.12. Noteworthy are the reflections, which are probably produced by the coupling between the cables and the amplifier, as this SPE can be compared with the pulse shown in figure 5.3, which was made from this same setup and PMT, but without the amplifier.

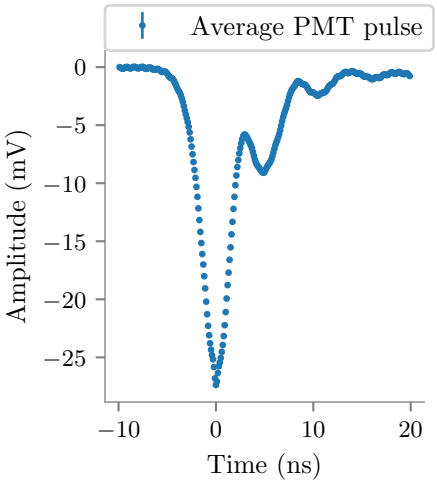

Fig. 7.12: Average SPE from the PMT connected to the amplifier.

Since the gain changes with temperature, also the SPE minima will vary. This is however not considered in the simulation and only the SPE at room temperature is used. Nevertheless, this should be still a good approximation for the purposes of this thesis, as the waveforms are simulated just for reasons of time resolution.

8 Measurement of scintillation parameters

In order to simulate the response of the optical modules to the luminescence background inside the vessel glass, it is important to rightfully parameterise this process. The theory behind the scintillation was already introduced in chapter 4. Empirically, the most important parameters are the energy distribution of the emission (scintillation spectrum), its lifetime, which determines the time distribution and the expected amount of emitted photons (scintillation yield). These three are also the default parameters needed for fully describing a scintillating material inside a Geant4 simulation. This chapter presents the method and results of the measurement of these parameters, starting with the scintillation spectrum (section 8.1), continuing with the lifetime (section 8.2) and at last the yield (section 8.3).

For practical reasons, the experiments done in the scope of this chapter used small glass samples, instead of a whole pressure vessel. The specimens of Vitrovex glass were provided in different thicknesses ranging from $\sim 2\,\mathrm{mm}$ to $\sim 10\,\mathrm{mm}$ by the manufacturer, while in the case of the Benthos glass a fragment of the pressure vessel of an IceCube DOM was cut into smaller square-shaped samples. Figure 8.1 shows a picture of most of these glass specimens. In the case of the gel, the samples can be made by mixing two liquid components, which vulcanises at room temperature to a soft gel after a few hours of curing time. Hence, the shape and thickness of the gel specimens can be constructed as needed for each setup.

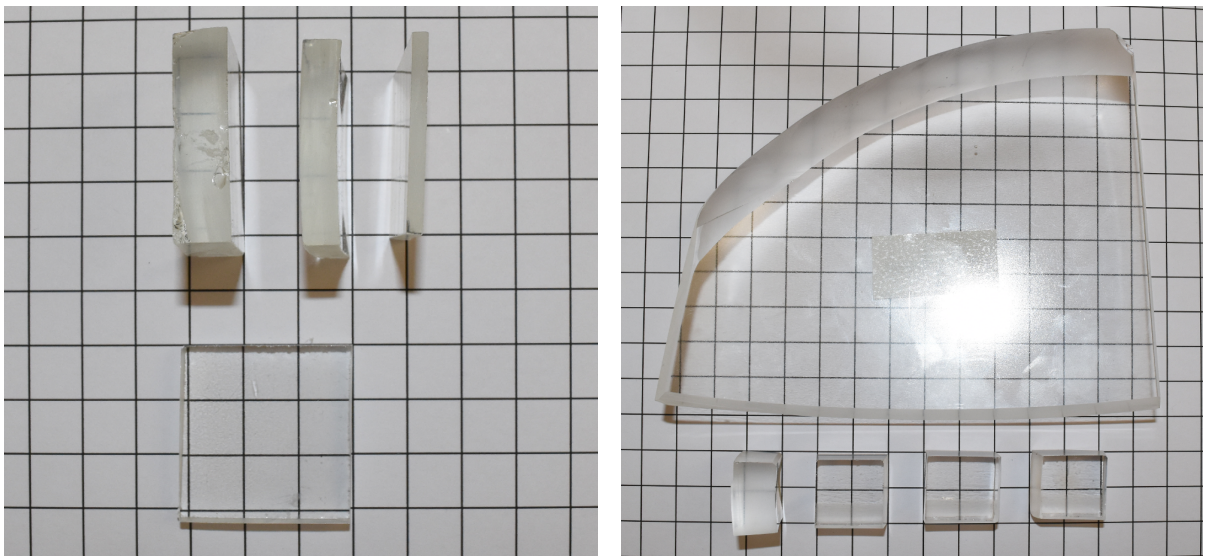

Fig. 8.1: Left: Some of the Vitrovex samples provided by the manufacturer, which have different thicknesses. These are on a square grid of side length 1 cm. **Right:** Fragment of the IceCubes DOM vessel (Benthos glass) with the smaller samples cut from it. The side length of the grid is 1 cm.

8.1 Scintillation spectrum

This section presents the results of the measurement of the scintillation spectrum of the different materials. First, the acquisition of the spectra is presented and explained. The results are afterwards corrected, compensating various influencing factors of the experimental method, such as the wavelength dependence of the QE of the PMT and the transmittance of the samples.

8.1.1 Raw scintillation spectra

The measurements of the scintillation spectra were conducted with the setup seen in figure 8.2. A radioactive source excites the sample, which then scintillates. The emitted light passes through the entrance slit of a remotely controllable monochromator[1], which filters the emission down to a narrow wavelength segment. Right after the exit slit of the monochromator is located a small PMT, which measures the output light in current mode (see section 3.1). The PMT is a Hamamatsu R7600U-200, which has a flat photocathode that can be placed in such a way that almost all the light emitted by the monochromator hits the PMT. Its photocathode material is ultra bialkali, which exhibits a higher QE in comparison to the normal bialkali of the Hamamatsu R12199-02. The PMT signal is measured with a picoammeter[2].

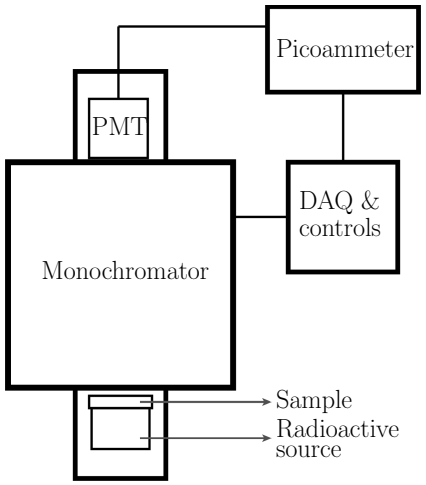

Fig. 8.2: Schematic of the scintillation spectrum measurement setup. The sample and the PMT are placed directly in front of the entrance and exit slit respectively.

For this measurement, it is indispensable that the samples scintillate intensely since only a small fraction of the emitted light is measured at a time. This makes necessary the use of a strong radioactive source. The first measurements were done with an ^{241}Am α-source, which had an approximate activity of $\sim$ 250 kBq. The average energy of the emitted alphas is 5.479 MeV [57], producing an energy deposition in the material of $\sim 0.7\,\mathrm{TeV}\cdot\mathrm{s}^{-1}$.

The intensity of the output light is directly dependent on the entrance and exit slit aperture. If the aperture of one of the slits is reduced by half, the intensity is also halved. Additionally, both slits should have the same aperture, meaning that by reducing the width to the half, the intensity is fourfold smaller. Their

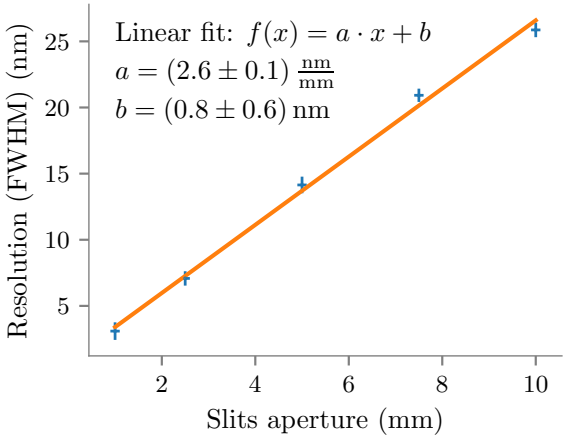

Fig. 8.3: Resolution of the monochromator output in dependence on the slits apertures. This was calculated measuring the FWHM of emission lines of a Hg lamp.

[1] LOT Quantum Design model MSH 300 with grating model MSG-T-1200-250.
[2] Keithley model 487.

aperture also determines the resolution of the monochromator. Figure 8.3 shows this dependency: the wider the slits, the broader the output light. Consequently, one has to make a compromise between the signal to noise ratio (SNR) and the resolution of the spectrum. For the measurement with the α-source the number of detected photons is low, yielding a fairly poor SNR. Therefore, a rather wide aperture of 2.5 mm was chosen, with which the resolution of the monochromator is (7.3 ± 0.7) nm.

For the measurement of the spectra, the intensity of the PMT current is measured in 2 nm steps for wavelengths between 250 and 650 nm. One data point delivered by the picoammeter is the mean current of the PMT in a period of 16.7 s. For one measurement cycle, the average of 100 of these data points was made for each wavelength. Depending on the sample, at least 15 cycles were carried out and then averaged, until the random noise was flattened. The resulting emission spectra of the specimens are depicted in figure 8.4.

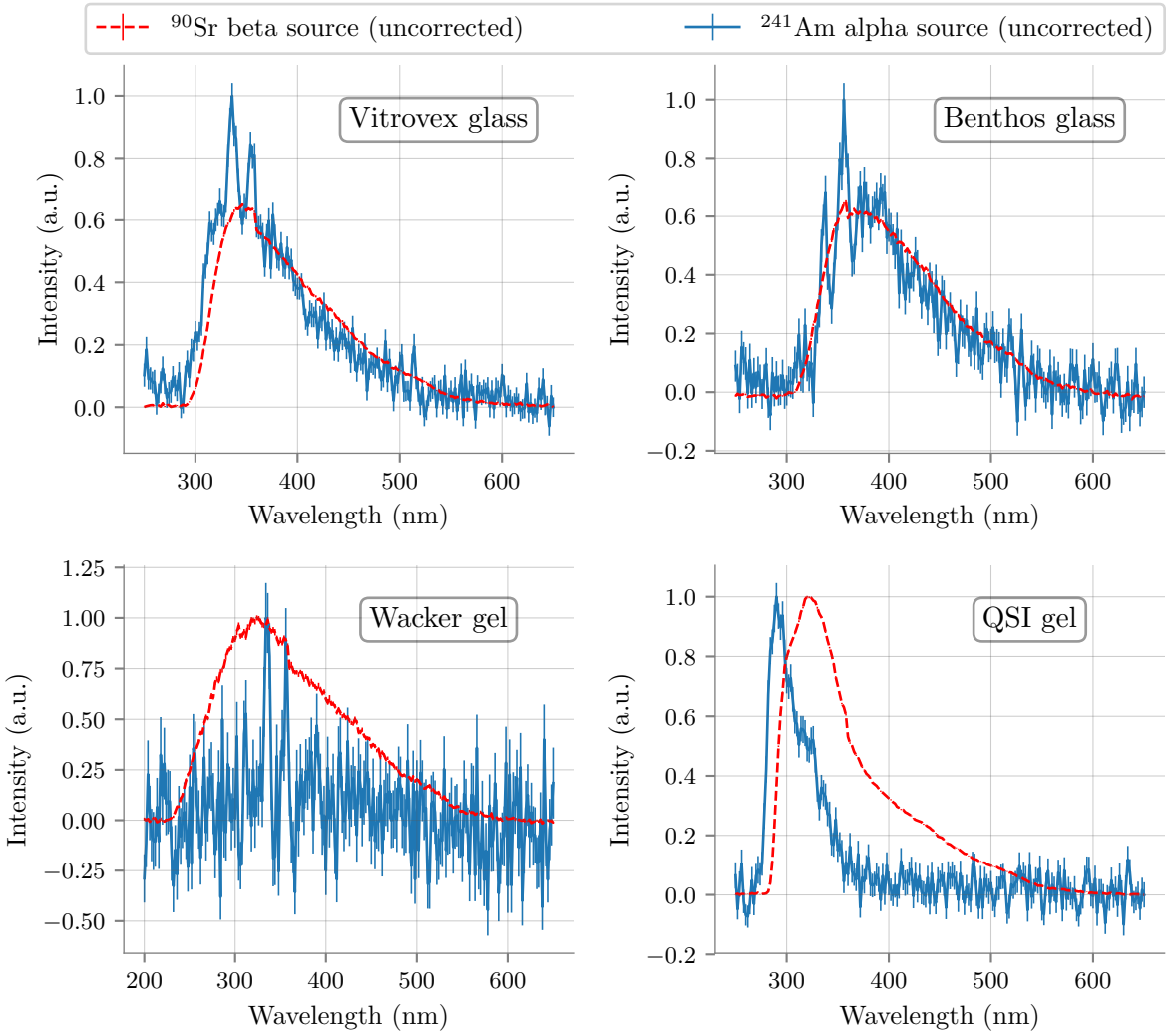

Fig. 8.4: Measured spectra of the four samples irradiated once with an ^{241}Am α- and then with a ^{90}Sr β-source. The results with ^{241}Am yield an inferior signal to noise ratio, as the energy deposition in the samples is far lower than the one achieved with the ^{90}Sr source.

It is noteworthy that for both glass samples, sharp peaks are present in the measured spectra. These peaks are located at the same wavelength (at $\sim$ 337 nm and $\sim$ 358 nm)

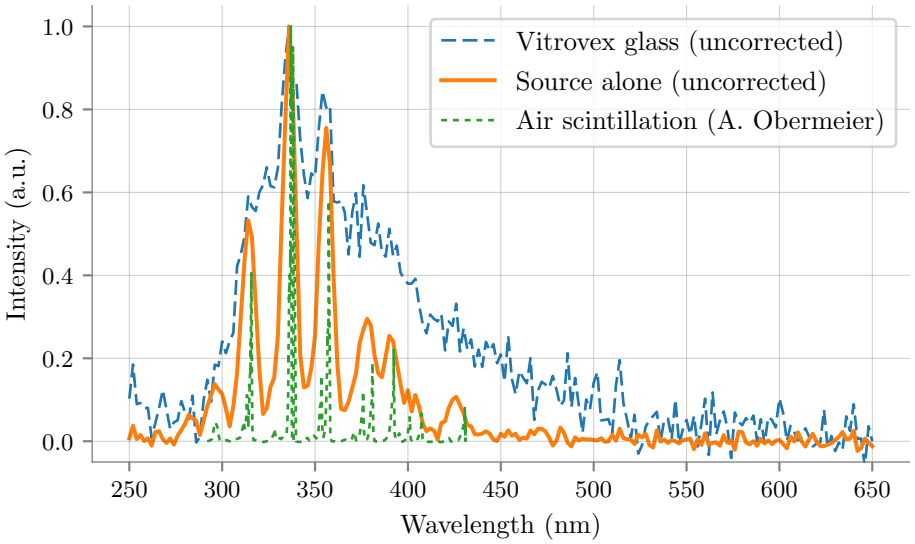

Fig. 8.5: Measurement of the air scintillation with the source facing no sample (solid line). For comparison, the measured Vitrovex glass spectrum is shown (blue dashed line), where the two largest peaks originating from air scintillation can be identified. As a reference, the measurement of air scintillation with 3 MeV electrons is also presented (green dashed line). Data was taken from [58].

suggesting the presence of an external light contamination in the setup. For these samples, the distance to the α-source was approximately $\sim 0.5\,\mathrm{mm}$, as the source is protected by a ring of this height. In the case of the Wacker gel no signal was measured over the background, only traces of the mentioned peaks. The QSI gel sample was small enough in order to be placed without any gap in between the source and the gel. As the measurement of the latter does not show any light contamination, the peaks are most probably being produced by air-scintillation. To confirm this, the α-source was measured without any sample in front of it. The results are presented in figure 8.5. It is noteworthy that the same peaks are found as in the samples, besides others less intense, which coincide with a reference measurement from Obermeier et al. of air-scintillation done with a 3 MeV electron beam [58]. This discrete emission can be traced back to electronic transitions from molecular nitrogen [58].

Owing to the constraints presented by the measurement with the ^{241}Am source, the low SNR, reduced resolution and air-scintillation, another measurement with ^{90}Sr with an activity of $\sim 0.4\,\mathrm{GBq}$ was done. ^{90}Sr is a beta source with a mean energy of $(195.8 \pm 0.8)\,\mathrm{keV}$ and decays into ^{90}Y [57]. The latter also undergoes beta decay with a mean energy of $(933.7 \pm 1.2)\,\mathrm{keV}$. As the half-life of the yttrium isotope ($(64 \pm 2)\,\mathrm{h}$) is much lower than the one of its mother nucleus ($(28.8 \pm 0.1)\,\mathrm{y}$), they are in secular equilibrium. With both isotopes, the yielded energy deposition in the sample is around $\sim 225\,\mathrm{TeV} \cdot \mathrm{s}^{-1}$. A beta source features the advantage that electrons have a longer range in the air than alpha particles. While these are completely absorbed after a few centimetres, betas exhibit a range in the order of metres. This reduces the amount of energy released into the air and thus the probability of detecting light stemming from it. Accordingly, this also means that the sample has to be thicker for the energy to be completely absorbed in the material. The thicker the sample is, the more scintillation photons will be absorbed in the material, losing sensitivity of the spectrum and changing its shape, especially in the UV region, as

it is shown with the transmission curves of figure 2.7.

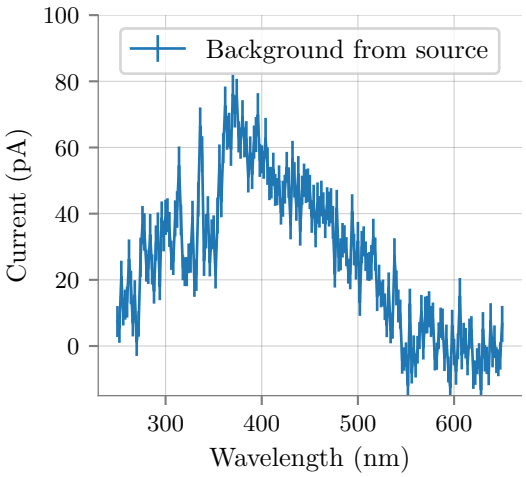

Fig. 8.6: The spectrum of the light originating from inside the ^{90}Sr source.

The light emitted by the samples was strong enough in order to take long exposure pictures with a DSLR camera[3]. The photos are depicted in figure 8.7. Apart from the scintillation itself, small green spots can be seen. Comparing the photo from the source (see figure 8.7 top right) with the long exposure picture (see figure 8.7 bottom right), one can see that the light is coming from inside the source. The ^{90}Sr is encapsulated in glass and a very thin layer of steel. The light may be produced by scintillation of the glass capsule and then escapes the steel layer, which seems to be worn-out in some areas. The spectrum of this background is depicted in figure 8.6 and with an intensity of tens of pA it is two orders of magnitude smaller than the scintillation of the samples ($\mathcal{O}$(nA)). Hence, the influence of this contamination on the spectra is negligible.

The results with the ^{90}Sr source are illustrated in figure 8.4. It can be seen that for both glass samples the measured spectra are similar to the one obtained with the α-source. Though, the UV-cut-offs from the spectra of the Vitrovex glass are different. For the ^{241}Am source a sample with $\sim 1\,$mm thickness was used (the range of α-particles is $\mathcal{O}(\mu$m) in glass) and for the ^{90}Sr one of $\sim 1\,$cm (the range of β-particles in the energy spectrum emitted by the source is $< 0.6\,$cm in glass). As the absorption length in UV is very small, a wider sample causes a shift in the UV-cutoff to larger wavelengths. This was not the case for the Benthos glass, as the same sample was used for both measurements. This effect is most noticeable with the QSI gel spectra, as the sample thickness for the α-source was very thin ($\sim 0.3\,$mm) and for the measurement with ^{90}Sr it was $\sim 15\,$mm absorbing the maximum of the emission and modifying its shape and position. Furthermore, the spectrum with the β-source features a tail at higher wavelengths. This is probably caused by Cherenkov radiation from the sample, as the Cherenkov energy threshold for electrons in glass and gel is around $\sim 200\,$keV (see section 2.3), lower than the energy of most of the emitted electrons. This is not seen with the ^{241}Am source, as the threshold for alpha particles is $\sim 1.5\,$GeV. Cherenkov radiation should also explain the emission shown by the Wacker sample, as no signal was measured with the α-source. This will be verified in the next section 8.1.2 simulating the Cherenkov emission from the sample.

For the glass samples, both sources yield a similar spectrum. However, it is difficult to estimate how much the spectra of the glass samples are being modified by Cherenkov radiation, as the ones measured with the ^{241}Am source were contaminated with air-scintillation and thus there is no reference to compare with. Besides, especially at the Vitrovex glass spectrum, the intensity is higher at wavelengths between 400-500 nm, which could be a consequence of Cherenkov photons. Air also scintillates in this zone, which could mean that the glass scintillates only at lower wavelengths. Nevertheless, as this cannot be corrected, the spectra measured with ^{90}Sr will be used from now on, as they show a much

[3]Nikon D5500 with an AF-S 18-55 VR lens

better signal to noise ratio. For the QSI gel sample, the spectrum with the ^{241}Am source will be used in further calculations, as there is a clear loss of information due to sample absorption and contamination from Cherenkov light in the results with the ^{90}Sr source. The next section presents the correction of these spectra.

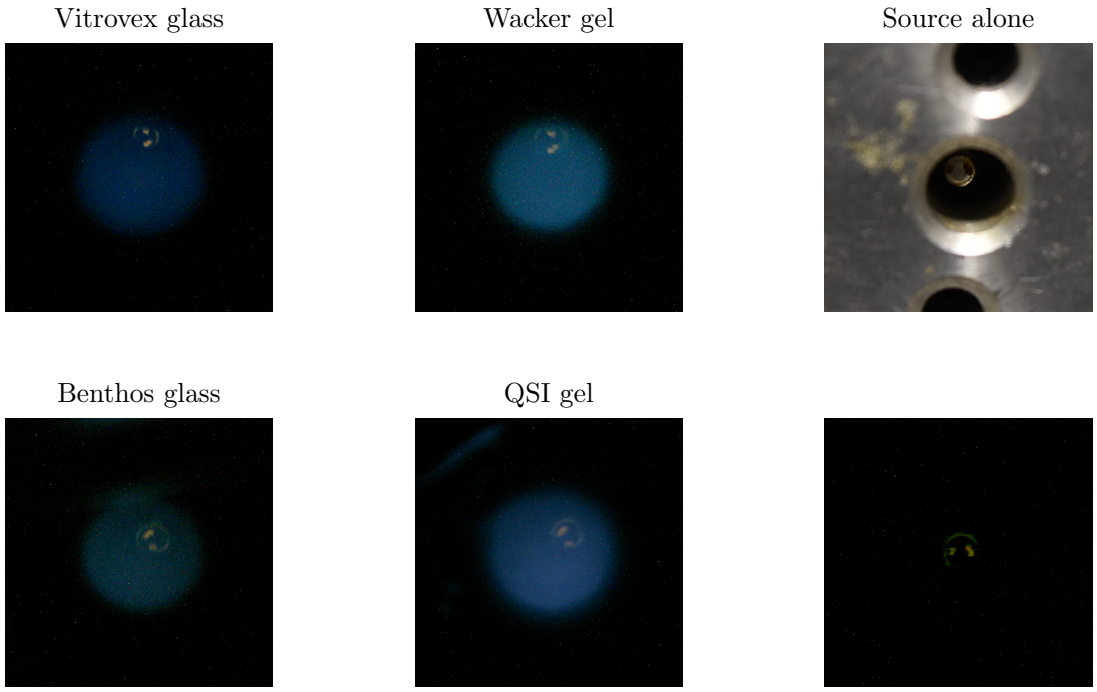

Fig. 8.7: Long exposure (15 min) photos from the glass and gel samples emitting light (left, centre), as well from the source itself (right).

8.1.2 Correction of the spectra

Three components modify the emitted spectrum. First, the efficiency of the grating inside the monochromator is wavelength dependent. The data provided by the manufacturer is shown in figure 8.9. One can notice that there is no cutoff coming from the grating, as its efficiency never falls to 0 % in the measured wavelength interval, but there is nevertheless a change in the shape of the input and output spectrum, which has to be corrected.

Then, there is the quantum efficiency of the PMT. This is measured with the same setup as the one explained in section 7.2. The results are displayed in figure 8.10. The data in the UV region is here excluded as well (see explanation in section 7.2).

At last, there is the absorption of the light in the sample. This depends on the absorption length of the material and the distance travelled by the photons inside the sample. In the case of the measurements with ^{90}Sr source, it is not trivial to calculate it analytically, as the electrons scatter in different directions and depths depending on their energy. Also the stopping power of the electrons is energy dependent, and hence the amount of emitted light will vary at different depths of the sample. To take all these variables into account, the transmission is determined with a Geant4 simulation.

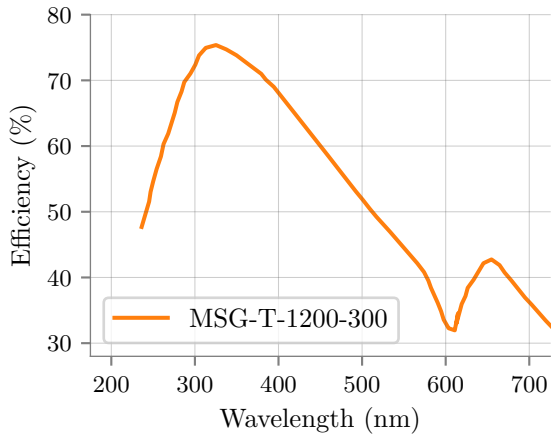

Fig. 8.9: Grating efficiency for the wavelength interval used in the measurement.

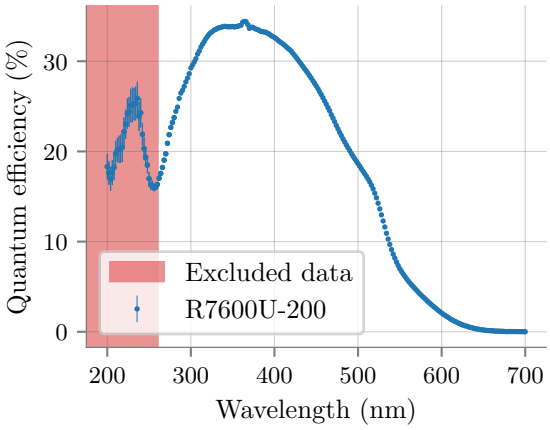

Fig. 8.10: Quantum efficiency of the PMT. The red zone marks the excluded data.

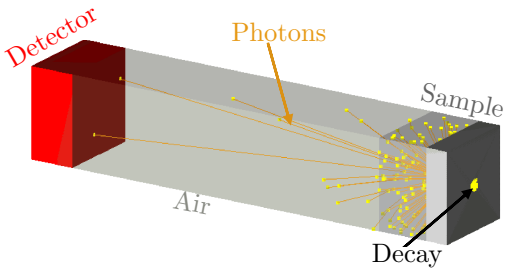

Fig. 8.8: Geometry in the Geant4 simulation of the scintillation transmission.

Figure 8.8 shows the simulated geometry. At each event, a decay of ^{90}Sr and ^{90}Y is simulated emitting electrons isotropically. The isotopes are placed 1 cm in front of the sample and are enclosed with aluminium, imitating the source geometry (see figure 8.7). Some of the emitted betas hit the sample, which then scintillates with a flat spectrum between 200 nm and 800 nm. Cherenkov radiation is not included in the simulation, to not contaminate the results. The simulated sample has the same thickness as in the measurement (Vitrovex glass (10.4 ± 0.1) mm, Benthos glass (11.4 ± 0.1) mm and QSI gel (0.3 ± 0.1) mm), and the same data for the absorption length is used, as for the mDOM simulation. A "detector" is placed at a distance of 10 cm from the sample, saving the wavelength of all the photons that hit this volume. A corresponding simulation was made for the QSI gel spectrum, but simulating ^{241}Am isotopes instead of the ^{90}Sr and ^{90}Y. The relative transmission is then created by displaying the wavelength of the detected photons as a histogram. The normalised relative transmission is presented in figure 8.11.

The corrected emitted scintillation spectrum $S_c(\lambda)$ at wavelength λ can be calculated dividing the measured intensity $S_m(\lambda)$ by the transmission $T(\lambda)$ of the sample, the efficiency of the grating $GE(\lambda)$ and the quantum efficiency $QE(\lambda)$:

$$S_c(\lambda) = \frac{S_m(\lambda)}{T(\lambda) \cdot GE(\lambda) \cdot QE(\lambda)}. \tag{8.1}$$

The results are displayed in figure 8.11. The figure shows a portion of the measured wavelength interval, as the relative noise at small and large wavelengths gets amplified by small values of the transmission and quantum efficiency. This can be seen in the spectrum of Benthos glass, where the errors at smaller wavelengths are large, as the absorption is substantial in this area.

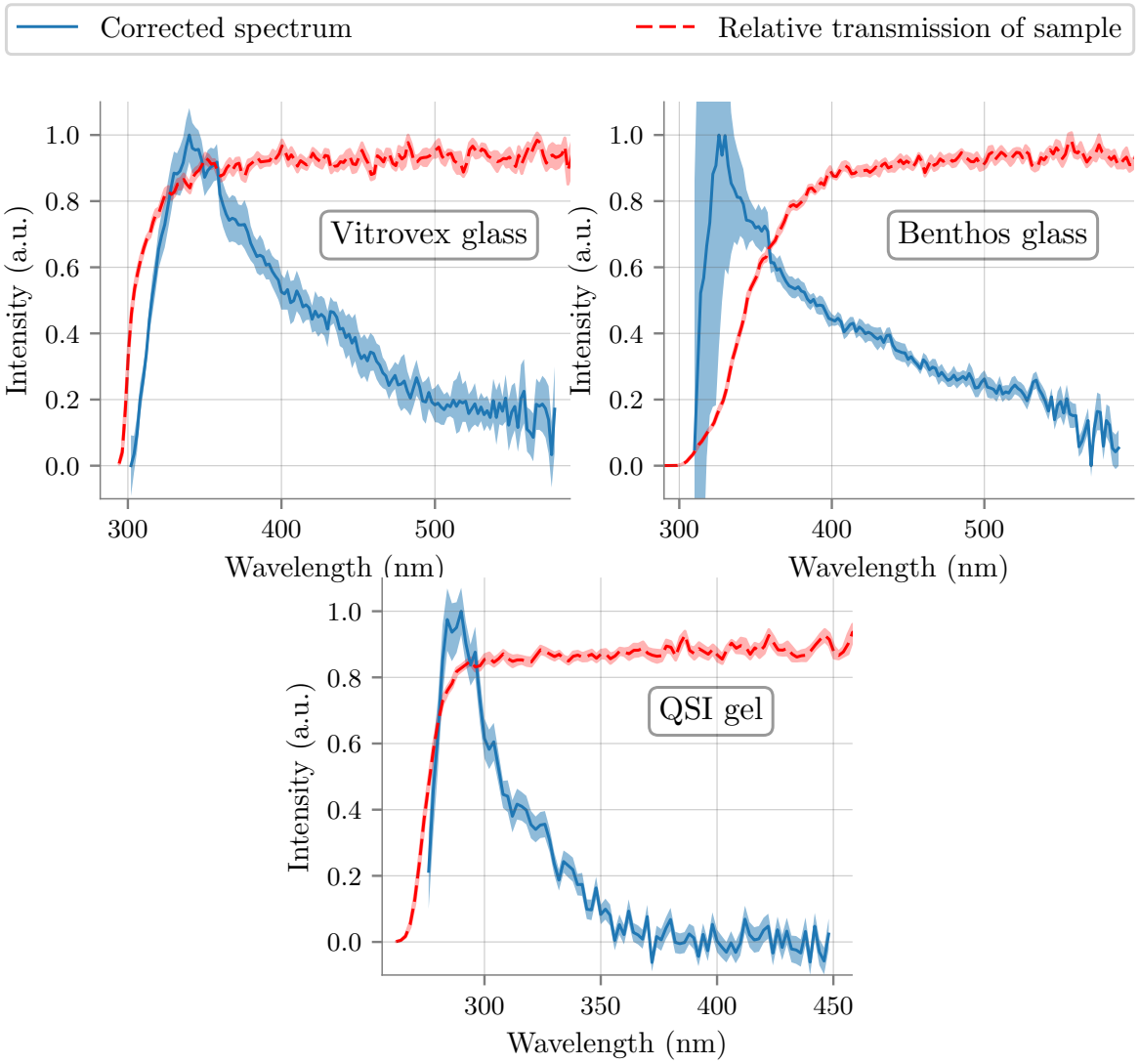

Fig. 8.11: Corrected spectra of both glass and the QSI gel samples (blue) and their relative transmission for scintillation photons (red). The uncertainty is depicted as a desaturated band around the data marker line. The maximum emission for these three samples occurs just at the UV-cutoff of the transmission.

Finally, these corrected spectra are included in the Geant4 simulation for further calculations, although the QSI gel spectrum gets cut at 375 nm, as at higher wavelength there is only noise that fluctuates around zero.

Using the simulation described before, one can also test the claim made in the previous section, that the spectrum measured with the Wacker gel sample being excited by the ^{90}Sr source was, in fact, only Cherenkov light. For this, the scintillation is deactivated in the code, while the Cherenkov effect is included again in the physics list. Apart from that, the simulation is identical to the one of the sample transmission. This way, the transmission of the Cherenkov spectrum is calculated instead for a flat one. In order to compare the results of the simulation with the measurement, the QE of the PMT and the grating efficiency is multiplied by the simulated transmission. The results are depicted in figure 8.12. The simulated spectrum exhibits a cutoff at 260 nm, as this is the first data point from the QE of the PMT. Starting from this wavelength, however, the curve is similar to

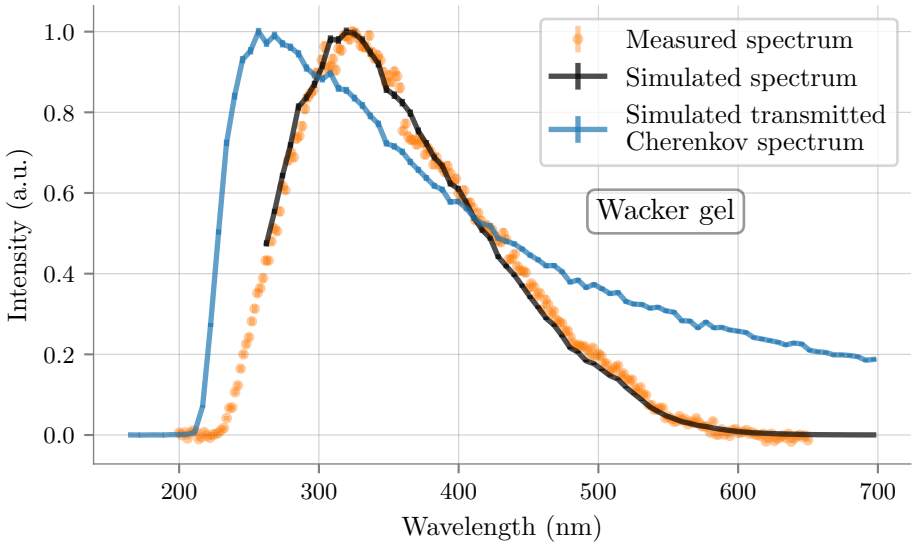

Fig. 8.12: Comparison between the simulated and measured spectrum of the Wacker gel sample. The transmission for the Cherenkov spectrum produced by ^{90}Sr and ^{90}Y decays was simulated (blue curve) and then multiplied with the QE of the PMT and the efficiency of the monochromator's grating (black line) in order to be compared with the measurement (orange dots).

the measured one, which supports the premise.

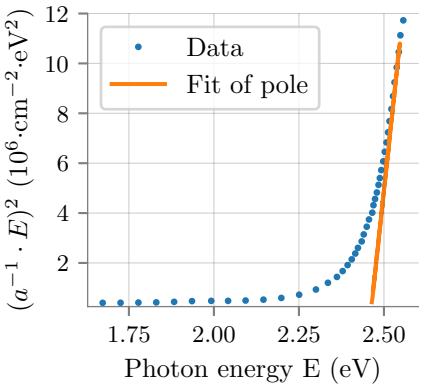

Fig. 8.13: Tauc diagram of a bismuth silicate glass based on its absorption length a. Data taken from [59]. The linear fit of the divergence pole is extrapolated to the abscissa, which determines the band gap energy level of the material.

The measured scintillation spectra feature their maxima always very close to the absorption cutoff of the samples. This means that the emission results from transitions with similar energies as the optical band gap. The latter can be easily calculated using the absorption length a by means of a Tauc diagram [60 (p. 444)]. Here $(\frac{E}{a})^n$ is plotted against the photon energy (E), where n denotes the nature of the band gap ($n = 1/2$ for direct, $n = 2$ for indirect ones). Then the pole for $(a \to 0)$ is extrapolated to the abscissa, which yields the band gap energy level. An example is shown in figure 8.13. For this, however, the absorption length near the cutoff $(a \to 0)$ has to be known very precisely ($a \sim \mathcal{O}(\mu\mathrm{m})$). The data of the samples currently used has only the absorption length down to the millimetre range. Nevertheless, the optical bandgap energy level will be between the smallest a of the data and $a = 0\,\mathrm{mm}$. For the Vitrovex glass this corresponds to the wavelength between 296.6 nm and 299.8 nm, for Benthos between 290 nm and 300 nm, QSI gel 270 nm and 280 nm and lastly Wacker gel in the range from 200 nm to 210 nm. This could explain that no light was detected from the Wacker specimen. As the PMT only can measure photons down to $\sim 250\,\mathrm{nm}$, the emission would not get detected, if this lies in the wavelength range near the absorption cutoff, as is the case with the other specimens.

8.2 Lifetime

This section presents the results of the lifetime measurement of the glass and gel sample scintillation. First, the acquisition and calculation of the time distributions is explained in section 8.2.1. Further these results are corrected in section 8.2.2, due to limitations of the detection method.

8.2.1 Measuring the time distribution

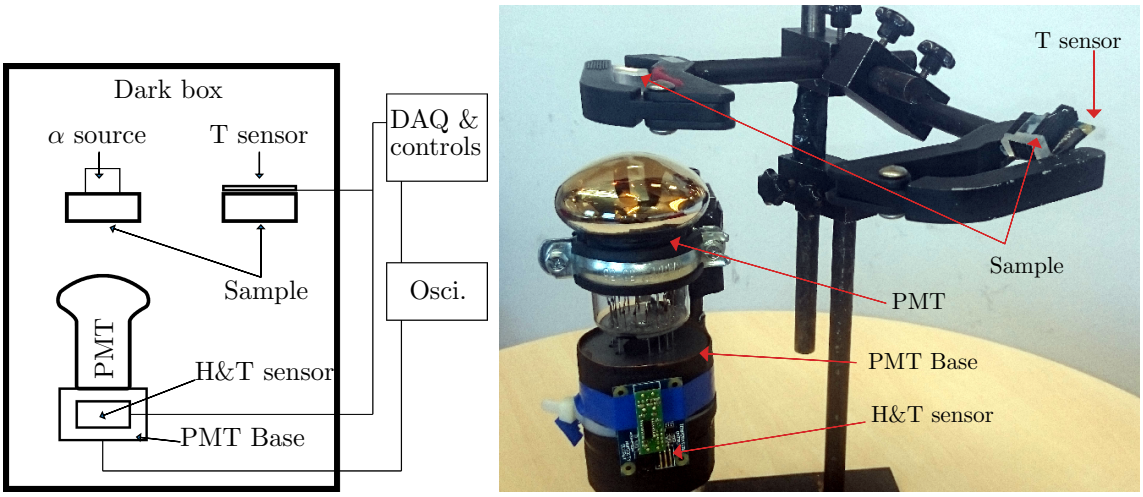

Fig. 8.14: Left: Schematic drawing of the lifetime measurement setup. The dark box is located inside the climate chamber for the temperature regulation. Not shown in the sketch is the amplifier between PMT and oscilloscope and the high voltage supplier for the PMT. **Right:** Picture of the setup inside the dark box. T stands for temperature and H for humidity.

Figure 8.14 illustrates the experimental setup of the lifetime measurement. The samples are excited by an alpha source and the scintillation is measured by the PMT located in front of the sample. These are placed inside a light-tight box inside the climate chamber. For recording the humidity and temperature, a sensor is placed on the PMT base and a second sample with a temperature sensor is placed at the same height as the first specimen. In order to maximise the heat transfer, the sample and the sensor are connected via thermal grease. This is necessary since the thermal conductivity of the sample and the PMT base are different and it is not possible to place the sensor on the studied specimens, as they are small.

The signal of the PMT is measured with an oscilloscope[4] with self-trigger. For every trigger event, a waveform of the next 100 μs is processed, saving the arrival time, charge and amplitude of every signal that surpasses the trigger of -18 mV. This is done for 200000 events at temperatures between -45 °C and -15 °C in 10 °C steps, including one at -50 °C, which is the lowest temperature endurable by the temperature sensors. The measurement starts when both temperature sensors read a value at most 0.2 °C away from the target temperature. With this data, it is possible to make a histogram of the arrival times, which corresponds roughly to time distribution of the emission. Two examples of such distributions are shown in figure 8.15. The glass samples show a rather long

[4] PicoScope 6404C

emission and their histogram is thus affected by the correlated noise, especially by the late afterpulsing (see section 3.2.4), which appears at around 3 μs and thus has to be corrected for further calculations. This can be done by replacing the source and sample with a pulsed LED, which emits nearly exclusively SPE at approximately the same rate as the emission with the source. Processing the same number of events, the resulting histogram does not only show the correlated signals, but also the effects of random noise, as the LED only causes the first photon of the waveform. Subtracting this distribution to the one measured with the samples, results in a better approximation of the real emission (see the left plot of figure 8.15). For the gel samples this is done analogously, although as their scintillation is very fast (<200 ns), the correlated noise in this range does not significantly affect the measurement. This is presented on the right side of figure 8.15.

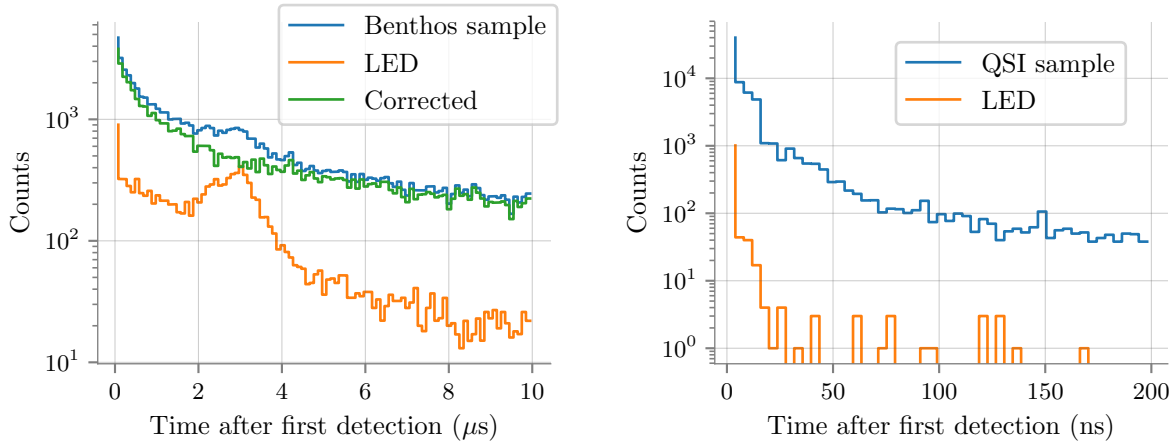

Fig. 8.15: Time distributions of the emission from the Benthos glass (left) and QSI gel sample (right) at −15 °C. In order to remove the afterpulsing, the correlated noise was measured by triggering the first event with the emission of an LED and subtracted from the distributions. The corrected distribution for the gel sample is not shown, as the difference with the original cannot be noticed visually.

These distributions were fitted with multi-exponential decays (see equation 4.7) and a constant. The best fit for the glass and QSI gel sample was achieved with three exponential decays and for the Wacker gel sample with two. Here it is important to start making the fits with histograms with a very fine binning, as this defines the resolution for the possible measurable lifetimes. Once the shortest time constant is found, it is possible to make a rebinning for better statistics. For the glass samples the fits were done with a final bin width of 20 ns and for the gel samples of 1 ns.

Instead of the amplitude α_i, a more relatable parameter for describing the exponential decays are the fractional contributions f_i since they can be interpreted as the percentage of photons emitted by each component. It is given by

$$f_i = \frac{\alpha_i \tau_i}{\sum_j \alpha_j \tau_j}, \tag{8.2}$$

where τ_i is the lifetime and $\alpha_i \tau_i$ the total number of detected photons stemming from the component i. The fits of the time distribution of the four materials at −15 °C are illustrated in figure 8.16. Table 8.1 summarises the resulting fit parameters of the glass and gel samples respectively.

Table 8.1: Fit parameters with a multi-exponential decay for measured time distributions of the glass and gel samples at different temperatures. The best fit was achieved with three exponential decays, except for the Wacker gel emission, which shows a two-exponential decay emission.

Vitrovex glass					
	−15 °C	−25 °C	−35 °C	−45 °C	−50 °C
f_1	0.132 ± 0.004	0.119 ± 0.004	0.113 ± 0.004	0.117 ± 0.004	0.123 ± 0.004
τ_1 (ns)	356 ± 9	334 ± 9	323 ± 9	321 ± 9	377 ± 10
f_2	0.362 ± 0.008	0.354 ± 0.008	0.345 ± 0.008	0.336 ± 0.008	0.331 ± 0.008
τ_2 (μs)	2.84 ± 0.06	2.70 ± 0.06	2.66 ± 0.06	2.63 ± 0.06	2.99 ± 0.07
f_3	0.506 ± 0.009	0.527 ± 0.009	0.542 ± 0.009	0.547 ± 0.009	0.546 ± 0.010
τ_3 (μs)	19.3 ± 0.4	18.6 ± 0.4	20.1 ± 0.4	19.3 ± 0.5	23.5 ± 0.7
$\overline{\tau}$ (μs)	10.8 ± 0.3	10.8 ± 0.3	11.9 ± 0.3	11.5 ± 0.4	13.9 ± 0.4
Benthos glass					
f_1	0.158 ± 0.007	0.155 ± 0.007	0.142 ± 0.006	0.142 ± 0.007	0.134 ± 0.006
τ_1 (ns)	357 ± 12	391 ± 13	321 ± 11	345 ± 13	308 ± 12
f_2	0.309 ± 0.013	0.324 ± 0.013	0.309 ± 0.012	0.308 ± 0.013	0.304 ± 0.012
τ_2 (μs)	2.75 ± 0.10	3.04 ± 0.11	2.52 ± 0.09	2.52 ± 0.10	2.38 ± 0.09
f_3	0.533 ± 0.014	0.521 ± 0.015	0.550 ± 0.013	0.550 ± 0.014	0.562 ± 0.013
τ_3 (μs)	18.2 ± 0.6	20.0 ± 0.7	19.5 ± 0.6	17.6 ± 0.6	16.9 ± 0.5
$\overline{\tau}$ (μs)	10.6 ± 0.4	11.5 ± 0.5	11.5 ± 0.5	10.5 ± 0.4	10.3 ± 0.4
Wacker gel					
f_1	0.826 ± 0.018	0.787 ± 0.016	0.784 ± 0.016	0.781 ± 0.015	0.775 ± 0.016
τ_1 (ns)	11.57 ± 0.13	12.06 ± 0.14	12.71 ± 0.14	12.82 ± 0.14	13.09 ± 0.15
f_2	0.174 ± 0.018	0.213 ± 0.016	0.216 ± 0.016	0.219 ± 0.015	0.225 ± 0.016
τ_2 (ns)	126 ± 13	119 ± 9	119 ± 9	115 ± 8	115 ± 8
$\overline{\tau}$ (ns)	31.5 ± 3.2	34.8 ± 2.7	35.7 ± 2.7	35.2 ± 2.5	36.0 ± 2.6
QSI gel					
f_1	0.762 ± 0.011	0.787 ± 0.013	0.798 ± 0.011	0.801 ± 0.011	0.796 ± 0.011
τ_1 (ns)	1.009 ± 0.017	1.100 ± 0.016	1.093 ± 0.016	1.075 ± 0.015	1.064 ± 0.016
f_2	0.183 ± 0.010	0.136 ± 0.009	0.121 ± 0.008	0.105 ± 0.008	0.100 ± 0.008
τ_2 (ns)	8.58 ± 0.29	11.0 ± 0.6	10.7 ± 0.6	10.0 ± 0.6	10.2 ± 0.7
f_3	0.055 ± 0.007	0.077 ± 0.0012	0.081 ± 0.009	0.094 ± 0.008	0.104 ± 0.009
τ_3 (ns)	40.9 ± 2.7	39.9 ± 2.8	50.7 ± 2.9	50.6 ± 2.4	48.6 ± 2.3
$\overline{\tau}$ (ns)	4.6 ± 0.4	5.4 ± 0.3	6.3 ± 0.5	6.7 ± 0.5	6.9 ± 0.5

As the fits deliver 7 parameters in the case of a triple-exponential decay and 5 in the case of a double one, it is difficult to have an overview of the lifetime change at different temperatures. Furthermore, the parameter α_i and τ_i are correlated, and therefore results from two different measurements cannot be compared easily. In this regard, it is useful to determine the average lifetime $\overline{\tau}$, which is given by

$$\overline{\tau} = \sum_i f_i \cdot \tau_i. \tag{8.3}$$

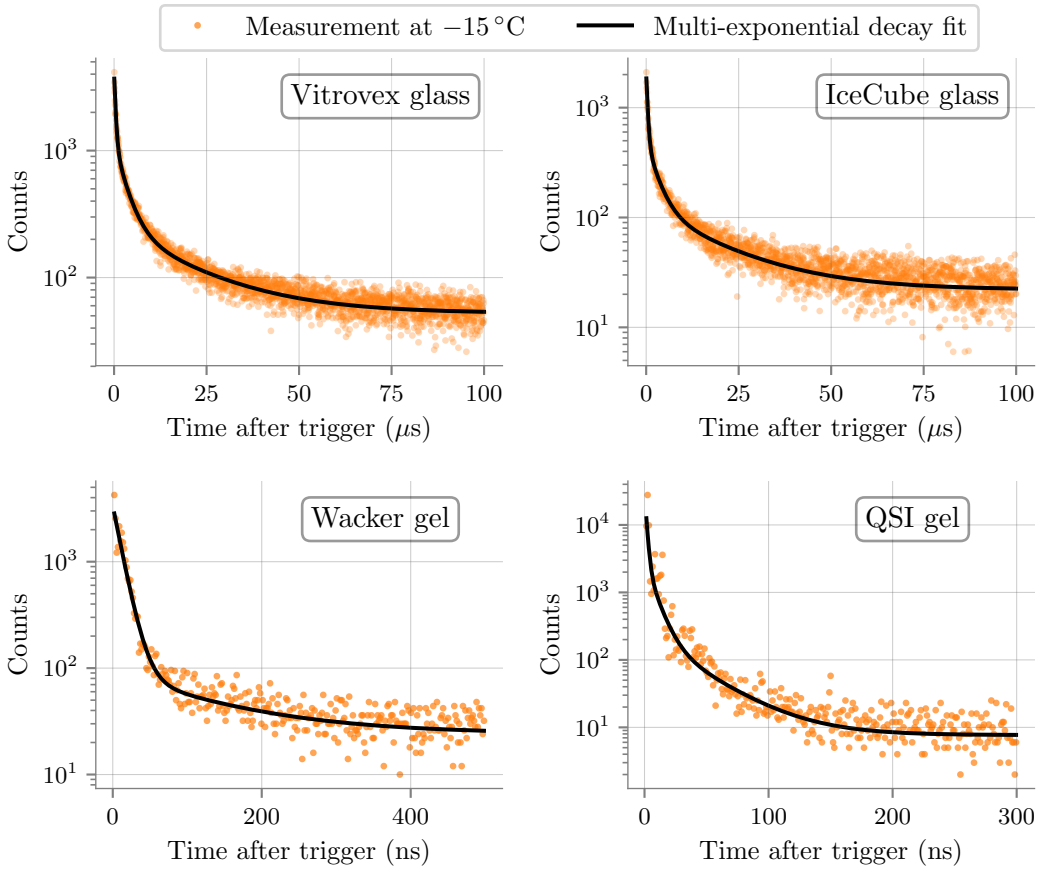

Fig. 8.16: Time distribution of the emission of the four samples at −15 °C, after subtracting the correlated noise. The fits using multi-exponential decays are shown with a black line.

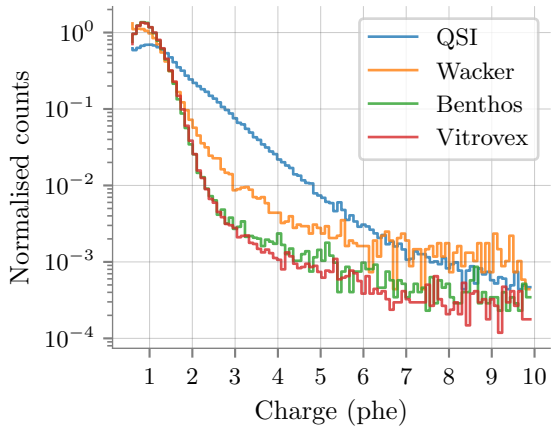

Fig. 8.17: Charge distribution of the pulses forming the decay curves at −15 °C.

The average lifetimes of the distributions are also summarised in table 8.1. The results for the glass samples are very similar, exhibiting an average time constant of around $\sim 10\,\mu$s. There seems to be an increase of the lifetime with lower temperatures, although not by much. The gel samples, on the other side, exhibit a much faster emission with an average time constant of approximately ~ 5 ns (QSI) and ~ 35 ns (Wacker), and a more distinguishable slowing down of the emission at colder environments.

The emission of the gel samples is probably faster than measured, as the time resolution (TTS) of the PMT plays a role in this range. Especially for the QSI sample with its time constant component of ~ 1 ns the probability of detecting two photons without being able to distinguish them is quite high. This can be tested by comparing the charge histograms of the detected scintillation, which is illustrated in figure 8.17. It is noteworthy, that while with the glass sample almost exclusively SPE signals are measured

(mean charge (1.067 ± 0.001) phe and (1.053 ± 0.002) phe with Vitrovex and Benthos respectively), the gel samples present a more considerable amount of multi-photoelectron events. The charge distribution of the emission of the Wacker gel sample has an average of (1.177 ± 0.003) phe and the one of the QSI gel of (1.615 ± 0.002) phe, which is to be expected, as the latter exhibits the fastest emission. This has as a consequence that the time distribution has fewer counts towards shorter times. For the emission of the Wacker gel, this distortion should not be significant, as most events were SPE pulses, but this is not the case for the QSI emission. One possible correction method tested in the scope of this thesis was to use weighed events by their charge. However, this distorted the distributions and made the subtraction of the correlated noise not doable. Because of the time constraints, a correction of this effect could not be done. Nevertheless, in the context of the dark rate, a parameter of 1 ns is already well below the time resolution of the PMT (~ 3 ns, see section 7.1.3) and thus it should not make a difference if this is even faster.

8.2.2 Correction of the lifetime

Why is a correction needed? A toy model

Since in the experiment the first measured photon is used as the trigger and is assigned $t = 0$, the results are distorted towards slower scintillation times. This effect can be best described in a simplified model of the measurement. Lets assume a triple-exponential decay with lifetimes τ_i, time constant $\lambda_i = \tau_i^{-1}$, and amplitude α_i:

$$\sum_{i=1}^{3} \alpha_i \exp(-\lambda_i \cdot t), \qquad f_i = \frac{\alpha_i \tau_i}{\sum_j \alpha_j \tau_j}$$

where f_i is the fractional contribution of each component. If we measure two photons from this distribution, the probability that the first stems from the component l and the second from k is

$$\begin{aligned}\int_0^\infty P(t;\lambda_l) \cdot \Big(\int_t^\infty P(t';\lambda_k) \cdot dt' \Big) \cdot dt &= \int_0^\infty \lambda_l \exp(-\lambda_l \cdot t) \cdot \Big(\int_t^\infty \lambda_k \exp(-\lambda_k \cdot t') \cdot dt' \Big) \cdot dt \\ &= \int_0^\infty \lambda_l \exp(-(\lambda_l + \lambda_k) \cdot t) \cdot dt \\ &= \frac{\lambda_l}{\lambda_l + \lambda_k},\end{aligned}$$

where $P(t;\lambda)$ is the probability density function of an exponential distribution with time constant λ. If in the measurement only two photons are detected per decay, only the last photon will contribute to the measured time distribution.

By calculating the probability that the second measured photon is from the component k, the reconstructed fractional contribution $\widetilde{f_k}$ can be written as

$$\widetilde{f_k} = f_k^2 + 2 \cdot \frac{\lambda_l}{\lambda_l + \lambda_k} f_l \cdot f_k + 2 \cdot \frac{\lambda_m}{\lambda_m + \lambda_k} f_m \cdot f_k. \tag{8.4}$$

The first term of the equation 8.4 is the probability for both detected photons stemming from the distribution k, the second and third term includes the probability of measuring one photon of l or m followed by one of the k component.

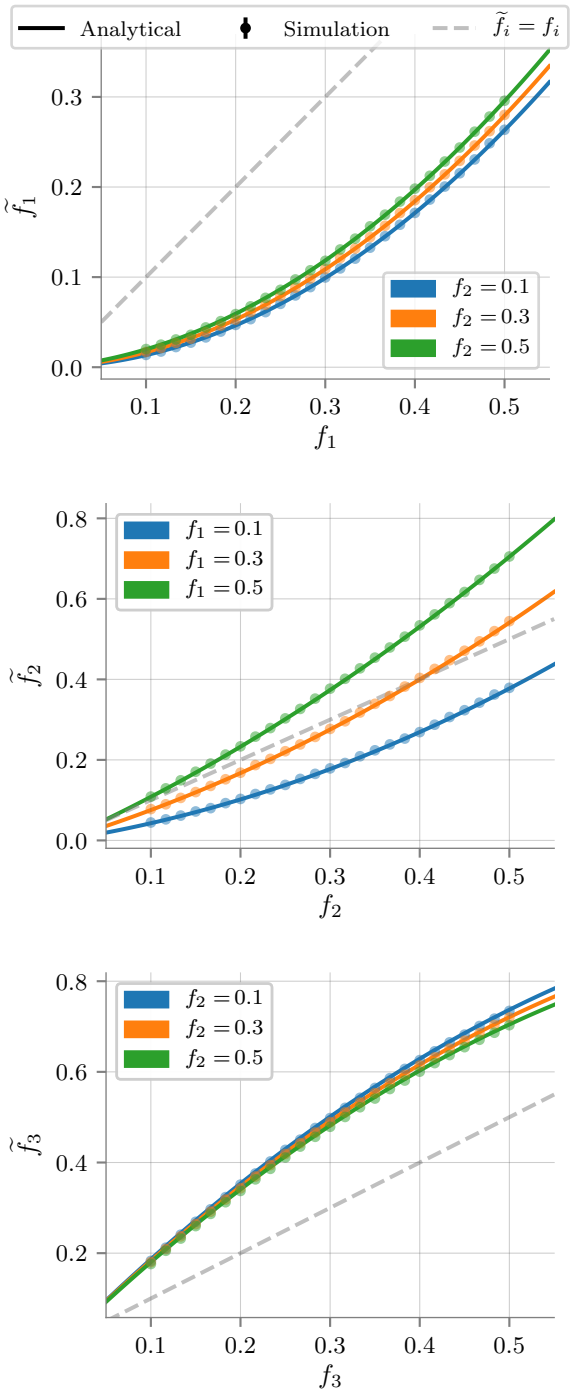

Fig. 8.18: Reconstructed fractional contribution $\widetilde{f}$ for an emission with a certain initial set of fractional contributions f_i, calculated analytically and with a simulation. In each plot, the values of only two components are shown, as $f_l = 1 - f_k - f_m$ always applies. The uncertainties of the simulation results are smaller than the marker size. The technique is discussed in the text.

It is noted that by describing one of the contributions with the other two $f_l = 1 - f_k - f_m$, it can be easily proved that the condition $\sum_i \widetilde{f}_i = 1$ is valid.

In figure 8.18 the reconstructed fractional contribution $\widetilde{f}_1$ and $\widetilde{f}_3$ for lifetimes $\tau_1 = 100\,\text{ns}$, $\tau_2 = 1\,\mu\text{s}$ and $\tau_3 = 10\,\mu\text{s}$ and for different initial f_i is shown. Since the photons from the component 1 are emitted faster, the probability that the second photon stems from 2 or 3 is higher and therefore $\widetilde{f}_1$ is always smaller than f_1. Conversely, the emission from component 3 is slow compared to the other two and thus the probability for the second photon originating from 3 is high. Hence $\widetilde{f}_3$ is always larger than f_3. The measured fractional component of 2 results in an intermediate case, being an underestimation of f_2 if more photons are being emitted from 2 than from 1, and overestimated if it is not the case. Given an experiment, where the emission is characterised by the assumptions of this example, i.e. triple exponential decay and only two detections per decay, its results (three $\widetilde{f}$ values) can be corrected by solving the equation 8.4 for the three f values.

The correction of the measurements done in this chapter is, however, somewhat more complex. The calculations until now have assumed that after one decay only two photons $N = 2$ are detected. This is the worst case scenario and the lowest number of photons with which such a lifetime measurement can be done. If the number of detections per decay increases, the error made is lower, as less information is lost. Nevertheless, the calculation of $\widetilde{f}_i$ for $N > 2$ is not trivial, as the number of permutations quickly increases with N and in the measurement with the samples up to $N \sim 50$ photons per decay are detected. Moreover, the measurement of the samples results in a distribution of the number of photons per decay $D_p(N)$, which complicates any attempt at correcting the measured lifetimes analytically.

Another possibility for estimating the error made in the measurement is to simulate the emission and detection with a Python code. One decay is simulated by sampling from the triple-exponential-decay of a certain f_i a number of times N following the measured $D_p(N)$. To the sampled times, the earliest one is subtracted. This is repeated several times in order to produce a histogram. Fitting this histogram returns the $\widetilde{f}_i$ values, which can be compared with the measurement. Throughout all this process, the lifetimes are being handled as constants. For the sake of consistency, this simulation was done with $\tau_1 = 100\,\text{ns}$, $\tau_2 = 1\,\mu\text{s}$ and $\tau_3 = 10\,\mu\text{s}$ and $D_p(N = 2) = 1$. The results are shown in figure 8.18 and exhibit no deviation to the analytical calculations.

Correction with the measured distributions

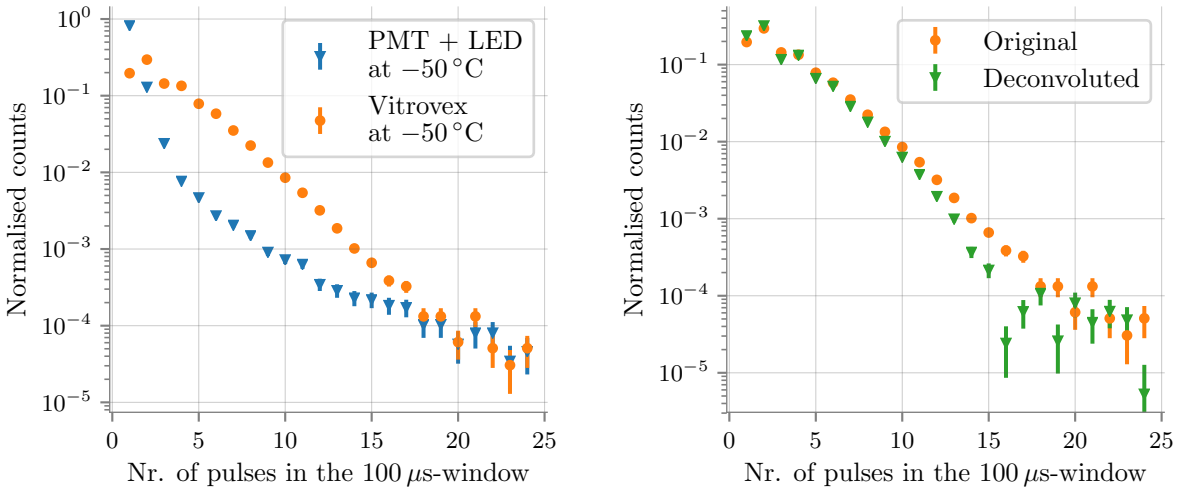

Fig. 8.19: Left: Distribution of the number of photon per waveform for the measurement with the LED and the excited Vitrovex glass sample at −50 °C. **Right:** Deconvolution of the Vitrovex distribution at −50 °C for removing effects of afterpulsing and background.

The measured distribution of the number of detections per decay is not the same as $D_p(N)$ needed for the correction, as it also includes afterpulsing events and the dark rate. In order to get rid of these influences, one can assume that the measured distribution is a convolution of $D_p(N)$ to the response to an SPE, which can be estimated using the measurement with the LED, as there the PMT is detecting almost exclusively SPE events. Both distributions are illustrated in the left plot of figure 8.19 for the measurement of the Vitrovex sample at −50 °C. This convolution implies that measuring two photons doubles the probability of measuring an afterpulsing and other correlated events, which is true. However, the distribution of the afterpulsing measurement also contains dark rates and thus, using it as a response function would also imply that the probability of a random event doubles after the detection of two photons as well, which is obviously false. Nevertheless, this should not be a big problem, as the probability of detecting a dark event inside the 100 μs window ($\sim 0.4\,\%$) is lower than the one of afterpulsing ($\sim 6\,\%$). In order to get $D_p(N)$ the measured distribution $D_m(N)$ has to be deconvoluted with the response function $D_{LED}(N)$:

$$D_p(N) = \mathcal{F}^{-1}\left(\frac{\mathcal{F}(D_m(N))}{\mathcal{F}(D_{LED}(N))}\right), \tag{8.5}$$

where $\mathcal{F}$ represents the Fourier transform and $\mathcal{F}^{-1}$ the inverse Fourier transform. Computationally, this calculation is done via a fast Fourier transform algorithm. The results of the measurement of the Vitrovex sample at $-50\,°C$ is shown in the right plot of figure 8.19. As expected, the mean number of photons detected after a decay decreases after the deconvolution, in this example from ~ 3.3 to ~ 3.0.

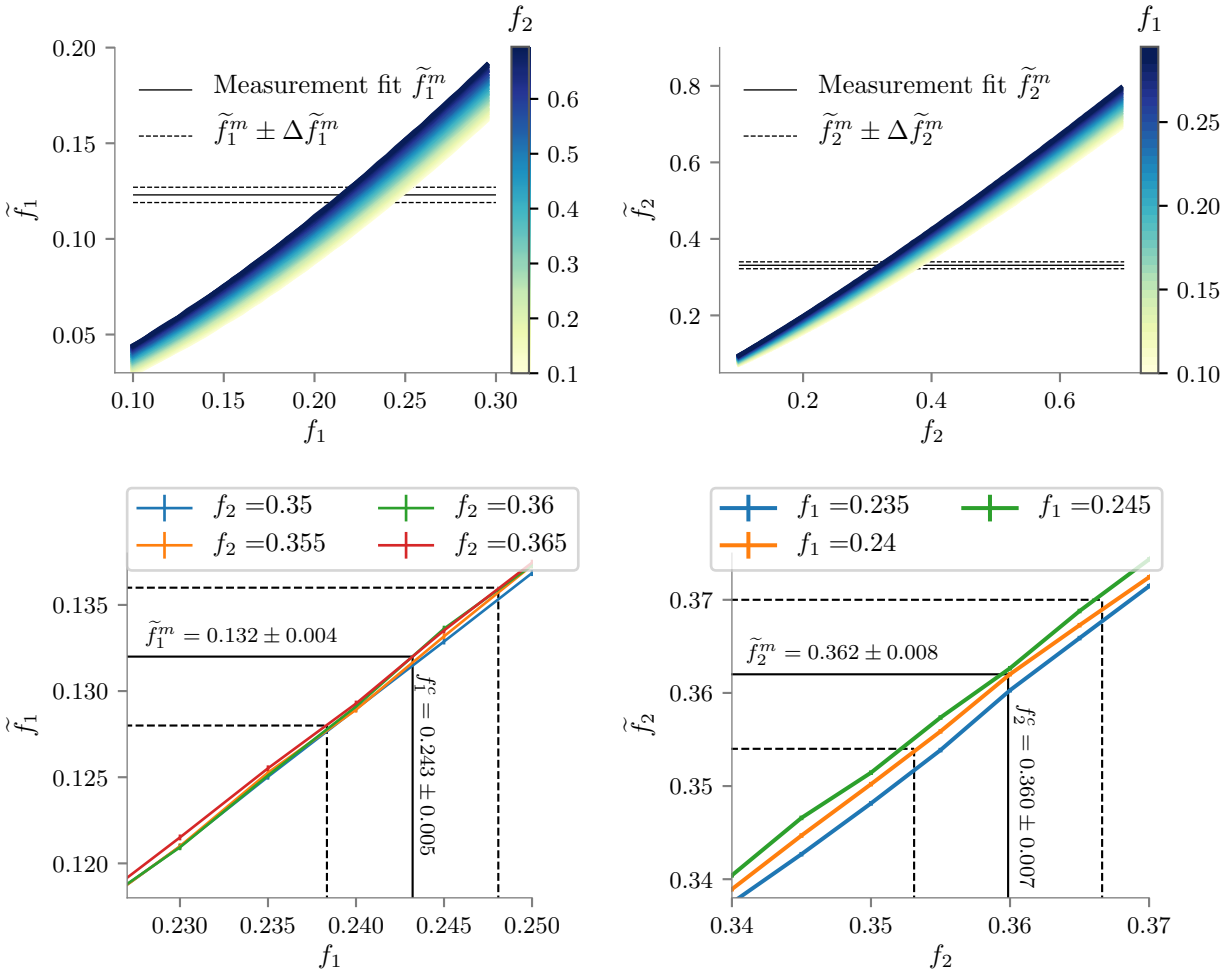

Fig. 8.20: Top: Fitted $\widetilde{f}_1$ (left) and $\widetilde{f}_2$ (right) for all simulated (f_1,f_2) pairs for the fit parameters of the Vitrovex sample at $-15\,°C$. **Bottom:** Interpolation procedure for calculating the corrected fractional contribution pair (f_1^c,f_2^c) given a measured pair $(\widetilde{f}_1^m,\widetilde{f}_2^m)$.

With the deconvoluted $D_p(N)$ it is then possible to simulate the emission as described in the last section. In the case of the glass samples, the emission was simulated for all combinations of fractional contributions in the intervals $f_1 = 0.1$ to $f_1 = 0.3$ and $f_2 = 0.1$ to $f_2 = 0.7$ in steps of 0.005. The third component is left parameterized as a combination of the other two $f_3 = 1 - f_1 - f_2$ and not explicitly varied[5]. The simulation results for the parameters obtained with the Vitrovex sample at $-15\,°C$ are presented in the top half of figure 8.20. Here, the fit values from the measurement are illustrated with a horizontal line. It is to notice, that there is a range of possible different initial conditions (f_1,f_2) that result in the fit value $\widetilde{f}_{1,2}^m$. This interval is limited, however, when both measurement results are taken into account at the same time. This is done, e.g. starting with $\widetilde{f}_1$ of the

[5]There is nothing special about f_1 and f_2. It would have been possible to vary any f pair.

left half, by only considering the f_2 lines that lie in the range crossed by $\widetilde{f}_2$ in the right plot. This reduces the band crossed by $\widetilde{f}_1$. Then, the same is applied to $\widetilde{f}_2$. This can be done several times, achieving a range of initial conditions, which is defined by the uncertainty of the fit values $\Delta\widetilde{f}^m_{1,2}$. The final corrected value of $\widetilde{f}^m_{1,2}$, is obtained by interpolating the two nearest curves. The same is done with the $\widetilde{f}^m_{1,2} \pm \Delta\widetilde{f}^m_{1,2}$ values, which results in a estimation of the uncertainty of the correction. This process is illustrated in the bottom half of figure 8.20. Table 8.2 shows the corrected values of the fractional contributions $f_{1,2}$ obtained with this procedure, together with the recalculated mean lifetime.

As expected, the fractional contribution with the shortest time constant is increased with the correction. This has a significant effect on the mean lifetime towards smaller values, which is also noticeable in the time distribution of the emission. Figure 8.21 shows a comparison between the fitted emission from the measurement of the Vitrovex sample at −15 °C with the corrected one. It is noteworthy, that the intensity of the earliest photons is up to 60 % larger, while the amplitude of the ones from the component with the longest lifetime is 20 % weaker.

Table 8.2: The corrected fractional contribution of the fit parameters shown in table 8.1 from the measurements with the Vitrovex and Benthos glass samples.

Vitrovex					
	−15 °C	−25 °C	−35 °C	−45 °C	−50 °C
f_1^c	0.243 ± 0.005	0.225 ± 0.006	0.216 ± 0.006	0.218 ± 0.006	0.226 ± 0.005
f_2^c	0.360 ± 0.007	0.357 ± 0.008	0.351 ± 0.008	0.340 ± 0.008	0.336 ± 0.008
$\overline{\tau}$ (μs)	8.77 ± 0.22	8.83 ± 0.23	9.69 ± 0.25	9.50 ± 0.25	11.40 ± 0.33
Benthos					
f_1^c	0.307 ± 0.009	0.301 ± 0.009	0.285 ± 0.008	0.281 ± 0.009	0.272 ± 0.008
f_2^c	0.305 ± 0.012	0.319 ± 0.012	0.312 ± 0.011	0.312 ± 0.012	0.310 ± 0.011
$\overline{\tau}$ (μs)	8.0 ± 0.4	8.7 ± 0.4	8.7 ± 0.4	8.1 ± 0.4	7.9 ± 0.3

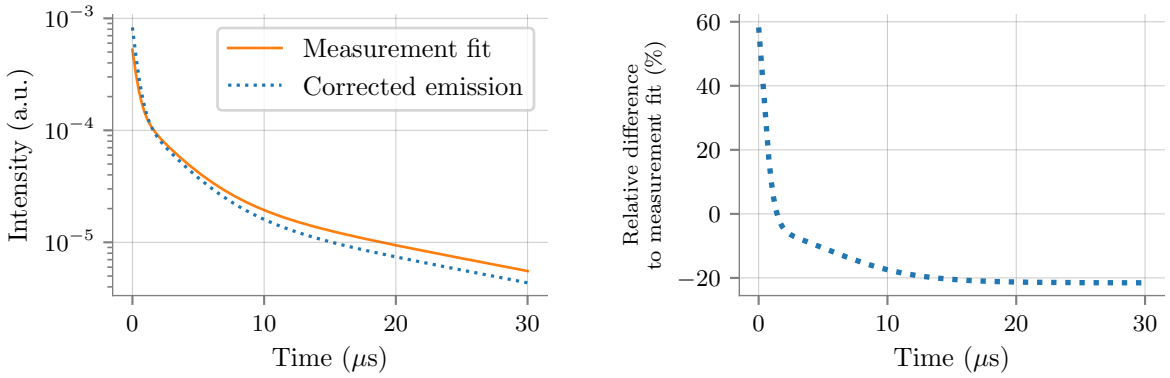

Fig. 8.21: Left: Comparison between the fit of the measurement of the emission of the Vitrovex sample at −15 °C and its correction. **Right:** Relative difference between the corrected and fitted emission. Here the constant factor of the fit was omitted, in order to do the comparison.

The same calculations are also done with the results of the gel samples. As aforementioned, in this case, the time constants are probably smaller, as they are of the same order of magnitude as the TTS of the PMT. One possibility to consider this in the correction is to include the transit time spread in the simulation. For this, to each value sampled from the emission is added a random number from a Gaussian with standard deviation equal to the TTS of the PMT $\sigma = (1.282 \pm 0.008)\,\mathrm{ns}$ (see section 7.1.3). The results for both samples with and without consideration of the TTS are summarised in table 8.3.

It is noticeable how much the time resolution of the PMT seems to affect the results of the QSI gel. As expected, both corrections, with and without consideration of the TTS, result in larger fractional contributions for the fastest time constant. However, the correction with TTS almost completely eliminates the contribution of the second time constant of $\sim 10\,\mathrm{ns}$, which implies that this is a product of the broadening of the fastest time constant. This is most noticeable comparing the time distributions, such as in the example shown in figure 8.22. Here, the parameters for the measurement at $-15\,°\mathrm{C}$ were used, and although this exhibits the largest f_2 among all temperatures, the corrected emission with TTS shows already only a double exponential decay similar to the one from the Wacker sample (see figure 8.16). Furthermore, the simulation including TTS produces a mean time constant $\sim 14\,\%$ smaller than the one without TTS, which demonstrates how much the time resolution of the PMT affects the measurement.

In the case of the results of the Wacker gel sample the effect of the TTS is much smaller, as the correction considering TTS reduces the average lifetime only $\sim 3.5\,\%$ more than the correction without TTS. This is to be expected, as the time constants of the results with the Wacker sample are larger than the ones with the QSI gel.

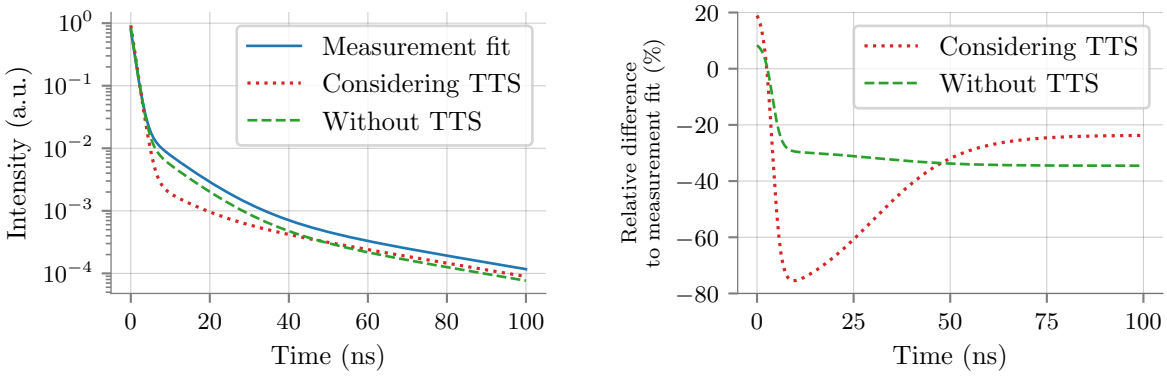

Fig. 8.22: Left: Comparison between the fit of the measurement of the emission of the QSI sample at $-15\,°\mathrm{C}$ and the corrections, simulating TTS and without it. **Right:** Relative difference between the corrected and fitted emissions. The constant factor of the fit was omitted.

Figure 8.23 shows the corrected mean lifetime $\overline{\tau}$ of the samples as a function of the temperature. All specimens exhibit a faster emission with higher temperatures, except for the Benthos glass. As seen in section 4.4, this is expected for a sample where thermal quenching is the most important nonradiative process that is temperature dependent, as the probability of surpassing the energy barrier that connects the excited and ground states is higher (see figure 4.3). This is not the case for the Benthos sample, where accounting the uncertainty the average lifetime remains fairly constant. This could imply that there are other non-negligible processes that are temperature dependent, or that the

energy barrier is large, and thus the temperature range used in the experiment is too small for noticing any change. Since the recombination efficiency should show a similar temperature dependence as the lifetime (see equation 4.8), more information about the involved processes can be further obtained in the next section, where the results for the scintillation yield are presented.

Table 8.3: The corrected fractional contribution of the fit parameters shown in table 8.1 from the measurements with the Wacker and QSI gel samples with and without consideration of the transit time spread of the PMT.

Wacker gel					
	−15 °C	−25 °C	−35 °C	−45 °C	−50 °C
f_1^c	0.858 ± 0.015	0.824 ± 0.014	0.821 ± 0.014	0.817 ± 0.013	0.812 ± 0.014
f_2^c	0.142 ± 0.015	0.176 ± 0.014	0.179 ± 0.014	0.183 ± 0.013	0.188 ± 0.014
$\overline{\tau}$ (ns)	27.8 ± 1.9	30.9 ± 1.7	31.8 ± 1.7	31.5 ± 1.5	32.2 ± 1.6
	Considering TTS				
f_1^c	0.867 ± 0.014	0.834 ± 0.013	0.831 ± 0.014	0.828 ± 0.013	0.823 ± 0.014
f_2^c	0.133 ± 0.014	0.166 ± 0.013	0.169 ± 0.014	0.172 ± 0.013	0.177 ± 0.014
$\overline{\tau}$ (ns)	26.8 ± 1.8	29.8 ± 1.6	30.7 ± 1.6	30.4 ± 1.5	31.1 ± 1.6
QSI gel					
f_1^c	0.834 ± 0.008	0.852 ± 0.010	0.859 ± 0.008	0.860 ± 0.008	0.855 ± 0.009
f_2^c	0.130 ± 0.008	0.097 ± 0.007	0.087 ± 0.006	0.077 ± 0.006	0.074 ± 0.006
$\overline{\tau}$ (ns)	3.4 ± 0.4	4.0 ± 0.4	4.6 ± 0.5	4.9 ± 0.5	5.1 ± 0.5
	Considering TTS				
f_1^c	0.929 ± 0.005	0.928 ± 0.006	0.931 ± 0.005	0.933 ± 0.005	0.930 ± 0.005
f_2^c	0.029 ± 0.006	0.014 ± 0.005	0.013 ± 0.004	0.004 ± 0.004	0.002 ± 0.004
$\overline{\tau}$ (ns)	2.9 ± 0.3	3.5 ± 0.3	4.0 ± 0.3	4.2 ± 0.3	4.3 ± 0.3

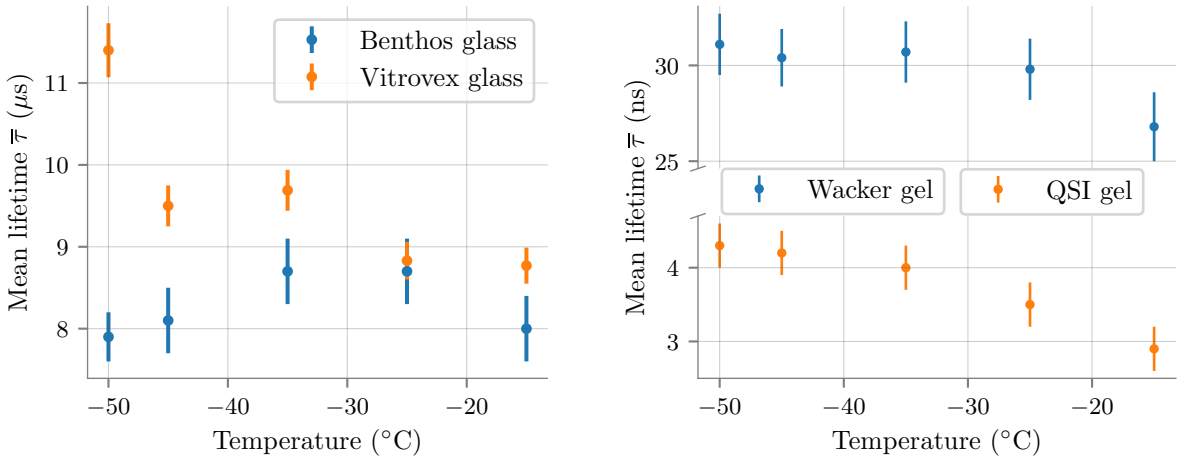

Fig. 8.23: Mean lifetime of the corrected emission of the four samples as a function of the temperature.

8.3 Scintillation Yield

In the previous two sections, the scintillation spectrum and lifetime of the investigated materials were determined. This section presents the calculation of the final parameter, the scintillation yield. The approach described in section 8.3.2 consisted of exciting the samples with an alpha source and measuring the PMT rate produced from the scintillation. The yield can be then determined if the geometry of the setup and the α-emission is well known. For this purpose, the activity of the source was measured with an alpha spectrometer in section 8.3.2. Key for the experiments of this section is to have a reliable method for measuring the PMT rate, as many factors of the setup may influence the measured value. The next part is dedicated to this topic.

8.3.1 Measuring PMT rates

In order to measure the rates of the PMT an oscilloscope *PicoScope 6404C* is used. This can be operated in *rapid block mode*, where an adjustable number of waveforms (or captions) are measured and then sent to the computer. The number of sampling points in each caption can be set to one so that the dead time between two waveforms is only determined by the duration of the rearming of the trigger. This whole process is controlled by a Python code, which also calculates the time t_N needed for the oscilloscope for measuring N captures. The requested number of waveforms is automatically adjusted to the mean rate, ensuring comparable statistics and time coverage - having a constant number of captions could result in very few data points, if the PMT rate is low, or too many when it is high. This would be especially problematic for measurements in the climate chamber, as the temperature can change relatively quickly. Hence, in order to have a steady measurement rate, the number of captions is set so that t_N lies between 2 to 3 s.

It stands to reason that the rates are given with $N \cdot t_\mathrm{N}^{-1}$, however t_N has to be corrected, as it is determined by the Python code and not the oscilloscope, meaning that in this time the processing and data transfer time from the oscilloscope to the PC alters the real PMT rate. This correction is calculated in the next subsection. Nevertheless, still after this, the calculated rate is constrained by other parameters and deviates from the real number of detections of the PMT. One obvious variable is the low amplitude single photoelectron pulses due to the trigger level, as already explained in section 7.1.2. Another parameter is the dead time between captures, which will severely reduce the measured rate, as it is in the same order of magnitude as the decay time constant of the scintillation.

Rate correction

For estimating the error of the rate measurement described above and its correction, a pulse generator[6] was connected to the oscilloscope producing rectangular pulses with a width of 16 ns and random frequencies between 0 and 10 kHz. The accuracy of this generator is high, with a relative uncertainty of ± 1 ppm of the set frequency value [61]. These pulses were measured with the same code used for the PMT rate measurement, meaning that the number of captions is set in such a way, that the measurement time

[6] RIGOL model DG1032Z

per data point is 2 s to 3 s. Figure 8.24 shows the results of this measurement. As expected the measured rates are smaller than the set frequency, especially at higher rates. This can be partially explained by an increase in processing time of the oscilloscope with the number of captions or longer delay for the data delivering to the computer.

The measurement shows an almost linear relationship, nevertheless it was fitted with polynomials of different numbers of degrees. The best result was achieved with a fifth-degree polynomial

$$f(x) = \sum_{i=0}^{5} a_i \cdot x^i, \tag{8.6}$$

with the coefficients a_i

$$a_0 = (-0.08 \pm 0.50)\,\mathrm{s}^{-1}, \qquad a_1 = 1.0026 \pm 0.0010,$$
$$a_2 = (7.3 \pm 0.7) \cdot 10^{-6}\,\mathrm{s}, \qquad a_3 = (-0.8 \pm 1.7) \cdot 10^{-10}\,\mathrm{s}^2,$$
$$a_4 = (-1.8 \pm 2.1) \cdot 10^{-14}\,\mathrm{s}^3, \qquad a_5 = (-8.1 \pm 8.8) \cdot 10^{-19}\,\mathrm{s}^4.$$

Correcting the rates with this function produces a maximal relative error of about 0.3 %, as seen in the residuals of the fit in figure 8.24.

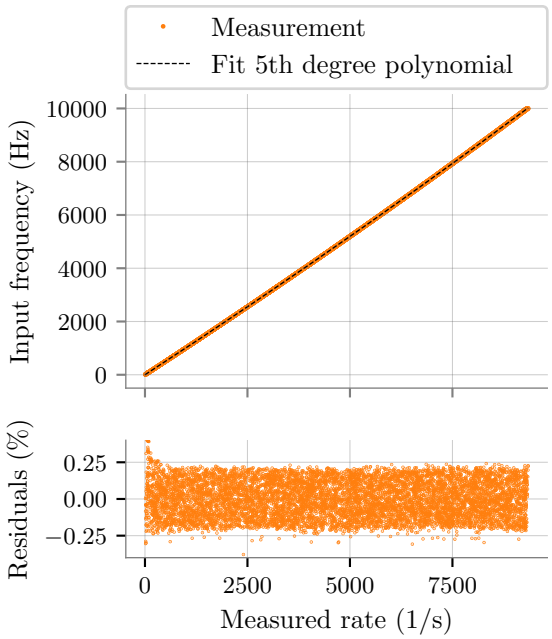

Fig. 8.24: Measured rate by the oscilloscope for different input frequencies generated by the pulse generator. The data is fitted with a fifth-degree polynomial, yielding relative residuals of less than 0.3 %.

Dead time between captures

To determine the dead time between captures a sine wave with frequency f_{in} was generated with the pulse generator and sampled in rapid block mode, as in the configuration of the rate measurement, but without a set trigger. Each capture takes one value of the sine amplitude, which gets digitised at 8 bit by the oscilloscope. The amplitude of the signal is set in such a way, that the whole range of the oscilloscope is used, for maximising the achieved resolution.

As the oscilloscope is measuring without a trigger, the signal is being sampled at the maximal sampling rate, where the sampling period is determined by the dead time between the captures. Thus, by fitting the data with a sine function, the number of captures N needed for the measurement of one period of the sine wave P_{in} can be calculated, and thus also the sampling period

$$P_{\mathrm{s}} = \frac{P_{\mathrm{in}}}{N} = \frac{f_{\mathrm{fit}}}{f_{\mathrm{in}}},$$

where the f_{fit} is the obtained frequency from the fit. This is done with a different number of captures, in order to investigate any dependency of the measurement configuration on the dead time. These results are depicted on the left side of figure 8.25, showing no distinctive dependency between the mean dead times measured with various number of captures, with deviations of less than 0.05 %. The mean sampling period is (1063.701 ± 0.023) ns.

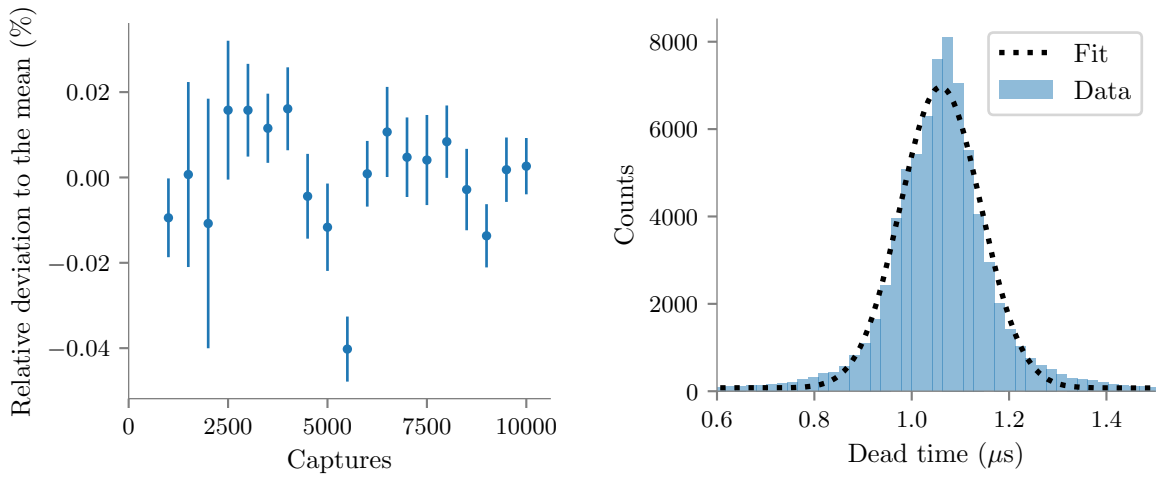

Fig. 8.25: Left: Comparison between the mean dead time retrieved with different number of captures. **Right:** The distribution of dead time between captures. It can be approximated as a Gaussian function.

Although the mean dead time can be retrieved with a very high accuracy, this also varies between captures. As the fit curve always marks the position of the mean, the standard deviation of the sampling period can be estimated by calculating the distance between the data points to the fit curve along the x-axis. This yields the distribution shown in the right part of figure 8.25, which can be fitted with a Gaussian with the standard deviation of $\sigma_1 = (82.68 \pm 0.28)\,\text{ns}$. However, this distribution gets widened by the y-resolution originating from the digitisation of the oscilloscope. As introduced, the data is digitised in 8 bit, therefore the amplitude can get assigned integer values between -128 to 128. This means, there is an uncertainty of 0.5 for every y-value, which also affects the x-residuals. Therefore the real variance of the dead time will be $\sigma_\text{R}^2 = \sigma_1^2 - \sigma_\text{y-res.}^2$, where $\sigma_\text{y-res.}$ is the x-residual widening stemming from the y uncertainty. The latter is estimated by artificially doubling the uncertainty of the y-values, increasing them randomly from a flat distribution of length 1. The resulting x-residual distribution has a standard deviation of $\sigma_2 = \sqrt{\sigma_\text{R}^2 + 2 \cdot \sigma_\text{y-res.}^2} = (83.75 \pm 0.28)\,\text{ns}$ and therefore the standard deviation of the dead time is $\sigma_\text{R} = \sqrt{2 \cdot \sigma_1^2 - \sigma_2^2} = (81.6 \pm 0.6)\,\text{ns}$.

8.3.2 Yield determination by external excitation

In this section, the yield is calculated exciting the samples with an ^{241}Am α-source. The experimental setup used for this is the same as the one of the lifetime measurement shown in figure 8.14. The activity and an estimation of the isotope distribution on the source surface are calculated in the following subsection, as these parameters are needed for the yield estimation. Aside from this, the air scintillation yield is calculated, since there is a small gap between the samples and the source, which contaminates the results.

Activity of the alpha source

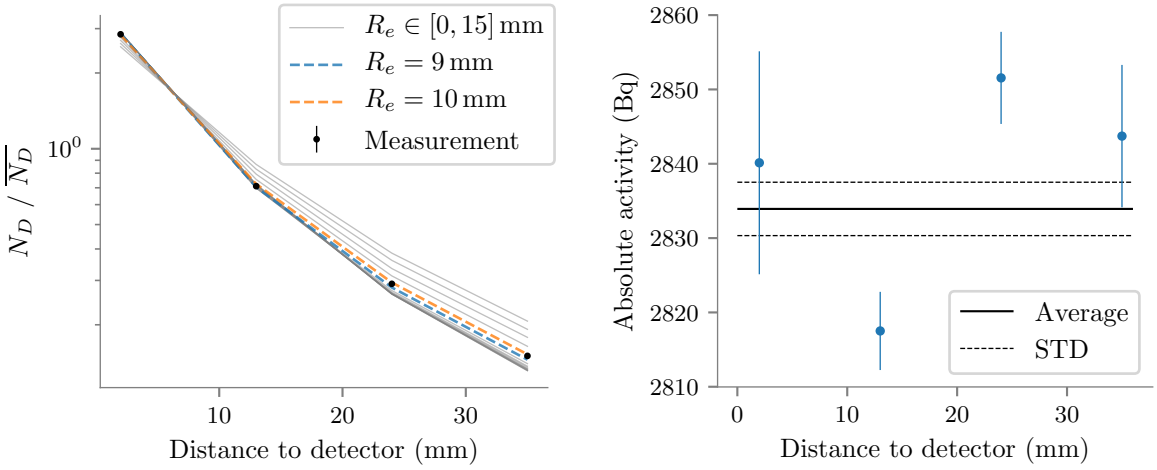

Fig. 8.26: Left: Comparison between simulation (lines) and the measurement results (points) of the relative efficiency variation at different source-detector distances for an assumed circular emission of radii $R_e \in [0, 15]$ mm. The values of the measurement are located consistently between the results for $R_e = 9$ mm and $R_e = 10$ mm. The uncertainties are smaller than the point markers. The simulation values are only valid at the distances where the measurements were done and are represented as lines for reasons of clarity. **Right:** Activity resulting from the measurement done at different distances. The mean and standard deviation (STD) of these points are also given with lines.

For the determination of the absolute activity of the source, an alpha spectrometer is used. The principle of an alpha spectrometer is very similar to the gamma spectroscopy explained in section 6.1. In this case, the source is placed right in front of a semiconductor detector inside a vacuum chamber (pressure $< 10^{-7}$ Bar), to avoid energy loss from alpha particle interaction with air molecules. After being processed by a combination of a pre- and a main amplifier, the semiconductors signal is digitised by a multichannel analyser. This way, an energy spectrum of the emission is obtained. In the scope of this work, only the activity of the source is needed, thus only the integration of the spectrum is necessary (total number of counts). The activity of the source A_s can be calculated via

$$A_s = \frac{1}{4\pi}\Omega \cdot \frac{N_D^{\mathrm{m}}}{t} = \varepsilon \cdot \frac{N_D^{\mathrm{m}}}{t}, \tag{8.7}$$

where Ω is the solid angle covered by the detector, ε the absolute detection efficiency, N_D^{m} the number of detections and t the duration of the measurement. The solid angle is only defined by a point source emission, otherwise ε should be used.

The calculation of the absolute detection efficiency is not trivial, as the distribution of the ^{241}Am isotopes on the surface of the source is not known. To estimate this distribution, one can measure the relative change of ε when the source is placed at different distances to the detector, and compare this to simulation results of a certain distribution. In the setup, (2.0 ± 0.2) mm is the nearest the source and the semiconductor can be placed. To increase the distance, up to three holders each with a width (11.0 ± 0.1) mm are used.

The source emission is assumed to be circular with radius R_e and with a constant surface density. A radius of $R_e = 0$ mm would correspond to the case of a point source

in the middle of the source. For this, a Geant4 code is used, where the setup geometry is reproduced and the fraction of detected particles N_D^{s} from a total of 10^6 is obtained. This is simulated for emissions with radii between 0 mm and 15 mm in 1 mm steps and source-to-detector distance as in the experimental setup. To compare the simulation results to each other and the measurement, the number of detections at each distance N_D^{s} is divided by the mean $\overline{N_D^{\mathrm{s}}}$ between the four distances. For the measurement results, the mean count rate $(N_D^{\mathrm{m}} \cdot t^{-1})$ is used instead of the total counts, as the duration of the measurements varies. The results are presented in the left plot of figure 8.26. It can be seen, that the measurement results lie between the values of the simulation with radii 9 mm and 10 mm at the four distances. Interpolating the $N_D^{\mathrm{s}}/\overline{N_D^{\mathrm{s}}}$ values with the measurement points, one obtains an effective emission radius of $R_{\mathrm{eff}} = (9.62 \pm 0.11)$ mm. Although most probably the density and shape of the isotope distribution on the source's surface are very complex, these results connote that it can be effectively described as a circular distribution of constant surface density.

Simulating again with the calculated emission radius, the absolute detection efficiency $\varepsilon = N_D^{\mathrm{s}} \cdot 10^{-6}$ is obtained for each distance and the activity is calculated with equation 8.7. The results can be seen on the right side of figure 8.26. The mean activity between the four distances is (2834 ± 4) Bq. The uncertainty of this value is only the statistical part originated from the error of the integration of the measured spectra and the efficiency calculated from the simulation ($\sqrt{N_D}$ in both cases). For determining the uncertainty stemming from Δd and ΔR_{eff}, the efficiency is simulated again but with distances $d \pm \Delta d$ and radii $R_{\mathrm{eff}} \pm \Delta R_{\mathrm{eff}}$. The average activity between the four distances is calculated with these efficiencies, and the maximal deviation arising from ΔR_{eff} and Δd are 16 Bq and 79 Bq respectively. Thus the absolute activity of the source is $A_s = (2834 \pm 81)$ Bq.

Air scintillation yield

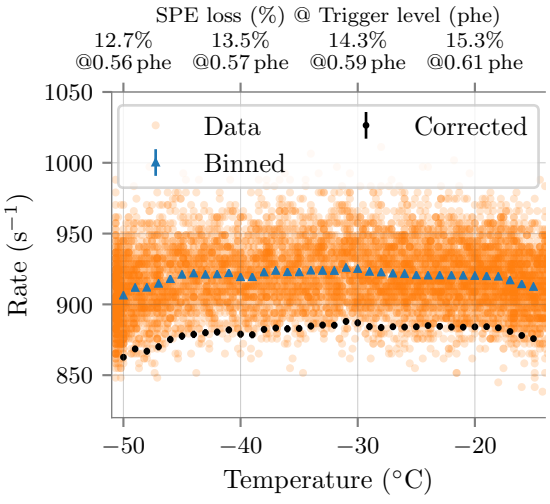

Fig. 8.27: Measured rate from the scintillation of the air. The raw data is binned in 1 °C steps for the sake of clarity. Also illustrated is the corrected rate after subtraction of the PMT dark rate. The second x-axis shows the percentage of SPE loss due to the set threshold of −18 mV and the trigger equivalent in phe (see section 7.1.2).

In order to measure the scintillation yield of the air, the source is placed (5.90 ± 0.05) cm directly in front of the PMT. At this distance, alphas cannot reach the PMT and are completely absorbed in the air. The climate chamber is first cooled to −50 °C, then switched off and from then on the PMT rates are saved as the chamber slowly warms up to room temperature. The results are shown in figure 8.27. As the rate is measured every 2 to 3 s, there is a lot of data points for each temperature. For better handling and clarity this data is binned in 1 °C steps.

The measured rate contains also the intrinsic background from the PMT and has to be corrected. Hence, the dark rate of the PMT is measured (only the PMT is inside the dark box) three times, obtaining the results shown in the left side of figure 8.28. For the sake of clarity, only the binned data

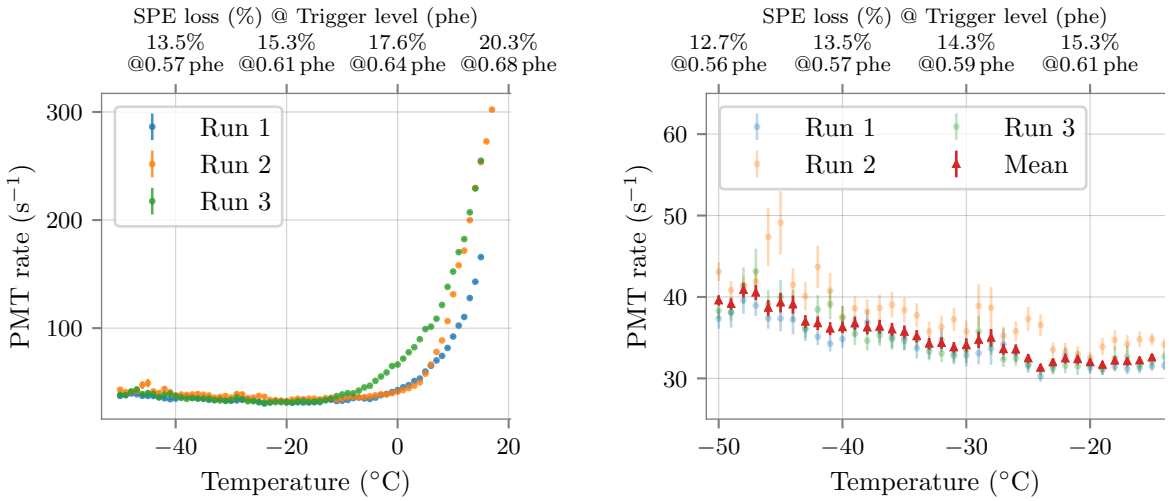

Fig. 8.28: Three measurements of the PMT dark rate as a function of the temperature. The second x-axis shows the percentage of SPE loss due to the set threshold of $-18\,\mathrm{mV}$ and the trigger equivalent in phe (see section 7.1.2). **Left:** For the whole temperature range of the measurement, **right:** only in the region of interest $-50\,°\mathrm{C}$ to $-15\,°\mathrm{C}$ with the mean rate between the three runs.

is presented. The three measurement exhibit similar results in the interval corresponding to the IceCube operating temperature range from $-50\,°\mathrm{C}$ to $\sim -10\,°\mathrm{C}$, but then the increase from the thermionic effect start at different temperatures and its slope also differs. The reason for this behaviour was not clear at the time of writing. For the further calculations, the average rate in the temperature interval from $-50\,°\mathrm{C}$ to $-15\,°\mathrm{C}$ in $1\,°\mathrm{C}$ steps will be used. This is illustrated in the right plot of figure 8.28.

Furthermore, it is important to determine the influence of the gamma rays emitted by the ^{241}Am-source on the measured rate, as these photons could release photoelectrons at the photocathode or dynodes. To this end, the radioactive source was placed inside a black plastic cup in front of the PMT, in order to shield the PMT from the air luminescence. The rate increase compared to the dark rate is illustrated in figure 8.29. There is no striking temperature dependency, which is expected because of the constant decay rate of the source. The average rate increase is of $(4.2 \pm 0.2)\,\mathrm{s}^{-1}$. However, this is just slightly larger than the variation between the measurements of the PMT dark rate (see figure 8.28 right) and thus, this increase could be mostly caused from the deviation of the PMT dark rate. For the further measurements with the source, the rate will be corrected by $(4 \pm 2)\,\mathrm{s}^{-1}$. Nevertheless, the influence of the gammas is almost

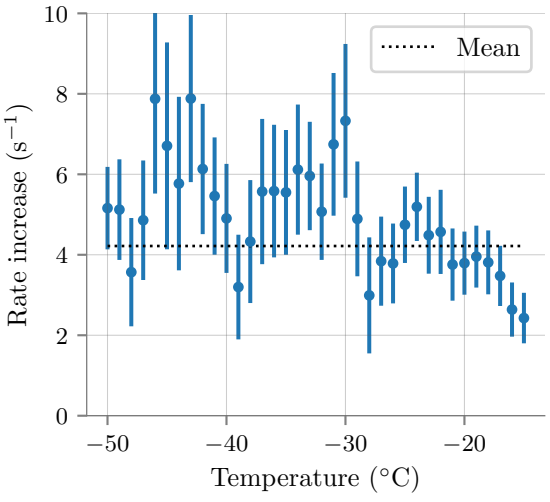

Fig. 8.29: PMT rate increase from the mean dark rate due to gamma-rays emitted from the radioactive source.

neglectable, as the rate from the samples and air scintillation is in the order of $\mathcal{O}(10^2)$-$\mathcal{O}(10^3)$.

The corrected rate of the air scintillation is illustrated in figure 8.27. With this, it is possible to calculate the yield using the Geant4 simulation. Here only the PMT and the source are simulated with the same distance between each other as in the measurement. The air scintillation spectrum used is the one measured in [58] shown in figure 8.5. The photon detection is done as described in chapter 5, using the dead time between captures calculated previously. In one simulation event, an alpha is emitted from the source with an isotropic direction. The scintillation photons are separated into two categories depending on their amplitude, if two or more photons were detected within a time that cannot be resolved by the PMT, it counts as a "definitive" hit H_D. If this is not the case, e.g. only one photon is detected, there is a possibility that it does not go through the threshold of the PMT and is saved as a "possible" hit H_P. After 2000000 events, the mean $\overline{H_P}(y)$ and $\overline{H_D}(y)$ per decay for the air scintillation yield y is obtained. Simulating with several y, it is possible to calculate the expected rate $R(y,T)$ in dependence on the yield y and temperature T:

$$R(y,T) = \left(\overline{H_D}(y) + \overline{H_P}(y) \cdot \big(1 - P(T)\big)\right) \cdot A_s, \tag{8.8}$$

where $A_s = (2834 \pm 81)\,\mathrm{Bq}$ is the activity of the α-source, and $P(T)$ the probability of an SPE for not being detected due to the trigger level of $-18\,\mathrm{mV}$, calculated in section 7.1.2. The air scintillation yield is then calculated by interpolation of the simulation data with the measured rate R_m. This is done with two different scintillation lifetimes. According to [62], the decay time constant of the air scintillation at atmospheric pressure is 0.5 ns, however, this value can vary between 1.9 ns and 0.4 ns, depending on the air composition and pressure. These are values well below the time resolution of the PMT, and it should make just a little difference, as most of the time all photons are detected as a single pulse. Nevertheless, the simulation was done with $\tau_{\mathrm{air}} = 0.5\,\mathrm{ns}$ and $\tau_{\mathrm{air}} = 2\,\mathrm{ns}$, the latter as a conservative value for the estimation of the uncertainty. The results are shown in figure 8.30. As expected, the case with $\tau_{\mathrm{air}} = 2\,\mathrm{ns}$ results in a slightly larger yield ($\sim 0.8\,\%$) than the case with $\tau_{\mathrm{air}} = 0.5\,\mathrm{ns}$, as more hits are SPE and therefore categorised into the $\overline{H_P}(y)$ part instead of $\overline{H_D}(y)$. The difference between these two distributions is used as the error stemming from the lifetime. The final result for the yield and its uncertainty is presented in the right part of figure 8.31. Most of the uncertainty is systematical, thereby including the error from the source activity ΔA_s, the uncertainty of the distance between the PMT and the source and the error from the lifetime just calculated. In the statistical error, the uncertainty from $\Delta P(T)$, ΔR_m and the simulation parameters $\Delta\overline{H_{D,P}}$ are considered.

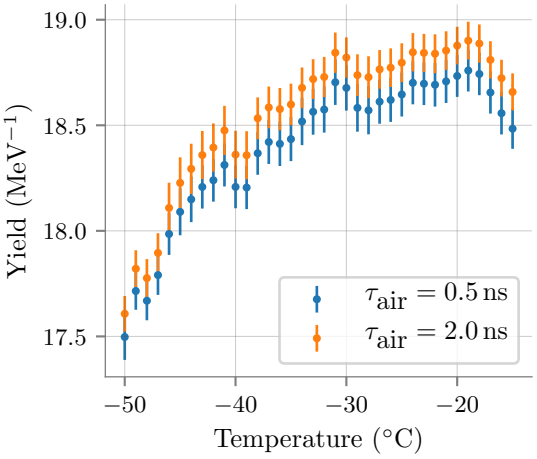

Fig. 8.30: Calculated air scintillation yield for alpha particles with two different lifetimes $\tau_{\mathrm{air}} = 0.5\,\mathrm{ns}$ and $\tau_{\mathrm{air}} = 2\,\mathrm{ns}$. Error bars include only the statistical uncertainty (see text).

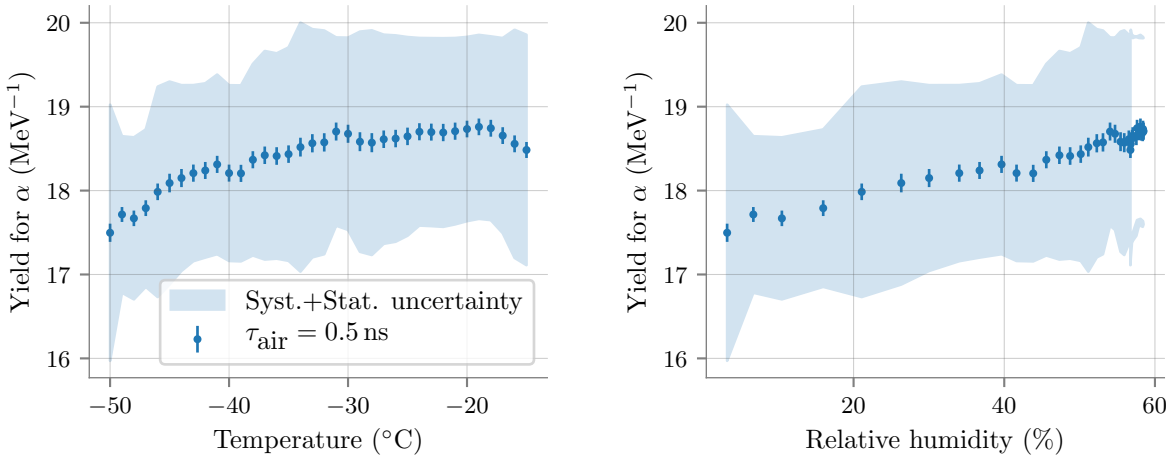

Fig. 8.31: Calculated yield illustrated in dependency of the temperature (left) and of the relative humidity (right). The blue region represents the total uncertainty (systematical and statistical error, see text).

It is noteworthy, that the air scintillation yield seems to increase with the temperature between −50 °C and −30 °C and then remains fairly constant as the temperature increases. The average yield in the temperature range from −30 °C to −15 °C is $(18.7 \pm 1.2)\,\mathrm{MeV}^{-1}$. This agrees with the results from other studies that were done at room temperature - $(19 \pm 3)\,\mathrm{MeV}^{-1}$ in [63] and $(18.9 \pm 2.5)\,\mathrm{MeV}^{-1}$ in [64]. Quantitative studies on air scintillation yield with alpha particles are rather rare, and no values in dependency of the temperature could be found in the literature. It is known, however, that there is a dependency on the air composition, and therefore also on the number of water molecules [63]. Hence, the decrease at lower temperatures seen in figure 8.31 is most probably an effect of the change of the humidity with the temperature rather than from the temperature itself. On the right side of figure 8.31 the same data points are illustrated, but in dependency of the measured relative humidity from the sensor on the base of the PMT. Here, the results show a fairly linear behaviour, which supports the premise. Nevertheless, for the sake of simplicity at further calculations, the air yield in dependency of the temperature will be taken, as the relative humidity does not change much between different measurements. Furthermore, the uncertainty of the yield is larger than the differences seen between different temperatures or humidities and therefore any shift between measurements is considered in the error.

Measurement with the mDOM material samples

The rate measured with the samples being excited with the α-source is illustrated in figure 8.32. All specimens exhibit a linear increase of the rates with lower temperatures, except for the Wacker gel, which features a shift at ~ -35 °C. According to the manufacturer, this gel crystalises between −45 °C and −50 °C into a white harder state. Therefore, this shift is probably caused either by a higher optical absorption or larger scattering probability inside the sample. As the rate measurement is done while the chamber is warming up, the deviation happening 10 °C away from expected may indicate a hysteresis effect in the decrystallisation process. Nevertheless, it is noteworthy that the rate decreases linearly

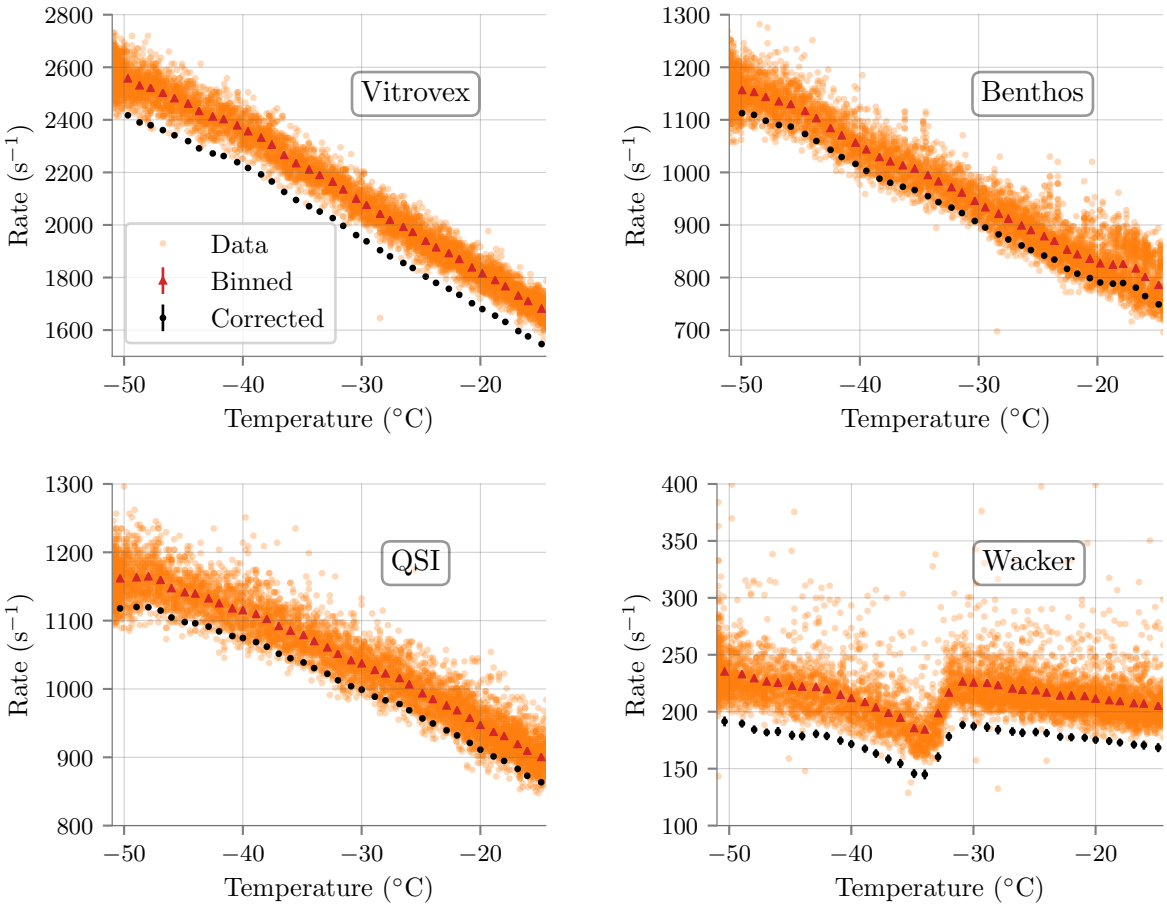

Fig. 8.32: Measured rate from the scintillation of the glass (Vitrovex and Benthos) and gel samples (QSI and Wacker). The raw data is binned in 1 °C steps. Also illustrated is the corrected rate after subtraction of the PMT dark rate. In this case, the percentage of SPE loss and the trigger equivalent in phe were not depicted in a second x-axis for sake of clarity (cf. figure 8.28 and 8.27).

with the temperature before and after the deviation, which may imply that the emission of the sample exhibits a similar behaviour as the one of the other materials.

For each setup, the influence of air scintillation was simulated, in order to correct the measurement. This will vary, depending on the geometry of the setup (gap of air between the sample and the radioactive source, distance to PMT, etc.) and the transmission of the specimen being examined. The simulated geometries of the glass and gel samples are shown in figure 8.34. While the glass samples were directly positioned in front of the PMT with the holding clamp, the gel samples were cured inside the holding cylinder of the source. In order to protect the source against the gel, a ring with width (0.6 ± 0.1) mm was positioned in-between these two. The results of the air rate simulation are shown in figure 8.33. As the gap between the gel specimens and the source is small, a fairly low rate is measured from the air luminescence. In the case of the glass samples, this gap was wider ((1.0 ± 0.1) mm), which results in a higher rate. The setup with the largest contamination is the one of the Vitrovex glass, as this is the biggest sample (side length of ~ 3 cm compared to ~ 1 cm of the Benthos specimens), the PMT covers a larger solid angle.

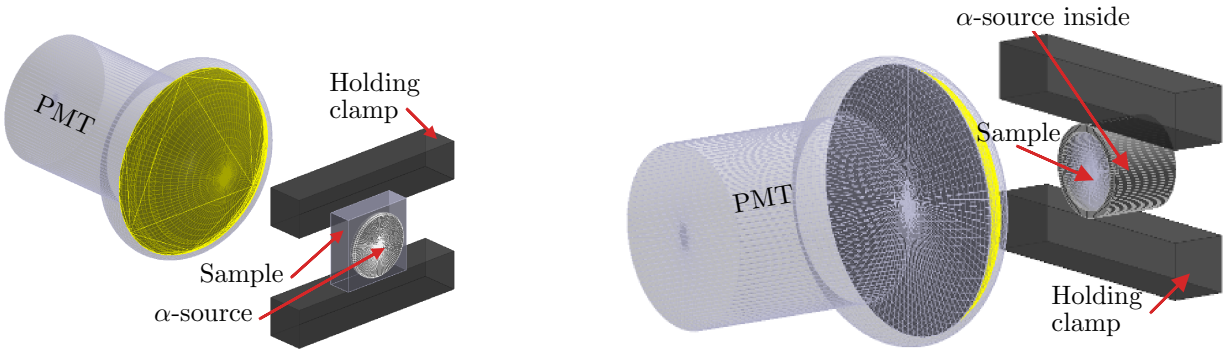

Fig. 8.34: Simulated geometry of the experimental setup shown in figure 8.14. **Left:** for the glass samples; in the picture, it has the dimensions of the Vitrovex specimen. **Right:** for the gel samples.

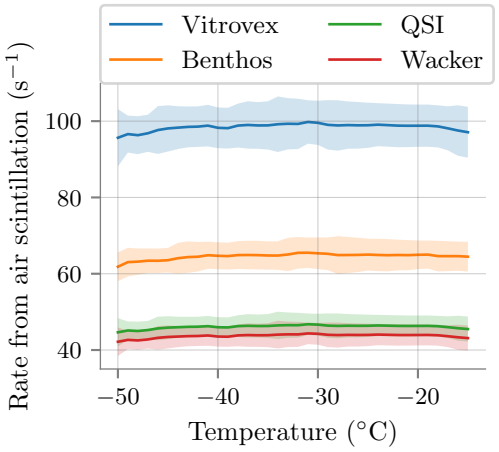

Fig. 8.33: Simulated rate caused by air scintillation in the experimental setup for the different samples. The desaturated band around the lines represents the systematical and statistical error.

The calculation of the yield is quite similar as it was done with the air luminescence. Here, however, one also has to take into account the variation of the lifetime with the temperature. Thus, the simulation is done with the five lifetimes values measured in section 8.2, obtaining an expected number of detections per decay that definitely surpassed the trigger level $\overline{H_D}(y)$, and the ones that have to be corrected for the detection loss $\overline{H_P}(y)$. As these lifetimes correspond to the temperatures $T_n = [-50, -45, -35, -25, -15]°C$, the simulation results can be ordered to a more general $\overline{H_D}(y, T_n)$ and $\overline{H_P}(y, T_n)$. With this it is possible to make an interpolation ℓ for every temperature between T_i and T_{i+1}, following

$$\ell_{D,P}(y, T) = \overline{H_{D,P}}(y, T_i) + \big(T - T_i\big) \cdot \frac{\overline{H_{D,P}}(y, T_{i+1}) - \overline{H_{D,P}}(y, T_i)}{T_{i+1} - T_i}. \tag{8.9}$$

Hence, the expected rate measured at the temperature T with an emission of yield y is calculated as in equation 8.8:

$$R(y, T) = \Big(\ell_D(y, T) + \ell_P(y) \cdot \big(1 - P(T)\big)\Big) \cdot A_s, \tag{8.10}$$

where $A_s = (2834 \pm 81)\,\mathrm{Bq}$ is the activity of the source, and $P(T)$ the probability of a SPE for not being detected due to the trigger level. Comparing this expected rate with the measured one, it is possible to calculate the emission yield of the samples. These results are presented in figure 8.35.

The yield for the Wacker gel was not simulated since there is no information about the spectrum, which is needed for the simulation. As mentioned in section 8.1.2, this material probably emits mostly in the UV region, where the PMT is not sensitive. Hence, the measured rate corresponds probably to a small fraction of the whole spectrum.

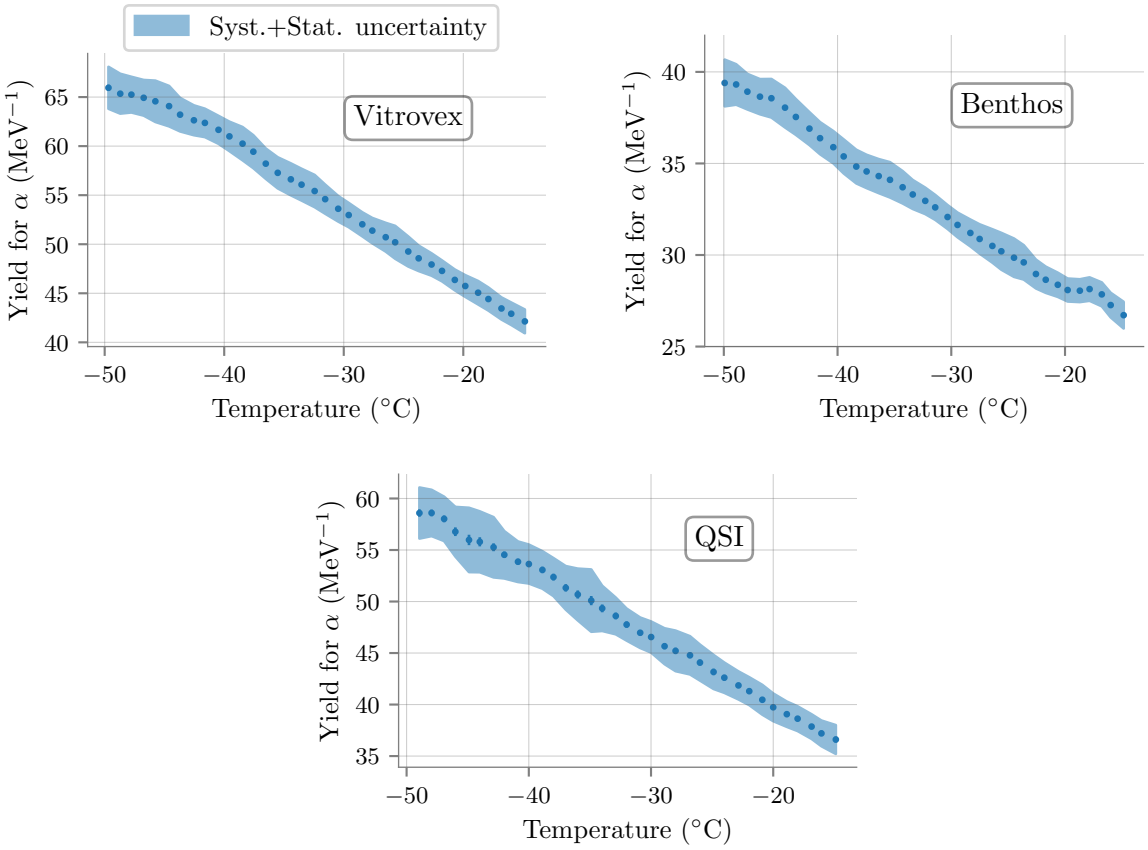

Fig. 8.35: Calculated yield for alpha particles in photons emitted per absorbed MeV for both glass samples and the QSI gel as a function of the temperature.

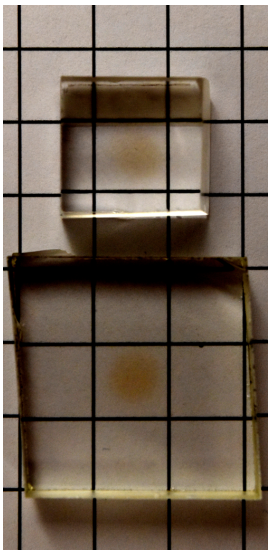

Fig. 8.36: Darkening of the transmission of the sample at the location where the source was placed indicating radiation damage. The contrast of the image was strongly increased for better discernability. Gridpoint distance 1 cm.

In the case of the other three samples, between −15 °C and −50 °C the yield increases ∼ 57 % (from $(42.1 \pm 1.2)\,\mathrm{MeV}^{-1}$ to $(65.9 \pm 2.2)\,\mathrm{MeV}^{-1}$) for the Vitrovex, ∼ 48 % (from $(26.7 \pm 0.8)\,\mathrm{MeV}^{-1}$ to $(39.4 \pm 1.3)\,\mathrm{MeV}^{-1}$) for the Benthos and ∼ 60 % (from $(36.6 \pm 1.4)\,\mathrm{MeV}^{-1}$ to $(58.6 \pm 2.5)\,\mathrm{MeV}^{-1}$) for the QSI specimen. This is expected for the Vitrovex and QSI samples, as this is also the behaviour shown by their average lifetimes (see figure 8.23). In the model considered in section 4.4, the recombination efficiency is directly proportional to the lifetime, as $\eta = \tau \cdot \tau_\mathrm{r}^{-1}$, where τ_r is the time constant of the radiative transition, which is normally treated not to be temperature dependent. However, for the Benthos glass, the average lifetime remained fairly constant at different temperatures, which contradicts the measurement of its yield in figure 8.35. This may imply an error during the measurement of the time constant. With only five measurement points for the lifetime temperature dependence, it is difficult to spot any incongruity in the data. Nevertheless, the points between −35 °C and −15 °C

show a decreasing behaviour, which could suggest an error in the measurement of the values at −50 °C and −45 °C. Another possibility could be a more complex underlying process, which is not considered in the model.

Furthermore, the calculated yield contains some errors, as the scintillation spectrum was only measured at room temperature and this changes with the temperature since the transitions occur at different energy levels due to the influence of phonons (see section 4.2). It is difficult to estimate this deviation, as also the absorption of the material will change. Nevertheless, these results can be taken as an effective yield, that is valid for PMTs with similar QE, and thus this should not be a big problem for the studies on dark rates, as the same PMT model was used for this measurements as the one planned for the mDOM.

A noteworthy effect observed after the measurements were disk-shaped darkening spots on the glass samples (see figure 8.36), which could not be cleaned with solvents like water, ethanol, isopropanol or acetone. It is a known fact that radiation damage can cause a reduction of the optical transmission of inorganic semiconductors, although most literature refers to accelerator physics, where the energy of the incident particles is orders of magnitude higher [65]. The rate measurement was done right after the one of the lifetime, and thus the samples were continuously irradiated with the α-source at least four days, and even longer as some measurement had to be repeated. Thus, it is not known the time span needed for this radiation damage to take effect. Moreover, it is difficult to determine if and how much this effect may have influenced the yield measurement, as although the transmission change is not very dramatic (the contrast of figure 8.36 was highly enhanced), the darkening implies a change in the electronic states configuration in the region where the absorption and emission occurs [65].

9 Simulation of dark rates in optical modules

In the previous chapters, the amount of isotopes inside the glass and gel samples was determined and the light produced by the radioactive decays was characterised. With this information, the background produced by the vessel glass and the gel inside the optical modules can be simulated. In this context, the following sections will describe the expected noise separating it between correlated and uncorrelated background, thus presenting its time distribution. Furthermore, as measured in chapter 8 the scintillation properties are highly temperature dependent and the expected background will also be introduced as a function of the temperature.

The time distribution of the noise is usually presented in a $\log_{10}(\Delta t)$ diagram. As this kind of plots may not be a common way of displaying data, section 9.1 gives a small introduction on the interpretation of correlated and uncorrelated noise in the $\log_{10}(\Delta t)$ representation.

Section 9.2 and 9.3 present some simulation studies for the DOM and mDOM, respectively. Although the motivation of this work is to estimate the background from scintillation for the mDOM, it is also important to study the case of the current IceCube DOM, since for the latter there is experimental data available. Hereby it is possible to estimate, how precise the prediction for the mDOM is.

9.1 Introduction to $\log_{10}(\Delta t)$ diagrams

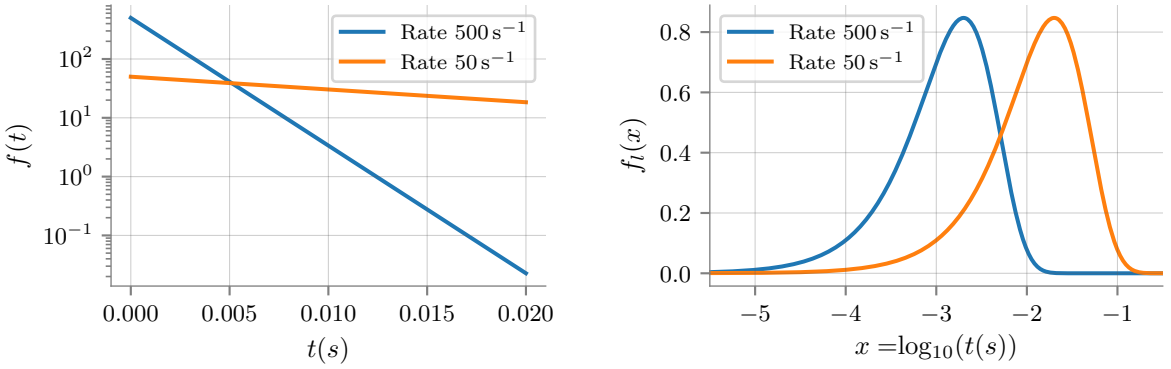

Fig. 9.1: The probability density function of the waiting time t for a background event stemming from random noise of rate 50 s^{-1} and 500 s^{-1}. **Left:** with linear and **right:** with a logarithmic representation of the time.

Random noise of average rate μ (hits per second) is a Poissonian process since the probability for an event is independent of the past. Let D be the waiting time for the detection

of a hit. The probability that D is larger than a given time t is

$$P(D > t) = \frac{(\mu \cdot t)^0 e^{(-\mu \cdot t)}}{0!} = \exp(-\mu \cdot t). \tag{9.1}$$

Hence, the cumulative density function (CDF) $F(t)$ is given by

$$F(t) = P(D \leq t) = 1 - \exp(-\mu \cdot t) \tag{9.2}$$

and its probability density function (PDF) $f(t)$ by the derivative of the CDF

$$f(t) = \frac{d}{dt} F(t) = \mu \cdot \exp(-\mu \cdot t). \tag{9.3}$$

Therefore, the time difference between subsequent hits from random background is expected to produce an exponential decay with a slope equal to the average rate of the noise (assuming a logarithmic scale in the ordinate). As an example, the Δt distribution for random background of rate $50\,\mathrm{s}^{-1}$ and $500\,\mathrm{s}^{-1}$ is shown in the left part of figure 9.1. However, this is only valid for a linear application of the abscissa. If the time is represented by its logarithm (applying the substitution $t = 10^x$), the CDF of the distribution in 9.1 is equal to $F_l(x) = 1 - \exp(-\mu \cdot 10^x)$ and thus the PDF is given by

$$f_l(x) = \frac{d}{dx} F_l(x) = \mu \cdot 10^x \cdot \log(10) \cdot \exp(-\mu \cdot 10^x). \tag{9.4}$$

For comparison, the random background of $50\,\mathrm{s}^{-1}$ and $500\,\mathrm{s}^{-1}$ is given in this representation in the right part of figure 9.1. Although the PDF for the logarithm of the time is more complex, it has some advantages over the linear representation, e.g. the maximum of equation 9.4 lies at $x = -\log_{10}(\mu)$, and thus the rate can be more easily visualised than in the linear case. Moreover, the benefits of a $\log_{10}(\Delta t)$ representation manifest itself in background that combines both, correlated and uncorrelated signals, like the case of a PMT or the optical modules, as these processes can be better differentiated.

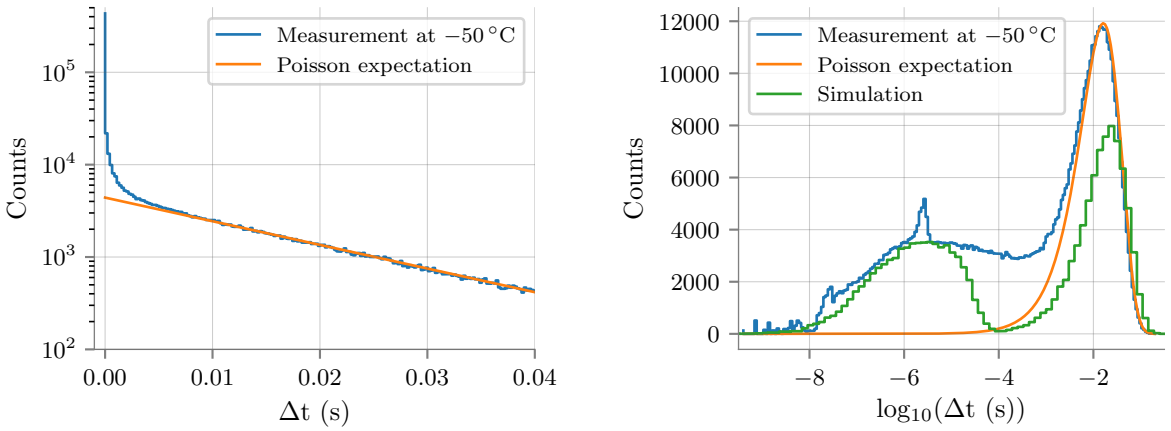

Fig. 9.2: Measured time between subsequent signals Δt of a PMT inside a Benthos half vessel at −50 °C. Also shown with a yellow line is the fit of the Poisson expectation for the uncorrelated part of the background. **Left:** histogram of the Δt distribution. **Right:** histogram of the logarithm of the Δt data. Here, also the simulated distribution stemming from scintillation is shown with a green line.

In order to give an example of correlated and uncorrelated background, the time of subsequent hits from a PMT inside the Benthos half pressure vessel was measured. The signal of the PMT is split with a T-adapter and sent to two different oscilloscopes[1]. One of them saved the time difference of pulses inside waveforms of 100 μs and the second oscilloscope the Δt between triggers, which has a lower boundary as the rearming of the trigger takes around $\sim 1\,\mu$s. Combining the data from both devices into a histogram yields the results shown in figure 9.2(left). Since there is correlated noise originating from the PMT (afterpulsing) and the vessel (coincident hits from scintillation of radioactive decays), the Δt distribution deviates from the Poissonian one showing a larger number of counts for very short time differences. Taking the logarithm of the data and graphing it as a histogram yields the results shown in the right part of figure 9.2. In this case, the correlated background can be better distinguished from the Poissonian expectation and the process causing the different structures can be deduced. In section 8.2, the most probable time delay for late afterpulsing of the PMT was found to be at around 3 μs, while for the early afterpulsing at < 50 ns (see figure 8.15). These times correspond to the peaks seen at $\sim -5.5\log_{10}(\mathrm{s})$ and $\sim -7.6\log_{10}(\mathrm{s})$ in figure 9.2 (right).

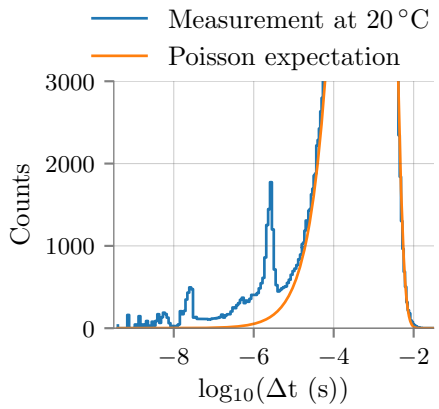

Fig. 9.3: Measured time between subsequent signals of a PMT inside a Benthos half vessel at 20 °C.

The expected Δt distribution from luminescence for this setup was simulated with Geant4[2] using the scintillation parameters measured in chapter 8 and the mass-specific activity of the isotopes inside the half vessel measured in chapter 6. The result is also presented in figure 9.2. Here the amplitude of the simulated histogram was modified in order to fit the measured curve. It is noticeable that luminescence accounts for most of the correlated background under $-5\log_{10}(\mathrm{s})$, but that it also contributes to the uncorrelated peak. This part stems from the time differences between photons from different decays, which is random and determined by the activities of the isotopes. The sum of several Poissonian processes with a rate λ_i results in a single Poisson distribution of rate $\sum_i \lambda_i$, and thus only one Peak from the uncorrelated background is measured. Furthermore, the simulated distribution does not account for the correlated noise measured at longer time differences at around $-4\log_{10}(\mathrm{s})$.

For comparison figure 9.3 shows the same measurement done at 20 °C. Here, the effects of the luminescence background are almost unnoticeable, as the yield decreases with higher temperatures (see section 8.3.2), leaving only the dark rate from the PMT. As the thermionic noise from the PMT is much higher at this temperature, the Poissonian peak shifts towards shorter times. However, it is to notice that the correlated background measured between $\sim -4.7\log_{10}(\mathrm{s})$ and $\sim -3\log_{10}(\mathrm{s})$ in figure 9.2, which cannot be explained by luminescence parametrised with the result from chapter 8, also does not appear in the measurement. This suggests that this background must be also caused by scintillation, which would mean that there are one or more extra time constant in the order of ms. The exponential decays from lifetimes in this order of magnitude would be seen as a constant

[1] A PicoScope 6404C and a Lecroy Waverunner 640ZI
[2] The next section 9.2 explains how these distributions are simulated.

and could not have been extracted from the waveforms of 100 μs used in the measurements of section 8.2.

Altogether, $\log_{10}(\Delta t)$ diagrams are a helpful resource for analysing correlated and uncorrelated noise. In this context, in the next two sections the contribution of the scintillation light to the overall background of the modules will be simulated and discussed in more detail.

9.2 Current IceCube DOM

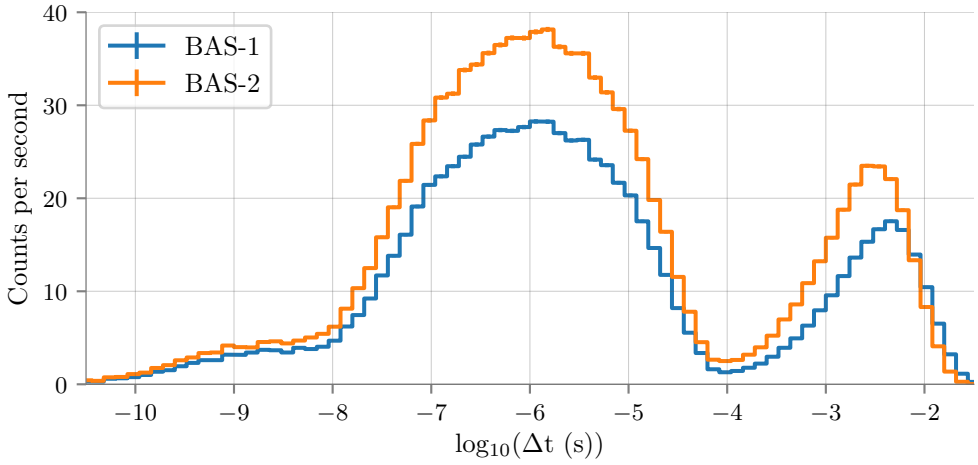

Fig. 9.4: Simulated time between subsequent hits in $\log_{10}(\Delta t)$ for a DOM in ice at −35 °C. Both measured sets of isotope activities BAS-1 (table 6.2) and BAS-2 (table 6.3) were used. The error bars only consider the statistical uncertainty and are smaller than width of the line.

The time distribution of the background and its total rate depends on the amount of radioactivity in the glass. There were two sets of isotope activities measured for the Benthos glass in chapter 6, which will produce different results. For the sake of simplicity, the set of activities for the Benthos samples summarised in table 6.2 and 6.3 will be referenced as "BAS-1" and "BAS-2" respectively.

In order to simulate the time distributions of the background caused by radioactive decays in the DOM surrounded by ice, the decay of the natural series and the ^{40}K are simulated 100000 times. Here, the scintillation parameters at −35 °C were used and only luminescence of the glass was taken into consideration. The effects of gel luminescence are studied later in section 9.4. Since only the scintillation yield for α-particles was determined, it is assumed that electrons exhibit a yield 9.5 times larger, following the results for another kind of glass [41 (p. 255)]. An output file is created for each isotope, where one line of the file contains the hit time of the detected photons from a single decay. If in an event no photon was detected, the line is left empty. Thus, each file contains 100000 lines. Hereby, the time distribution of the noise can be constructed by mixing the decay results with a Python code. The number of decays of a specific isotope during one second is sampled randomly from a Poisson distribution with a mean equal

to the isotope activity (assuming a pressure vessel of 9.07 kg[3]). These decays are ordered randomly in time and for each, one line from the isotope's file is sampled, containing the hit times of the detected photons. This is done consecutively 600 times with all isotopes, resulting in a time array corresponding to 10 minutes of background. The resulting Δt distribution is presented in figure 9.4 for BAS-1 and BAS-2.

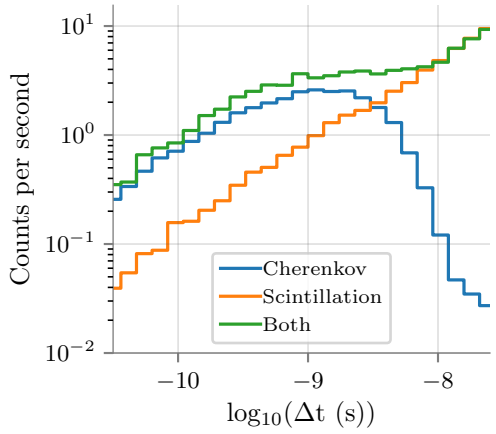

Fig. 9.5: Time between subsequent hits considering only Cherenkov photons (blue line), only scintillation (yellow line) and both (green line). The statistical uncertainty is not depicted, as it is smaller than the line width.

Since in BAS-2 the activity of the ^{238}U chain is $\sim$ 42 % larger, the expected background for this set is higher and the maximum of the Poissonian peak lies also at shorter time intervals. Figure 9.5 shows the fastest hits in the interval -10 to $-8\log_{10}(\mathrm{s})$, which correspond to time differences between 0.1 ns and 10 ns. Here are depicted the results of the simulation of BAS-1 separating the Cherenkov and scintillation photons. It can be seen that the principal source of hits in this region originate from Cherenkov light and that the contribution of the luminescence noise decreases exponentially with shorter times. However, it has to be noticed that in the simulation either TTS nor the PMT pulse length was taken into account, and therefore most of this time differences cannot be measured. The pulse length (FWHM) of the PMT used inside DOMs (Hamamatsu R7081-02) is about 7.5 ns [66], and hence Δt shorter than $-8\log_{10}(\mathrm{s})$ will be strongly suppressed, as is the case in the measurements shown in figures 9.2 and 9.3.

In order to compare the shapes of the time distribution curve from both isotope activity sets, these were normalised in the left side of figure 9.6. Here are also shown the results for the case of a vessel with 50 % and 150 % of the isotope activities from BAS-1. The peak from luminescence does not change with a variation of the amount of radioactivity and only the position of the Poissonian part moves towards higher or lower rates. This is to be expected, as the scintillation peak is produced by photons from the same decay and therefore its shape is independent of the radioactive decay rate. On the right side of figure 9.6 is shown the normalised distribution for three different scintillation yield values. The results shown in figure 9.5 are for the scintillation parameters at $-35\,^{\circ}\mathrm{C}$, viz. a yield of $34\,\mathrm{MeV}^{-1}$. Comparing the results for this yield value with a lower of $20\,\mathrm{MeV}^{-1}$ and a larger one of $50\,\mathrm{MeV}^{-1}$ it can be noticed that the relative height of the luminescence peak in regards to the Poissonian part changes. With an increase of the yield, the number of hits from a single decay is larger, while only the first and last detected photon from the decays contribute to the uncorrelated part, reducing its relative contribution to the overall distribution. A similar reasoning can be applied for the region of the distribution stemming from the Cherenkov radiation, since this is independent of the yield. Although the rate of Cherenkov photons detected is the same, the Cherenkov part of the distribution has a larger relative contribution to the distribution if the yield

[3]Teledyne Benthos, 2013. Deep Sea Glass Spheres. Available online at: `http://www.teledynemarine.com/Lists/Downloads/Flotation_Spheres_Data_Sheet_2013_lo.pdf` (Last accessed 18 December 2017).

is smaller. Furthermore, it is noteworthy that the shape of the scintillation part also changes with the yield, having fewer counts at shorter Δt. This may be a similar effect as the one encounter in the measurements of the lifetime (see section 8.2). The first photon detected from a decay does not contribute to the correlated part of the distribution, but to the Poissonian peak. Therefore the number of detected Δt corresponding to the shortest lifetime is lower than the emitted one. This effect is further enhanced when the number of photons per decay decreases.

In IceCube the time distribution of the background can be studied separately for each DOM with the HitSpool data[4]. This data is however limited to the dead time of the DOM mainboard, with a minimum time between triggers of 2.45 μs depending on the readout sequence [68]. This precludes the study of most of the correlated noise. Nevertheless, a glimpse of this region was provided in [67], where the HitSpool distribution was combined with FRT[5] data. This data set does not have enough statistics in order to construct a time distribution of the background for each DOM and thus the information of every module was combined in a single histogram. The results obtained with this approach are shown in figure 9.7. Here roughly the same features can be found as in the measurement shown in 9.2, including an afterpulsing peak at around $\sim -5.1\log_{10}(\mathrm{s})$ (as the R7081-02 PMT is larger than the Hamamatsu R12199-02, it takes longer for the ions to reach the photocathode).

It is noteworthy that the Gaussian fitted to the correlated noise in figure 9.7 is very similar to the results shown in figure 9.4. Excluding the Cherenkov contribution at very short time differences, the simulated distribution exhibits a maximum at around $-6\log_{10}(\mathrm{s})$ and decreasing quite symmetrically until about $-8\log_{10}(\mathrm{s})$ and $-4\log_{10}(\mathrm{s})$. Nevertheless, the distribution in figure 9.7 also features a long timescale correlated peak centred at $-4\log_{10}(\mathrm{s})$, which is not explained by the scintillation parameters measured in this thesis. This was seen also in the results of the measurement done with the Benthos

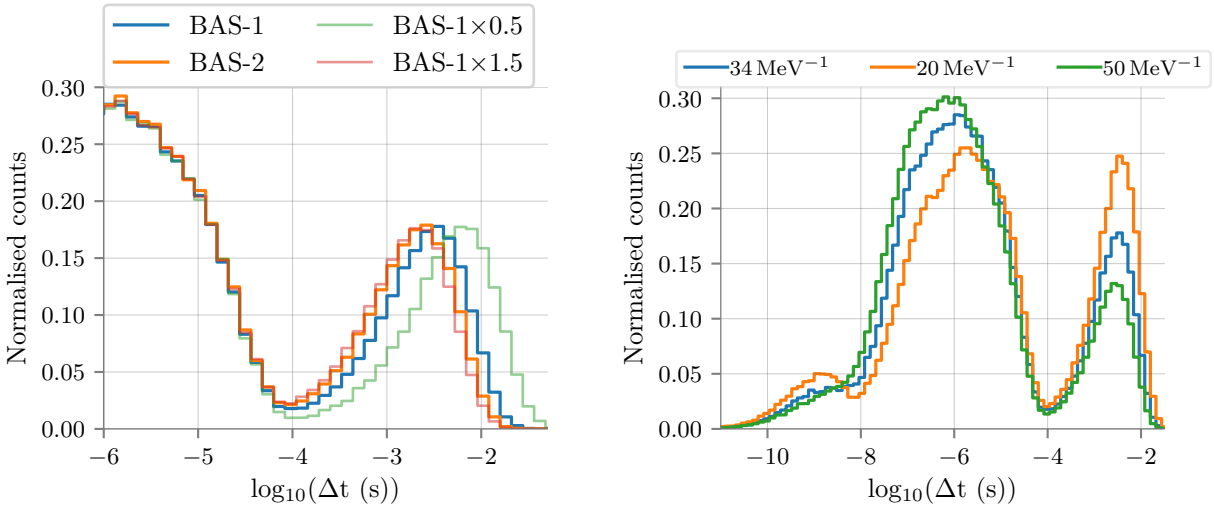

Fig. 9.6: Relative change of the background time distribution by varying the isotope activity in the glass (**left**) and the scintillation yield (**right**). The statistical uncertainty is not depicted, as it is smaller than the line width.

[4]HitSpooling is a standard DAQ feature that buffers the raw data stream of the modules around supernova candidate triggers. Further information can be found in [68].

[5]At Fixed Rate Trigger (FRT) events, 10 ms of raw data is saved every 30 s for every DOM.

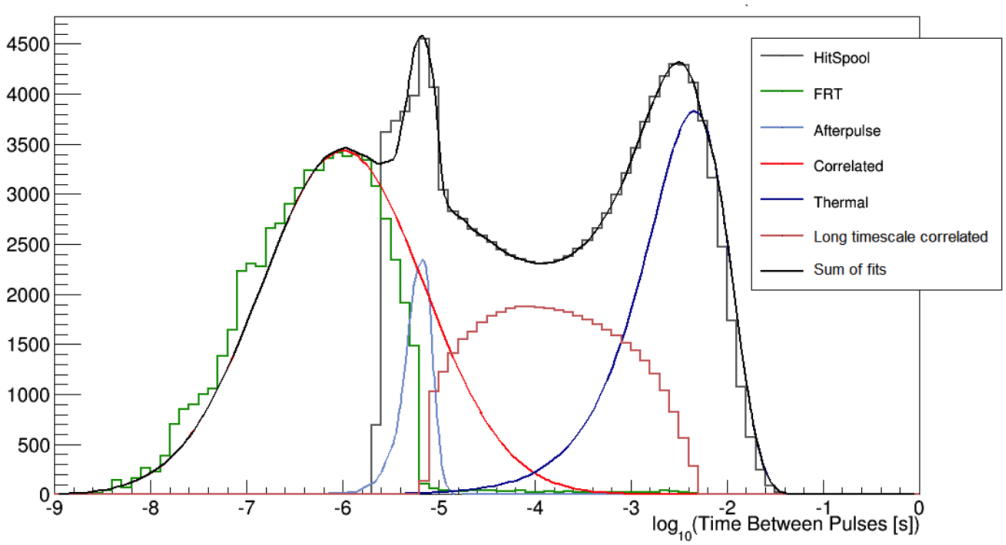

Fig. 9.7: Time distribution of the DOM background in IceCube. In order to make this histogram, the HitSpool and FRT data of all modules were combined. Figure taken from [67].

half vessel in last section (see figure 9.2) and probably stems from long-lived luminescence transitions.

With the Geant4 simulation, it is also possible to calculate the temperature-dependence of the background rate cause by radioactive decays in the pressure vessel. First, the decay of the three decay chains and ^{40}K is simulated 2×10^6 times each, once for every scintillation parameters at $T_i = [-15, -25, -35, -45, -50]\,°\text{C}$. As the results of these calculations are to be compared with the HitSpool data, in the simulation is set a dead time of $2.45\,\mu\text{s}$ between hits. Also, the PMT waveform and QE are considered, as explained in chapter 5. The output of the simulation provides the average number of photons detected $H(T_i, I)$ for the temperature T and isotope I. Thus, the rate R at T_i is calculated with

$$R(T_i) = \sum_I H(T_i, I) \times A_I \times m, \tag{9.5}$$

where A_I is the mass-specific activity of the isotope I and $m = 9.07\,\text{kg}$ is the mass of the pressure vessel. As the scintillation yield $y(T)$ was determined for all temperatures between $-50\,°\text{C}$ and $-15\,°\text{C}$ in $1\,°\text{C}$ steps, the rate can be calculated at these same temperatures by linear interpolation. Therefore, the rate $R(T)$ at the temperature T, when $T_i > T > T_{i-1}$, is given by

$$R(T) = R(T_{i-1}) + (y(T) - y(T_{i-1})) \times \frac{R(T_i) - R(T_{i-1})}{y(T_i) - y(T_{i-1})}. \tag{9.6}$$

This rate can be furthermore separated between correlated and uncorrelated noise by constructing the Δt distribution for every T_i and fitting the Poissonian peak with equation 9.4. The percentage of uncorrelated noise can be then calculated by integrating this fit and dividing it by the total number of counts of the distribution. The results of this approach are shown in figure 9.8. Here is also depicted the rate from the HitSpool data, where each point represents the average rate of 12 DOM layers from 78 strings [18].

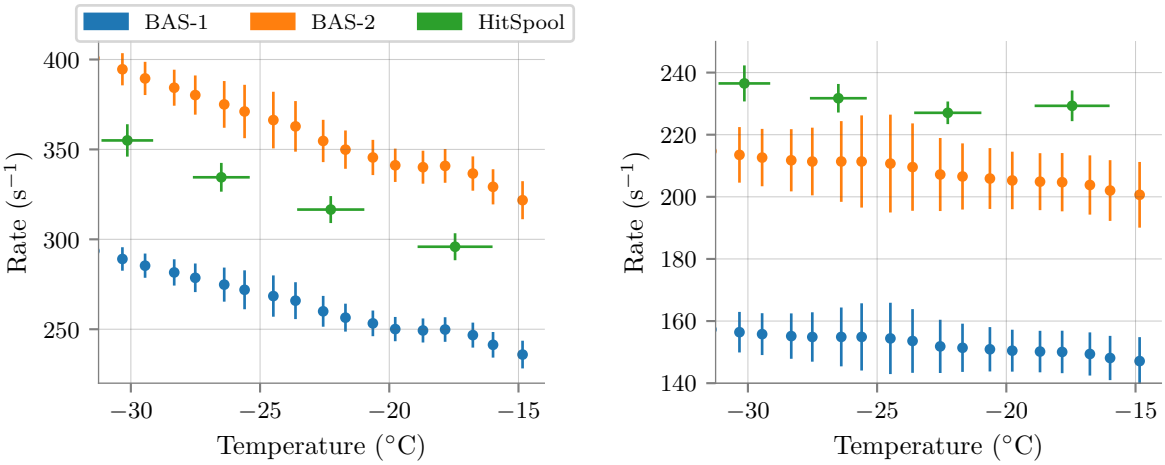

Fig. 9.8: Temperature-dependence of the background rate caused by radioactive decays inside the glass of the DOM, simulated using the two sets of isotope activities BAS-1 (blue) and BAS-2 (yellow). The large uncertainties are caused by the systematical error of the yield and isotope activities. For comparison is also depicted the DOM background rate calculated with the HitSpool data (taken from [18]). The latter also includes the dark rate of the PMT. **Left:** rate of the correlated and **right:** of the uncorrelated noise.

The simulated temperature dependence shown by the correlated part of the background (left side of figure 9.8) is in good agreement with the experimental data. This behaviour is a direct result of the dependency shown by the scintillation yield of the glass. However, the absolute values of the rate do not coincide with each other, as the set of isotope activities BAS-2 result in a higher, while the one of BAS-1 in a lower rate compared to the HitSpool data. Since in this thesis the amount of radioactivity of only two Benthos samples was measured, it is not known how much the activities vary between the pressure vessel of different DOMs. As the experimental data is the average of several modules, it could be asserted that the mean isotope activity lies between the sets measured in this work, assuming that every scintillation parameter is correct. Anyway, the correlated rate of the HitSpool data also includes the afterpulsing of the PMT, thus the rate caused by radioactive decays is a bit lower than the one shown in figure 9.8.

The analysis of the uncorrelated part, shown in the right side of figure 9.8 is more complex, as most of the dark rate of the PMT contributes to the Poissonian noise. The influence of the PMT can be clearly seen, as the rate starts to increase with higher temperatures at around $-20\,°C$ due to the thermionic emission. However, the PMT dark rate is not known with great precision, as the measurements done with bare PMTs can not completely reproduce the optical coupling inside the DOM. In [66], the PMT dark rate was determined to be close to $300\,s^{-1}$ in the $-40\,°C$ to $-20\,°C$ range. In this measurement, an artificial dead time of $6\,\mu s$ was added, which suppressed around the half of all afterpulses. If the PMT dark rate in the DOMs is of the same order, then the uncorrelated part of the HitSpool data would be almost exclusively caused by the PMT. This would mean that there is a big overestimation done in the simulations of this thesis. In order to maintain the values of the correlated rate of the background caused by radioactive decays and reduce its uncorrelated contribution, the yield of the glass would have to be larger (see right side of figure 9.6), and thus also the isotope activity inside the glass would have to be lower. This makes evident the requirement for more statistics for

both, the scintillation parameters and the amount of radioactivity expected to be found in the glass, if the causes of the different features of the background are to be determined with greater precision.

9.3 mDOM

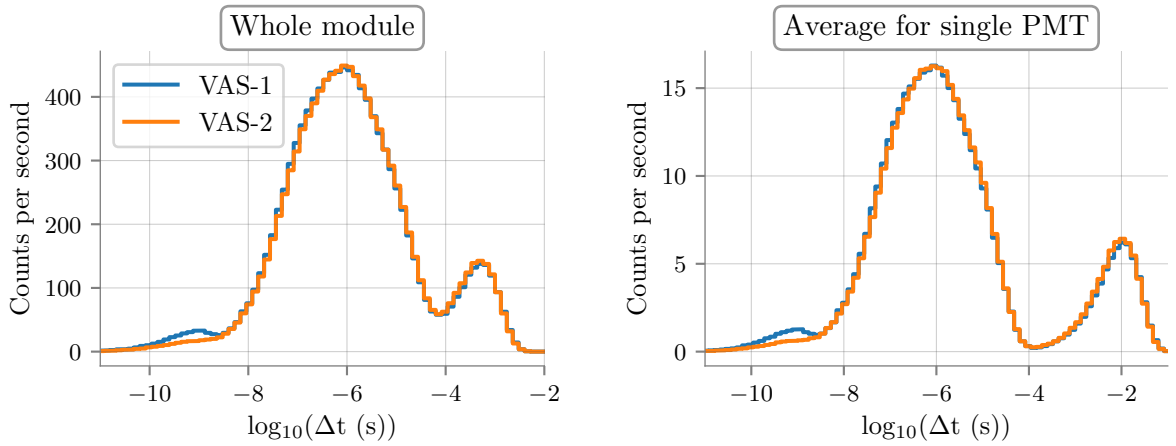

Fig. 9.9: Simulated time between subsequent hits in $\log_{10}(\Delta t)$ for an mDOM in ice at −35 °C. **Left:** the distribution combining all hits of the module, **right:** the average distribution only considering the hits at single PMTs. Two sets of isotope activities labelled as VAS-1 and VAS-2 were used (see text). The statistical uncertainty is not depicted, as it is smaller than the line width.

In chapter 6 the amount of radioactivity in four Vitrovex samples was determined. Three of them exhibited similar activities (see table 6.2 and 6.3), as they belong to the same production batch. In this section, the average of these three results will be used and referred as "VAS-1". The results for the Vitrovex half vessel (see table 6.3) as "VAS-2". With this information and the scintillation parameters of the Vitrovex glass measured in chapter 8, the Δt distribution can be simulated for the mDOM as done in the last section for the DOM. In this case, an mDOM surrounded by ice at −35 °C is simulated only taking into account glass scintillation for a pressure vessel of 13 kg. Considering that the mDOM features 24 PMTs, the background can be given considering the whole module or only single PMTs. Figure 9.9 shows the noise time distribution for both cases. Since in the case of the whole module the uncorrelated noise detected at all PMTs is summed to a single rate, the Poissonian peak exhibit a maximum at a shorter time than in the curve for a single PMT. The two isotope activity sets VAS-1 and VAS-2 yield almost the same results, with the most noticeable deviation at the very short time differences. This is due to the big contrast of ^{40}K activity with VAS-1 featuring $(61.0 \pm 0.9)\,\frac{\mathrm{Bq}}{\mathrm{kg}}$ and $(0 \pm 1)\,\frac{\mathrm{Bq}}{\mathrm{kg}}$ for VAS-2. The 89 % of ^{40}K decays emit an electron with mean energy 560 keV [57] and is therefore one of the main sources of Cherenkov light in the glass. However, as aforementioned, this difference would not manifest itself in measurements, as the pulse length (FWHM) of the PMTs is $\sim$ 5 ns, merging almost all Cherenkov photons in one pulse.

A novel feature offered by the mDOM design is the possibility of using coincidences between different PMT in the data analysis. In this regard, it will be important to set

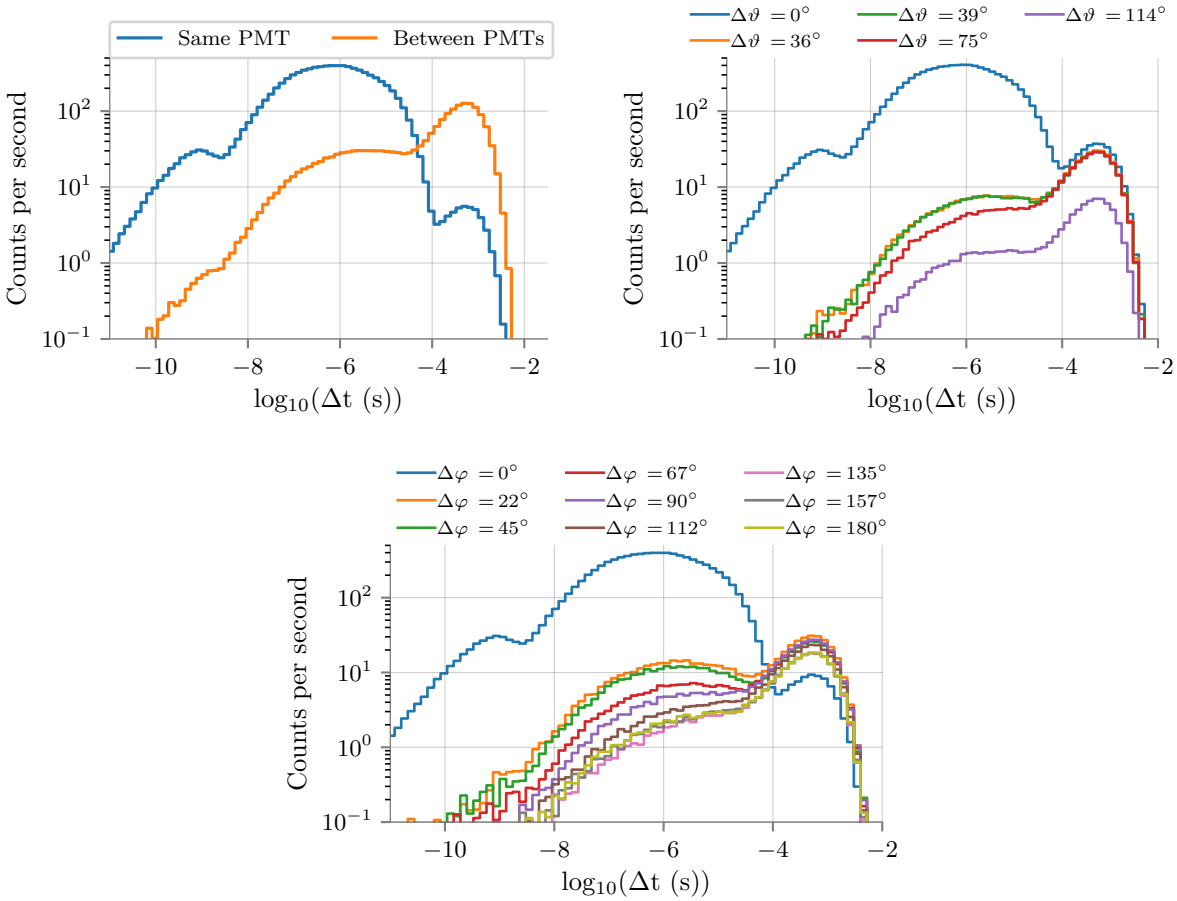

Fig. 9.10: Time between subsequent hits considering different PMT pairs. **Top left:** comparison of coincidence rate with the same PMT (blue) and different PMT (yellow). **Top right:** coincidence rate separating the PMT regarding their ϑ angle difference, **bottom** regarding their φ angle difference.

trigger conditions (either online in the DAQ or in the reconstruction algorithms) that suppress most of the coincidences caused by the background. With this motivation, the time distribution for background coincidences between PMTs will be briefly investigated next.

Since the output of the simulation entails the PMT number for every hit, the coincidences between PMTs can be analysed from the same data. For this, the data set from the simulation of VAS-1 at −35 °C presented in figure 9.9 is used. First, the most basic investigation is to separate the Δt distribution from subsequent hits detected in the same PMT from those that were measured at different PMTs. The results are shown on the top left side of figure 9.10. Here, the shortest Δt are measured at the same PMTs, while most of the uncorrelated noise is measured at different sensors. This is to be expected since the radioactive decays are localised in a single point of the glass volume. Therefore, the detection of the scintillation and Cherenkov photons will occur most probably at the nearest PMT from the decay. On the

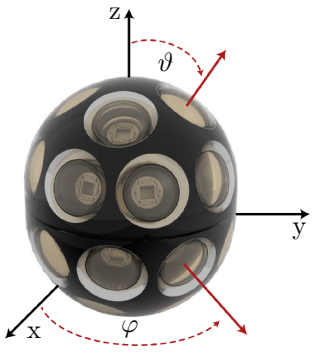

Fig. 9.11: Frame of reference used in this section.

other side, the Poissonian peak is caused by the Δt from the last and first detected photon from different radioactive decays. As these decays take place at different locations, the uncorrelated part is mostly measured by different sensors. Without considering the effects of the PMT pulse length and TTS, it is expected a rate of $(224.4 \pm 0.6)\,\mathrm{s}^{-1}$, $(67.9 \pm 0.4)\,\mathrm{s}^{-1}$, $(13.2 \pm 0.2)\,\mathrm{s}^{-1}$ and $(2.96 \pm 0.08)\,\mathrm{s}^{-1}$ of noise at different PMTs occurring in a time interval shorter than 1 μs, 100 ns, 10 ns and 1 ns, respectively. The uncertainty of these values only considers the statistical error from the simulations.

The coincidence distributions can be further broken down by taking into account the position of the PMTs. Figure 9.11 displays the frame of reference used, where the origin is the centre of the mDOM. The location of each PMT corresponds to a (ϑ, φ)-pair determined by the line that pass through the centre of the PMT's photocathode and the origin. The top right side of figure 9.10 presents the noise time distribution regarding the angle difference $\Delta\vartheta$ between the subsequently hit PMTs. Since in the mDOM design there are four rings of sensors symmetrically positioned along the z-axis, there are five different possible $\Delta\vartheta$ values. The curve in the case of $\Delta\vartheta = 0°$ exhibits the highest counts for correlated background, as this includes the Δt for hits at the same PMT. As expected, the probability for coincidences from the scintillation noise decreases the further away the PMT pairs are, while the intensity of the uncorrelated peak does not depend on the PMT location, except for the case $\Delta\vartheta = 114°$. Only PMTs on the rings at the extremes of the mDOM contribute to this angle difference. Since these rings have only four PMTs each, while the rings from the mid section have eight, the rate of uncorrelated coincidences is smaller. The same analysis can be done separating the Δt distributions regarding the $\Delta\varphi$ distance between subsequently hit PMTs. The results are depicted in the lower part of figure 9.10. Here, similar conclusions can be drawn as in the case of the $\Delta\vartheta$ separation, exhibiting a higher rate of coincidences in the correlated part of the distribution the smaller the angle difference $\Delta\varphi$. The only exception is the distribution for$\Delta\varphi = 135°$, which features the lowest rate. This can be explained applying the same reasoning as before, since only the 8 PMTs from the outer rings contribute to this distribution.

These results indicate that it is possible, if is necessary for a trigger algorithm, to reduce the background coincidence rate between PMTs by considering the PMT position. For example, if only are taken into account coincidences between PMTs separated by at least one ring ($\Delta\vartheta = 114°$ and $\Delta\vartheta = 75°$), the expected rate is reduced to $(42.4 \pm 0.3)\,\mathrm{s}^{-1}$, $(12.7 \pm 0.2)\,\mathrm{s}^{-1}$, $(2.45 \pm 0.07)\,\mathrm{s}^{-1}$ and $(0.54 \pm 0.03)\,\mathrm{s}^{-1}$of coincidences occurring in a time interval shorter than 1 μs, 100 ns, 10 ns and 1 ns, respectively.

Background rate as a function of the temperature

The temperature-dependence of the background rate caused by radioactive decays is simulated the same way as in section 9.2. The results for both isotope activity sets VAS-1 and VAS-2 are depicted in figure 9.12. Like in the case of the DOM, the correlated noise features almost the same temperature-dependence of the scintillation yield of the glass - the division between the average number of hits $H(T_i, I)$ and the simulated yield is similar for all temperatures. In the case of the Benthos glass, this is to be expected, since the lifetime did not change much with temperature (see section 8.2). However, the time constant measured with the Vitrovex sample did exhibit an increase with lower temperatures. This suggests that the lifetime, at least in the μs level, does not influence a lot the expected noise rate. The average number of hits per decay (in the case of the natural chains this means the decay of the whole isotope chain) divided by the yield is summarised

in table 9.1 for the three natural chains and ^{40}K. The most important relative contribution is from ^{238}U series, which is not surprising, considering that this chain exhibits three isotopes more than the ^{235}U and ^{232}Th chains (see table 6.1).

The rate per PMT was calculated considering no dead time and with 2.45 μs dead time between hits, in order to be able to compare the results with the DOM. First is to be noted that with both isotope activity sets almost the same results are obtained. At −35 °C and considering no dead time, the expected rate is $(428 \pm 13)\,\mathrm{s}^{-1}$ and $(430 \pm 14)\,\mathrm{s}^{-1}$ for VAS-1 and VAS-2, respectively. A (13.6 ± 0.1) % of this rate is uncorrelated. Applying a dead time of 2.45 μs, the rate is reduced to $(230 \pm 5)\,\mathrm{s}^{-1}$ (VAS-1) and $(240 \pm 6)\,\mathrm{s}^{-1}$ (VAS-2), whereas the uncorrelated rate remains almost unchanged (its relative contribution is increased to (23.0 ± 0.1) % of the total). Considering that $\log_{10}(2.45\,\mu\mathrm{s}) = -5.61 \log_{10}(\mathrm{s})$, the maximum of the Poissonian peak in figure 9.9 lies far from the dead time cutoff and thus is not greatly affected by it.

All the calculations so far have assumed that the scintillation yield for electrons is 9.5 times larger than the one for α-particles, which is based on measurements done in other glass samples [41 (p. 255)]. This is however only an assumption and the real factor will most probably be different. In order to estimate how much the rate calculated in this section would change with this parameter, the simulations were done again varying the

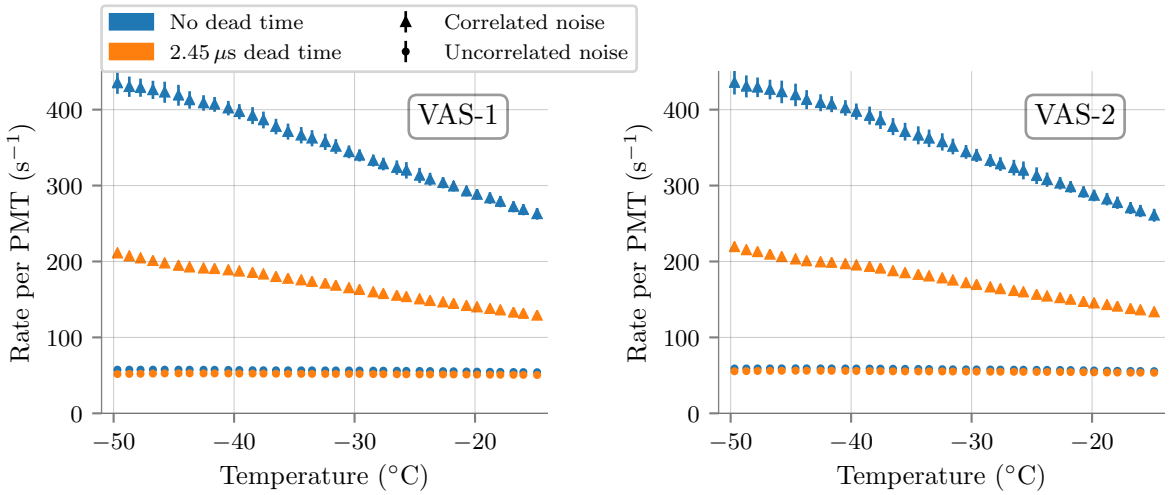

Fig. 9.12: Simulated background rate per PMT from radioactive decays inside the mDOM vessel as a function of the temperature, without (blue) and with a dead time of 2.45 μs (yellow). The large uncertainties are caused by the systematical error of the yield and isotope activities.

Table 9.1: Average number of detected photons per decay in the vessel glass (in the case of the natural series, after the decay of a whole chain) divided by the simulated yield for ^{40}K and the natural decay series.

	Hits per decay per yield $\times 10^{-2}$
^{40}K	0.4089 ± 0.0004
^{238}U-chain	5.296 ± 0.002
^{235}U-chain	4.543 ± 0.001
^{232}Th-chain	4.264 ± 0.002

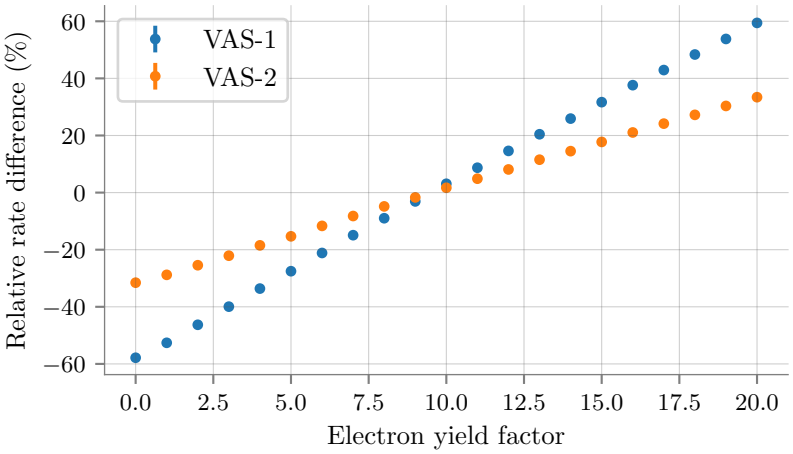

Fig. 9.13: Relative difference of the background rate for different electron yield factors in respect to the scintillation yield of α-particles. The rate calculations done in this section assumed a factor of 9.5.

electron yield factor from 0 to 20. The results are shown in figure 9.13. Since VAS-1 exhibits a much larger amount of ^{40}K the background is more strongly dependent on the electron yield factor than in the case of VAS-2, which features only the beta decay from the natural chains. If the scintillation yield would be the same as for α-particles, the rate presented in figure 9.12 would be $(52.61 \pm 0.04)\,\%$ and $(28.81 \pm 0.07)\,\%$ lower for a pressure vessel with the amount of radioactivity VAS-1 and VAS-2 respectively. This means, without a set dead time, at $-35\,°\mathrm{C}$ each PMT would be expected to measure a rate of $(203 \pm 6)\,\mathrm{s}^{-1}$ (VAS-1) and $(306 \pm 10)\,\mathrm{s}^{-1}$ from light produced by radioactive decays. Conversely, if the electron yield factor would be the double (19), the expected rate per PMT would rise by $(53.81 \pm 0.15)\,\%$ (VAS-1) and $(30.35 \pm 0.13)\,\%$ (VAS-2), which results in $(658 \pm 20)\,\mathrm{s}^{-1}$ and $(560 \pm 18)\,\mathrm{s}^{-1}$ respectively. Unfortunately, the β-sources available for this work were not suitable for a yield measurement. However, as long as the scintillation yield for electrons is not measured with a Vitrovex sample, it is difficult to make a more precise evaluation of the expected rate for the mDOM.

9.4 Influence of gel scintillation

So far the simulations have not considered the scintillation of the optical gel. In chapter 8 some luminescence could be measured from both brands, QSI and Wacker. Nevertheless, the gel samples studied with gamma spectroscopy featured no measurable radioactivity. This means that this material will only emit photons when particles from decays in the pressure vessel pass through the gel.

In order to find out if the luminescence of the gel should be a concern, radioactive decays in the glass of the module were simulated like done in section 9.2 and 9.3, but this time the gel was defined as the scintillating material instead of the glass. The Cherenkov effect was turned off in these simulations, in order to ensure that only the rate of the gel luminescence is being calculated and no dead time between hits was included. Furthermore, the parameters of the QSI gel brand were used for both modules, since the

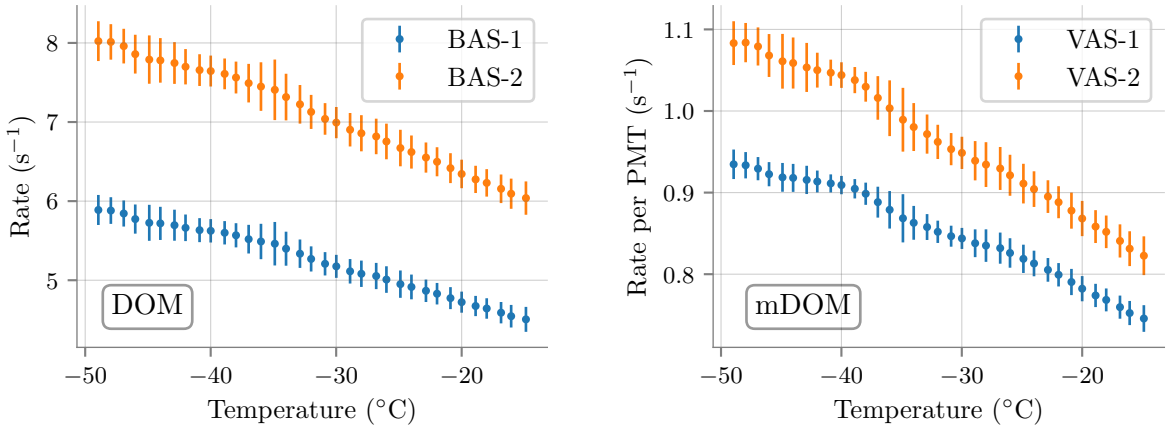

Fig. 9.14: Background rate stemming from scintillation of the optical gel expected to be measured in the DOM (**left**) and mDOM (**right**). The large uncertainties are caused by the systematical error of the yield and isotope activities.

scintillation yield of the Wacker sample could not be measured. The results are shown in figure 9.14.

It is noteworthy that the scintillation background expected to be caused by the gel is neglectable compared to the one caused by the pressure vessel. For the DOM this has as a maximum of $\sim 8\,\mathrm{s}^{-1}$ with the activity set BAS-2 and for the mDOM less than $1.1\,\mathrm{s}^{-1}$ per PMT is expected to be measured, considering the set VAS-2. In chapter 8 it was estimated that the Wacker gel emits photons mostly in the UV-region under 300 nm and therefore the rate presented in figure 9.14 is an overestimation for the mDOM if the Wacker gel were to be used. Nevertheless, the crystallisation of this gel observed during the investigations of this work, excludes it from being considered for the mDOM design.

10 Summary and outlook

The aim of this work was to study the background caused by radioactive decays inside the multi-PMT digital optical module, a new optical sensor being proposed for future IceCube extensions. As the deep ice at the South Pole has a very low optical activity, light produced by the mDOM itself represents the dominant background source. Two major sources are Cherenkov and scintillation light produced by radioactive decays inside the glass of the module's pressure vessel. Since so far the luminescence of the glass has not been studied in great detail, the main focus of this thesis was its characterisation. This included the determination of the amount of radioactivity found in the material, as well as the full parameterisation of the observed scintillation. In this context, not only the glass was studied, but also the gel used as an optical coupler between the PMTs and the glass of the module was investigated.

In the scope of this thesis two glass brands were studied - Vitrovex, which will be used in the mDOM prototype, and Benthos glass of the original IceCube DOM - and also two gel brands - Wacker SilGel 612 and the current default QSI Qgel 900. During the investigations of this work, it was observed that the Wacker gel undergoes undesired crystallisation, turning hard and opaque at low temperatures, which excludes it from being considered for the mDOM design.

The amount of radioactivity in these materials was investigated by means of gamma spectroscopy. A quantitative and qualitative analysis was conducted for a total of eight gamma-ray spectra, considering four Vitrovex samples, two Benthos specimens and one sample of each gel brand. In all glass samples, gamma-ray emission from isotopes of the three natural decay chains - ^{238}U, ^{235}U and ^{232}Th - was measured. The calculation of their activity indicated that these decay series were in good approximation in secular equilibrium, which allows to estimate the activities of isotopes that cannot be measured with gamma spectroscopy. Furthermore, ^{40}K was found in three of the Vitrovex samples. These stem from the same production batch and showed similar activities for all detected isotopes, but did deviate a lot with the results of the fourth sample, which exhibited no measurable amounts of ^{40}K. This is also true in the case of the Benthos samples. This suggested that the amount of radioactivity found in the pressure vessels is highly dependent on the production batch. Therefore, more samples should be investigated, in order to make an estimation of how much these values vary between different batches. Moreover, it is very important that the pressure vessel of the first mDOM prototype is studied with gamma spectroscopy before the integration of the module, since the size of the setup was too small for conducting such a measurement during this work.

In the case of the gel samples, no measurable amount of radioactivity was detected.

The light from scintillation was characterised considering its energy spectrum, the time distribution of the emission and the number of photons released per energy absorbed. Starting with the **scintillation spectrum**, it was possible to measure the wavelength of the luminescence from the exposure of the samples to two different radioactive sources, an ^{241}Am- α- and a stronger ^{90}Sr- β-source. This gave some information about the nature of

this process, as the measured spectra lie near the band gap energy of the material, meaning that the radiative transitions are produced most probably by defects near the conduction and valence band and excluding the possibility of a unique de-excitation centre from the contamination of rare-earth elements. In the case of the Wacker gel sample, no spectrum was measured with the α-source, since, following the same reasoning, the bandgap energy of this material lies in the UV-region, where the used PMT is not sensible. A signal was measured with the β-source, although this was shown by comparing it with simulations to be most probably only Cherenkov radiation.

Yet, there is room for improvement of the experimental approach, as different factors affected the results. On the one hand, the α-source excited the air in its surrounding, contaminating the results with the discrete emission of molecular nitrogen. This radioactive source also yields a low-emission intensity, and therefore, a rather low signal to noise ratio. On the other hand, the β-source provided better results regarding noise, but it also generated Cherenkov photons. Additionally, as the emission was near the transmission cutoff of the sample, information was lost and the real spectrum could not be measured.

A better approach would be to take advantage of the fact that scintillation light is emitted in all directions equally. Hence, one could measure the light that travelled the shortest path through the sample[1], by irradiating the sample with α-particles with a particular angle towards the entrance of the optical system (see figure 10.1). This requires, however, two conditions: on the one hand, the measurement has to be done in a low-pressure environment, so that the α-particles reach the sample and to reduce the air scintillation. Also, the α-source should have an activity in the order of hundreds of GBq for a better signal to noise ratio. This activity may need to be even higher, considering that probably the light must be coupled into an optical fibre if the vacuum chamber is not big enough for the monochromator, which would severely reduce the detection efficiency. This setup, however, should deliver results with no external contamination and almost no information loss due to absorption inside the glass. Also, a PMT sensible in the region between 200-300 nm should be preferred, as the transmission cutoff of the PMT's window is the next limiting factor after the absorption of the samples.

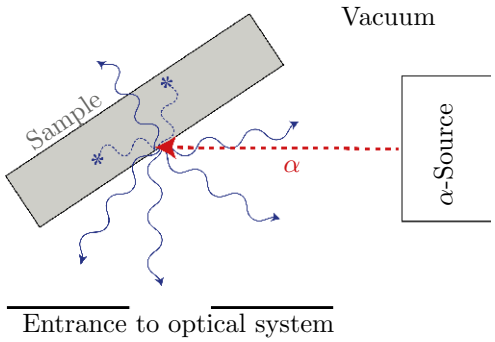

Fig. 10.1: Experimental approach for an improvement of the scintillation spectrum results. The sample is positioned at an angle towards the optical system, such that only photons that travelled a short path through the sample are measured.

Furthermore, the spectrum measurement should be done at different temperatures, as the scintillation spectrum of most semiconductors changes with it. However, such a study requires first the investigation of the QE of the PMT and the absorption length of the samples as a function of the temperature.

The measurement of the **lifetime** resulted in a long time distribution in the order of μs for the emission of the glass samples and a much faster one in the order of ns in the case of the gel specimens. For both gel and the Vitrovex sample, the average lifetime decreased with higher temperatures, which was not the case for the specimen of the Benthos glass. This decrease was expected for materials where thermal quenching is

[1] Only a few μm for excitation with alpha particles.

an important nonradiative process since it is more probable to release the energy through phononic vibrational states, if these are in higher (thermal) energy levels. However, the measurement was constrained by two factors. On the one side, the number of data points measured in the temperature range was limited by the long duration of the measurement to only five temperatures between −50 °C and −15 °C. In the context of the background simulation of the optical modules, this should not represent any major problem, as the data can be interpolated. Nevertheless, more measurements at different temperatures should be done, if interpretations of the underlying luminescence processes are to be made, especially with the glass samples, since these did show a more erratic behaviour with the temperature. On the other side, the lifetimes had to be corrected, as the time point of the decay was not known. This could be avoided by utilising a more complex setup. For example, the radioactive source could be surrounded by scintillators optically coupled with optical detectors, which can measure the gamma-rays emitted at the decays, e.g. the 59.5 keV photon emitted with a 35.9 % probability from the decay of ^{241}Am [57]. This would then trigger the measurement of the waveforms of the PMT measuring the luminescence of the samples, instead of using the first detected photon as the trigger, as it was done in this chapter. However, this would radically increase the duration of the measurement, which would restrain even more the statistics.

The determination of the **scintillation yield** is in hindsight of the other two parameters far simpler, as only the increase of the PMT rate is measured. All samples exhibited a rise of the emission with lower temperatures, except for the Wacker gel, as the crystallisation of the material changed the optical properties of the sample. In the case of the Benthos glass, this emission raise contradicts the results of the lifetime, which however could be explained by the low number of temperatures measured.

Moreover, for the calculation of the yield both, the spectra and lifetime of the samples are needed. Hence, any constraints and uncertainties applied to these parameters will also affect the yield results. In this regard, the main improvement for the determination of the yield would be more precise measurements of the lifetime and scintillation spectra, although better results could also be obtained by measuring the rates in a low-pressure environment in order to prevent air scintillation. Furthermore, in this chapter only the yield for α-particles was investigated. As introduced in chapter 4 the intensity of the emission changes with different kind of charged particles, viz. the yield for electrons is normally larger than for heavier particles like protons or α-particles. The β-sources that were available for this work were either too strong or encapsulated in transparent plastic, which will probably scintillate by itself. Thus, these sources have to be characterised in more detail if the yield for electrons is to be determined. In addition, the effects of the radiation damage observed on the glass samples regarding the calculated yield should be investigated. A possibility for this would be to measure the rate of scintillation light for a long period with a constant temperature, in order to observe any decrease of the emission due to the darkening of the material caused by the radiation damage.

Another remark, it is important to observe that there is a lack of statistic as only one sample of every brand was measured. Since the best assumption is that the scintillation is produced by lattice defects and/or impurity atoms, the luminescence properties will probably vary between different samples, especially between specimens from different production batches. Hence, more samples should be studied for their scintillation properties, in order to determine an expected deviation of the luminescence parameters for the optical modules.

With the parameterisation of the scintillation, it is possible to simulate the background from radioactive decays expected to be measured with the mDOM in the deep ice. For this, a combination of a Geant4 and a Python code was developed, which enables the investigation of the time distribution of the background and coincidences between PMTs. Regarding this, some brief simulations were done, which showed that the amount of coincidences is highly dependent on the distance between the coincident PMTs. Taking into account the measured isotope activities, the expected rate per PMT stemming from radioactive decays at $-35\,°\mathrm{C}$ was calculated to be $(429 \pm 14)\,\mathrm{s}^{-1}$. The scintillation of gel from radioactive decays inside the pressure vessel is relative to this rate neglectable, adding less than $1.1\,\mathrm{s}^{-1}$ to the total.

An important caveat, however, is that in the calculation of this rate it was assumed a yield for electrons 9.5 times larger than the one determined for α-particles. It was calculated that this rate value would change several tens of percentage points for different electron yield factors. This makes necessary the determination of this parameter in further studies.

In order to validate the methods used in this work, also the background of the DOM was investigated. Here, the simulated rate and time distribution are in good agreement with the experimental data of IceCube. Yet, both, in the IceCube data, as well as in measurements done with a Benthos vessel, correlated noise in long time differences was observed. Due to its temperature behaviour, it is a fair guess to say that it also originates from scintillation light. Owing to the activity of the used α-source and the set waveform length of $100\,\mu\mathrm{s}$, such a long-lived lifetime cannot be measured with the setup used in this work. Further experiments should be conducted in order to confirm these long lifetime emissions in both glass brands.

A Appendix

Gamma spectra of all measured samples

The following figures show the gamma spectra of the Benthos sample measured at the University of Alberta (figure A.1) and the samples measured in the scope of this work: both small Vitrovex samples labelled as VV-1 (figure A.2) and VV-2 (figure A.3), the Vitrovex half pressure vessel (figure A.4), the Benthos half pressure vessel (figure A.5) and the gel samples Wacker SilGel 612 and QSI Qgel 900(figure A.6). Most of the identified peaks are labelled. The colour of the text corresponds to the decay chain of the isotope (red the ^{232}Th-series, blue ^{238}U- and yellow the ^{235}U-chain). The spectra of the optical gel samples do not differ from the background and therefore were illustrated in the same figure. The mass-specific activities for the isotopes summarised in table 6.2 and 6.3 (on page 38 and 40, respectively) were calculated with these spectra.

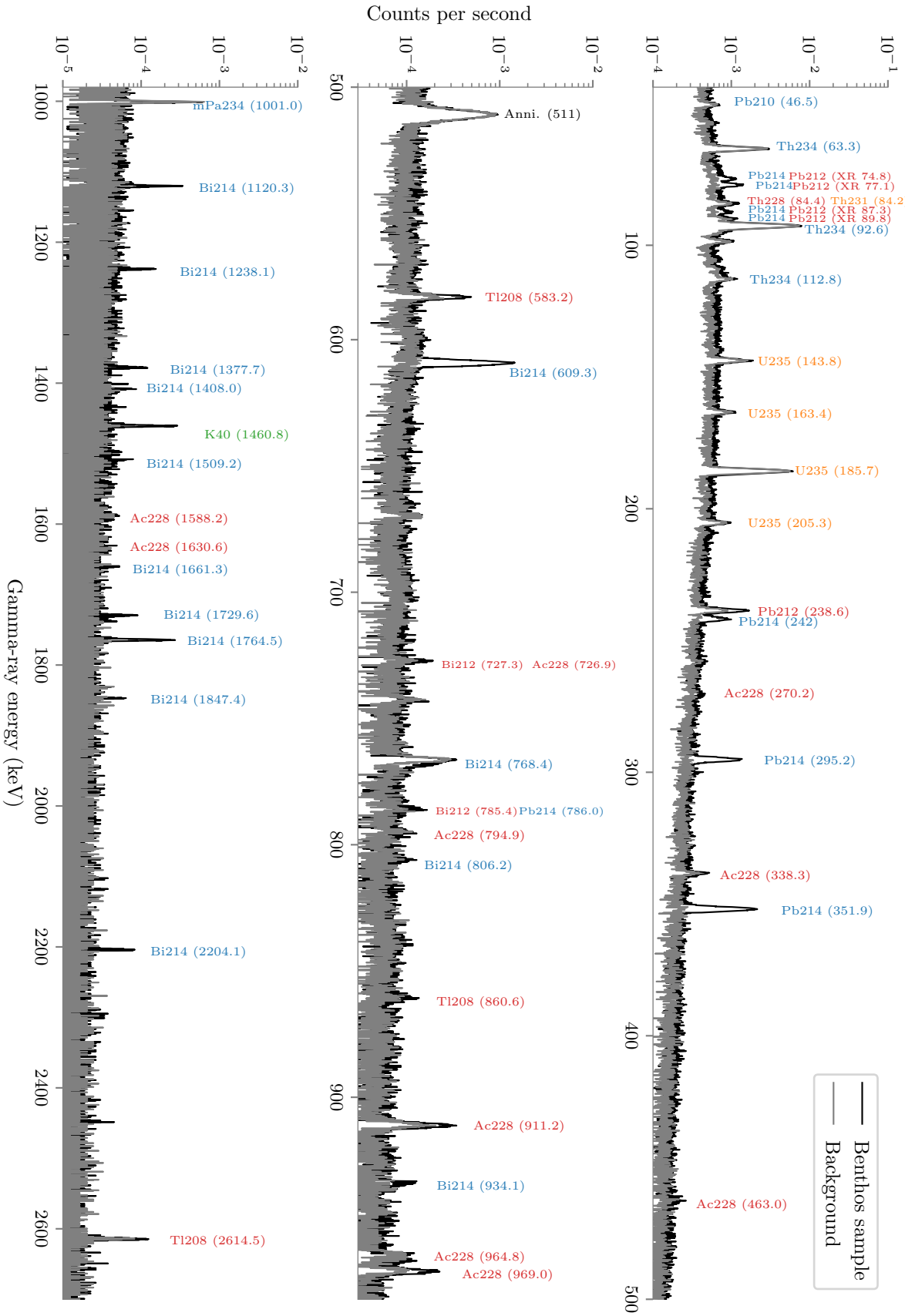

Fig. A.1: Gamma spectrum of the measurement of the Benthos glass sample and the background done at the University of Alberta.

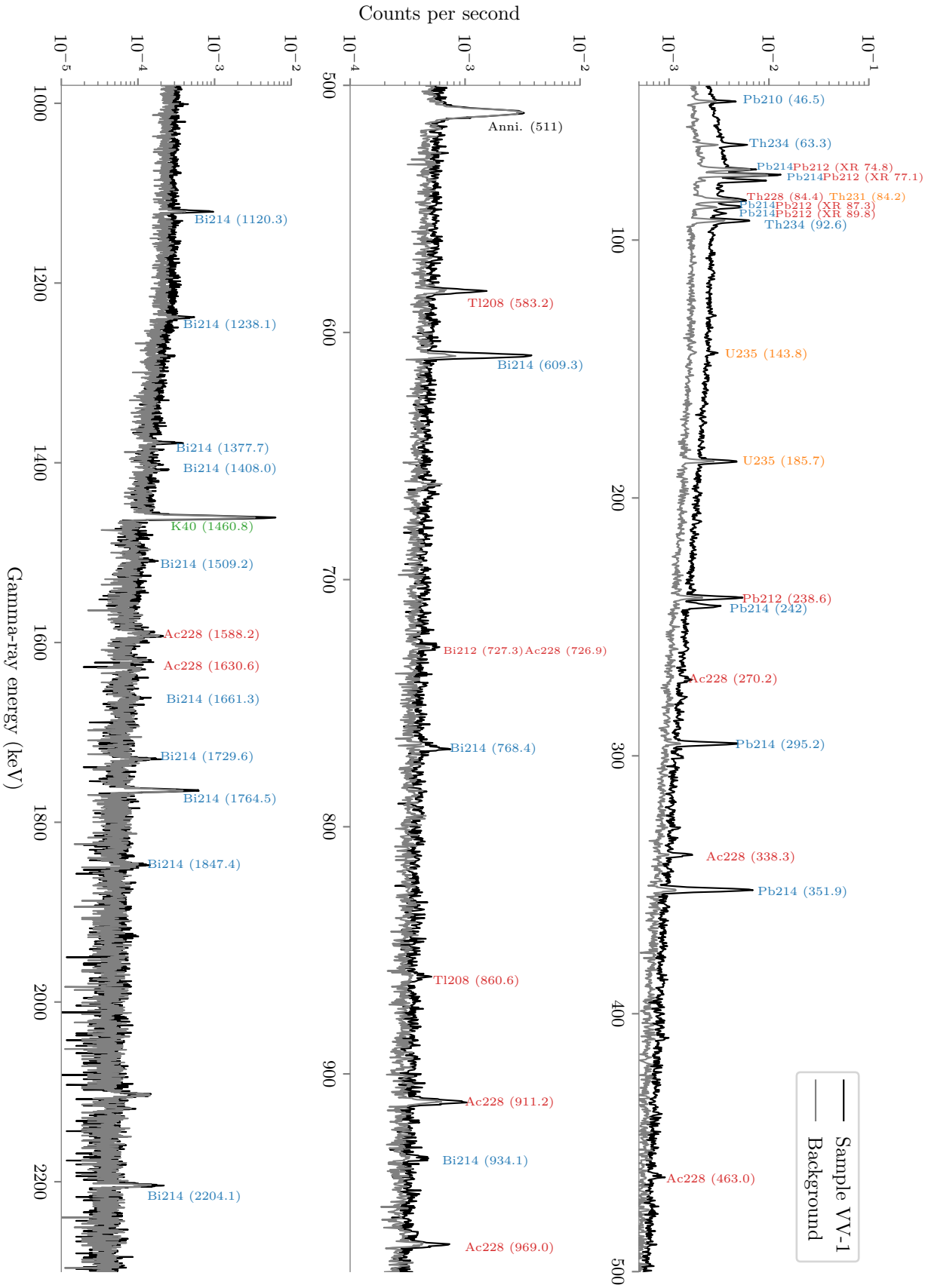

Fig. A.2: Gamma spectrum of the measurement of the small Vitrovex glass sample VV-1 and the background done at the University of Münster.

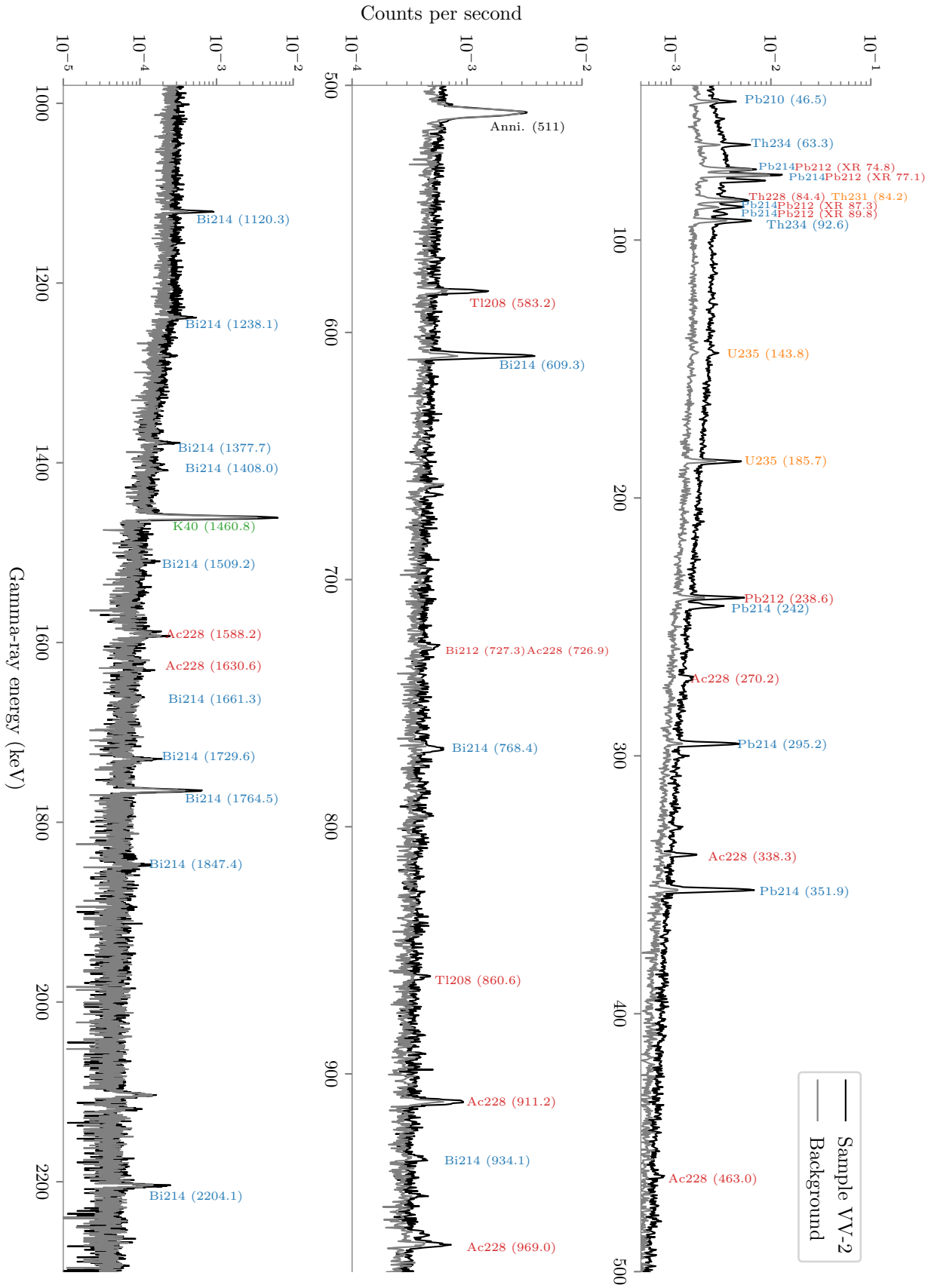

Fig. A.3: Gamma spectrum of the measurement of the small Vitrovex glass sample VV-2 and the background done at the University of Münster.

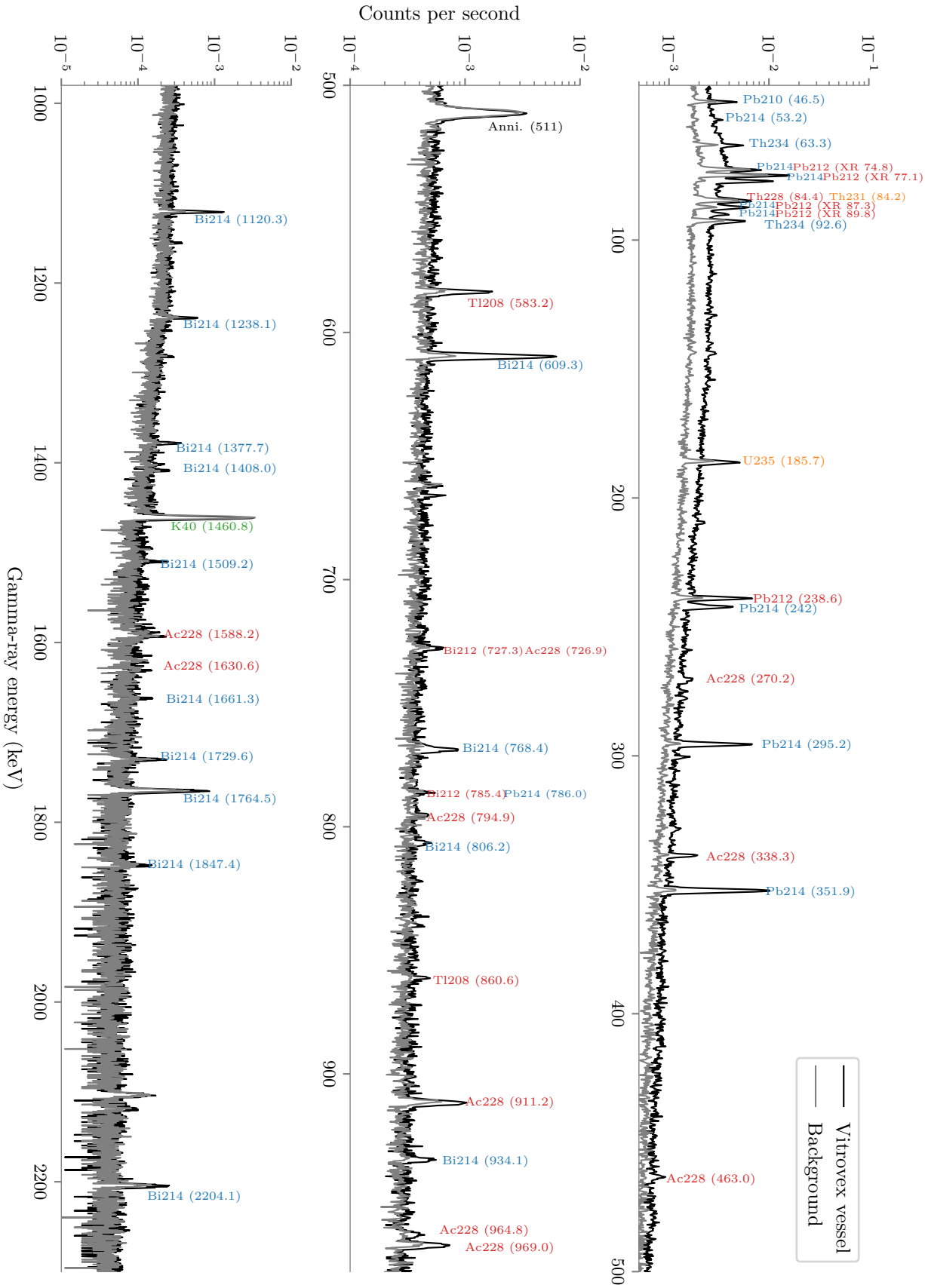

Fig. A.4: Gamma spectrum of the measurement of the Vitrovex vessel and the background done at the University of Münster.

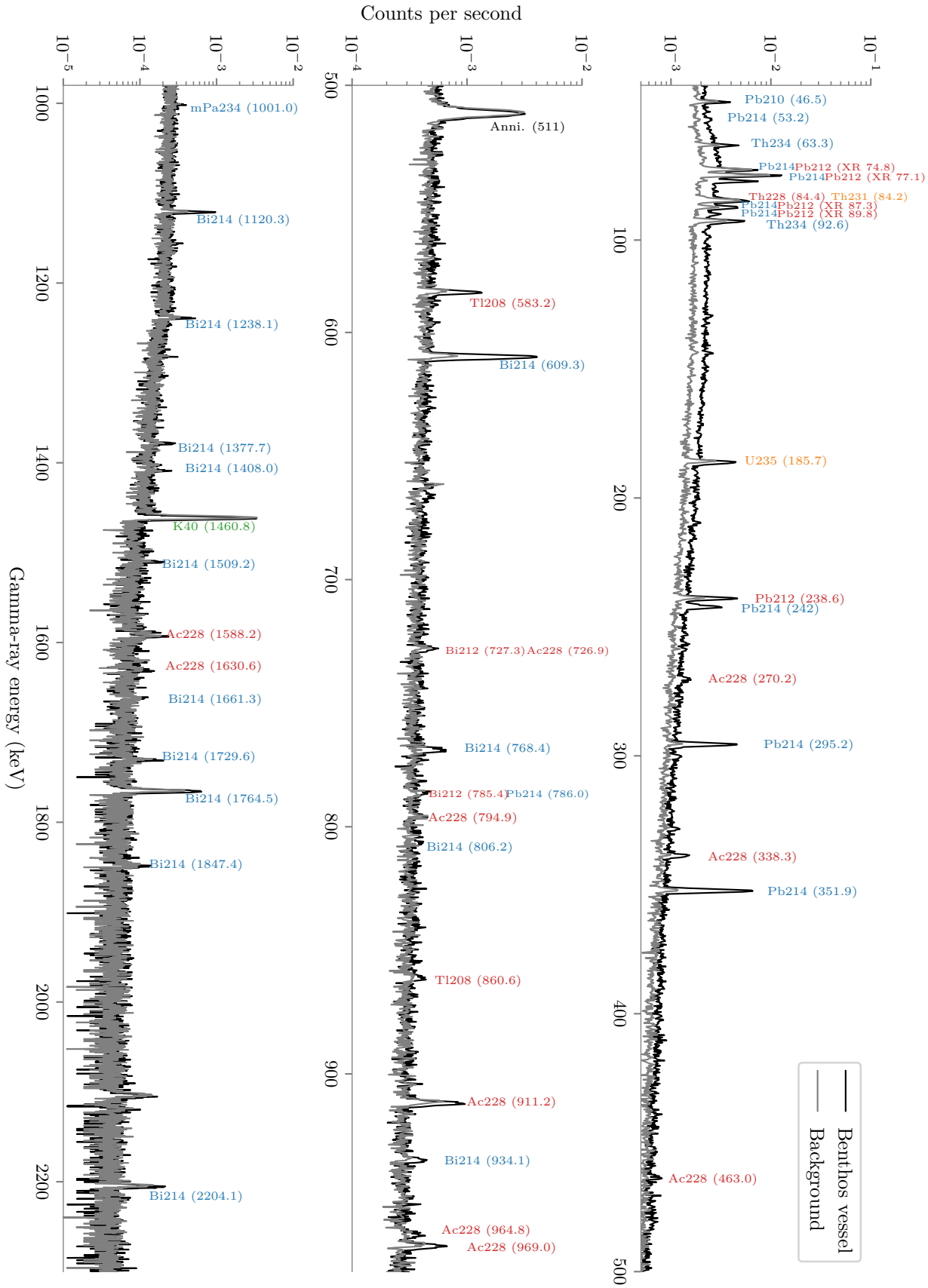

Fig. A.5: Gamma spectrum of the measurement of the Benthos vessel and the background done at the University of Münster.

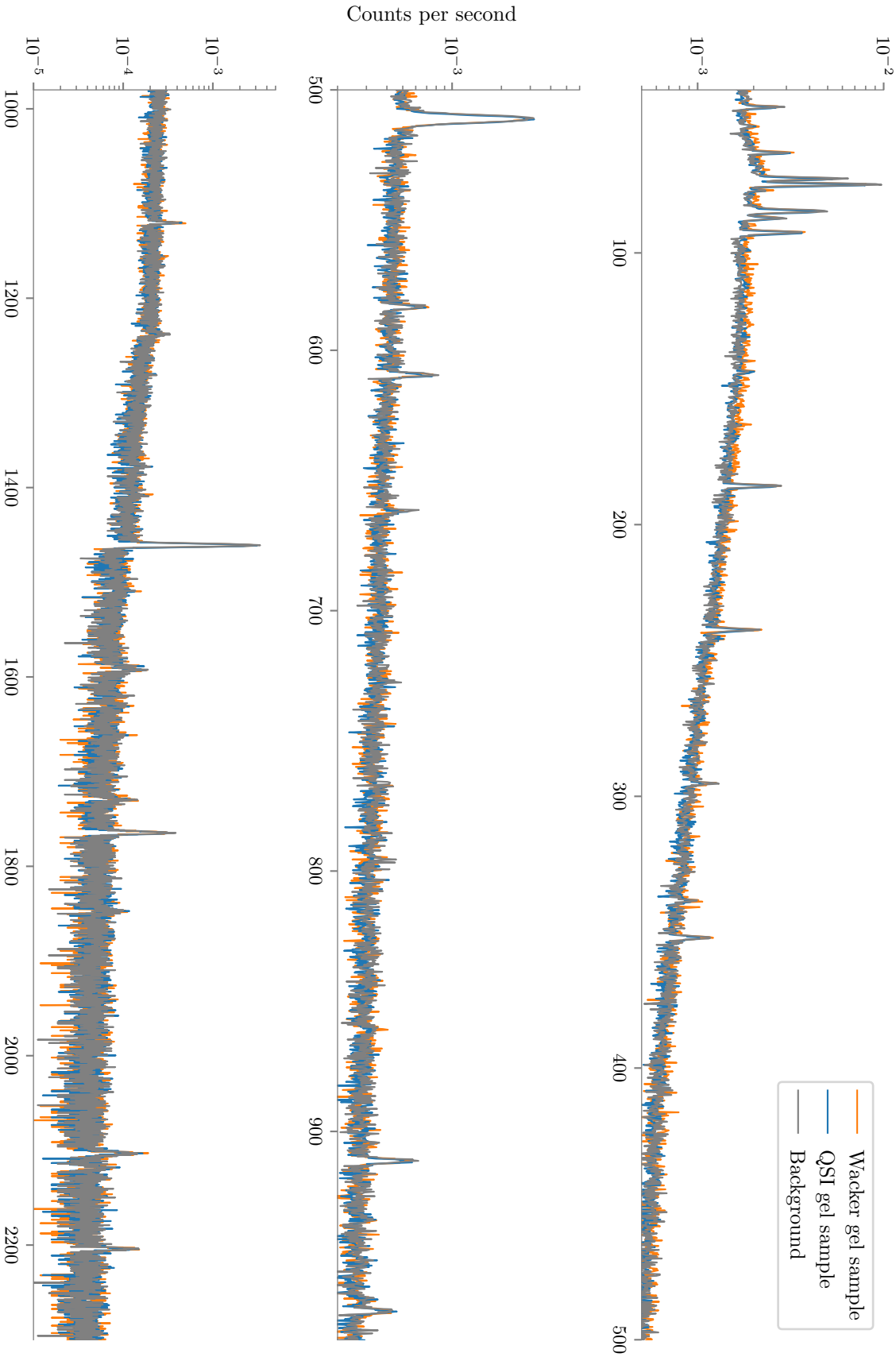

Fig. A.6: Gamma spectrum of the measurement of the gel samples, Wacker and QSI, and the background done at the University of Münster.

Bibliography

[1] B. P. Abbott, et al. (Virgo, LIGO Scientific Collaboration), *GW170814: A Three-Detector Observation of Gravitational Waves from a Binary Black Hole Coalescence*, Phys. Rev. Lett. 119 (14) (2017) 141101, Preprint 1709.09660.

[2] R. Schaeffer, *SN1987A: A Review*, Acta Phys. Polon. B21 (1990) 357–377.

[3] M. G. Aartsen, et al. (IceCube Collaboration), *Evidence for High-Energy Extraterrestrial Neutrinos at the IceCube Detector*, Science 342 (2013) 1242856, Preprint 1311.5238.

[4] M. G. Aartsen, et al. (IceCube Collaboration), *Constraints on Ultrahigh-Energy Cosmic-Ray Sources from a Search for Neutrinos above 10 PeV with IceCube*, Phys. Rev. Lett. 117 (24) (2016) 241101, Preprint 1607.05886.

[5] T. Eder, *Simulationsstudien zum Untergrund durch radioaktive Zerfälle in einem optischen Modul mit mehreren Photomultipliern für IceCube-Gen2*, Bachelor Thesis, Westfälische Wilhelms-Universität Münster (2016). URL `https://www.uni-muenster.de/imperia/md/content/physik_kp/agkappes/abschlussarbeiten/bachelorarbeiten/1609-ba_teder.pdf`

[6] K. Helbing, et al., *Light emission in Amanda pressure spheres*, AMANDA-Internal report (2003).

[7] O. Franzen, *Untersuchungen optischer module für das AMANDA- bzw. IceCube-projekt*, Diplomarbeit, Johannes Gutenberg-Universität zu Mainz (2003).

[8] T. K. Gaisser, R. Engel, E. Resconi, Cosmic Rays and Particle Physics, Cambridge University Press, 2016.

[9] D. V. Semikoz (Pierre Auger Collaboration), *Constraints on top-down models for the origin of UHECRs from the Pierre Auger Observatory data*, in: Proceedings, 30th International Cosmic Ray Conference (ICRC 2007): Merida, Yucatan, Mexico, July 3-11, 2007, Vol. 4, pp. 433–436, Preprint 0706.2960.

[10] U. F. Katz, C. Spiering, *High-Energy Neutrino Astrophysics: Status and Perspectives*, Prog. Part. Nucl. Phys. 67 (2012) 651–704, Preprint 1111.0507.

[11] A. Franceschini, G. Rodighiero, *The extragalactic background light revisited and the cosmic photon-photon opacity*, Astron. Astrophys. 603 (2017) A34, Preprint 1705.10256.

[12] K. Olive, *Review of particle physics*, Chinese Physics C 40 (10) (2016) 100001.

[13] J. S. Diaz, *Testing Lorentz and CPT invariance with neutrinos*, Symmetry 8 (10) (2016) 105, Preprint 1609.09474.

[14] R. Lehnert, *Cpt- and lorentz-symmetry breaking: a review* Preprint arXiv:hep-ph/0611177.

[15] M. Ageron, et al. (ANTARES Collaboration), *ANTARES: the first undersea neutrino telescope*, Nucl. Instrum. Meth. A656 (2011) 11–38, Preprint 1104.1607.

[16] I. A. Belolaptikov, et al. (BAIKAL Collaboration), *The Baikal underwater neutrino telescope: Design, performance and first results*, Astropart. Phys. 7 (1997) 263–282.

[17] P. A. Rapidis, *The NESTOR underwater neutrino telescope project*, Nuclear Instruments and Methods in Physics Research Section A: Accelerators, Spectrometers, Detectors and Associated Equipment 602 (1) (2009) 54–57.

[18] M. G. Aartsen, et al. (IceCube Collaboration), *The IceCube Neutrino Observatory: Instrumentation and Online Systems*, JINST 12 (03) (2017) P03012, Preprint 1612.05093.

[19] Z. Xing, S. Zhou, Neutrinos in particle physics, astronomy and cosmology, Zhejiang University Press Springer, Hangzhou Berlin New York, 2011.

[20] C. Backhouse, *Results from MINOS and NOvA*, Journal of Physics: Conference Series 598 (1) (2015) 012004.

[21] M. Duvernois, et al., *Radio detection of UHE neutrinos with the antarctic impulsive transient antenna (ANITA)experiment: Data and Analysis*, Vol. 5, 2005, pp. 107–110.

[22] C. Allen, et al., *Status of the radio ice cherenkov experiment (rice)*, New Astronomy Reviews 42 (3–4) (1998) 319–329.

[23] T. Meures, *The askaryan radio array (ARA)*, in: Development of a Sub-glacial Radio Telescope for the Detection of GZK Neutrinos, Springer International Publishing, 2015, pp. 37–57.

[24] J. V. Jelley, *Cerenkov radiation and its applications*, British Journal of Applied Physics 6 (7) (1955) 227–232.

[25] I. Frank, I. Tamm, *Coherent visible radiation of fast electrons passing through matter*, in: Selected Papers, Springer Berlin Heidelberg, 1991, pp. 29–35.

[26] M. G. Aartsen, et al. (IceCube Collaboration), *Neutrinos and Cosmic Rays Observed by IceCube* Preprint 1701.03731.

[27] M. G. Aartsen, et al. (IceCube Collaboration), *IceCube-Gen2: A Vision for the Future of Neutrino Astronomy in Antarctica*, PoS FRAPWS2016 (2017) 004, Preprint 1412.5106.

[28] P. Peiffer (IceCube-Gen2 Collaboration), *Overview and Performance of the Wavelength-shifting Optical Module (WOM)*, in: Proceedings, 35th International Cosmic Ray Conference (ICRC 2017): Bexco, Busan, Korea, July 10-20, 2017, PoS(ICRC2017)1052.

[29] A. Ishihara (IceCube-Gen2 Collaboration), *Overview and performance of the D-Egg optical sensor for IceCube-Gen2*, in: Proceedings, 35th International Cosmic Ray Conference (ICRC 2017): Bexco, Busan, Korea, July 10-20, 2017, PoS(ICRC2017)1051.

[30] L. Classen (IceCube-Gen2 Collaboration), *The mDOM – A multi-PMT Digital Optical Module for the IceCube-Gen2 neutrino telescope*, in: Proceedings, 35th International Cosmic Ray Conference (ICRC 2017): Bexco, Busan, Korea, July 10-20, 2017, PoS(ICRC2017)1047.

[31] L. Classen, *The mDOM - a multi-PMT digital optical module for the IceCube-Gen2 neutrino telescope*, PhD thesis, Friedrich-Alexander-Universität Erlangen-Nürnberg (2017). URL `https://www.uni-muenster.de/imperia/md/content/physik_kp/agkappes/abschlussarbeiten/doktorarbeiten/1702-phd_lclassen.pdf`

[32] C. J. Lozano Mariscal, *Studies on the sensitivity of multi-PMT optical modules to supernova neutrinos in the south pole ice*, Master thesis, Westfälische Wilhelms-Universität Münster (2017). URL `https://www.uni-muenster.de/imperia/md/content/physik_kp//agkappes/abschlussarbeiten/masterarbeiten/1702-ma_clozano.pdf`

[33] Photomultiplier tubes - Basics and Applications, 3rd Edition, Hamamatsu Photonics K.K., 2007. URL `https://www.hamamatsu.com/resources/pdf/etd/PMT_handbook_v3aE.pdf`

[34] S.-O. Flyckt, C. Marmonier, Photomultiplier tubes - principicles and applications, Photonis, 2002.

[35] T. Wright, A. Wright, The Photomultiplier Handbook, Oxford University Press, 2017.

[36] M. Suyama, K. Nakamura, Recent Progress of Photocathodes for PMTs, Proceedings of science, 2009. URL `https://pos.sissa.it/090/013/pdf`

[37] R. H. Fowler, L. Nordheim, *Electron emission in intense electric fields*, Proceedings of the Royal Society A: Mathematical, Physical and Engineering Sciences 119 (781) (1928) 173–181.

[38] B. Lubsandorzhiev, R. Vasiliev, Y. Vyatchin, B. Shaibonov, *Photoelectron backscattering in vacuum phototubes*, Nuclear Instruments and Methods in Physics Research Section A: Accelerators, Spectrometers, Detectors and Associated Equipment 567 (1) (2006) 12–16.

[39] E. H. Bellamy, et al., *Absolute calibration and monitoring of a spectrometric channel using a photomultiplier*, Nuclear Instruments and Methods in Physics Research A 339 (1994) 468–476.

[40] A. A. Jha, Inorganic Glasses for Photonics: Fundamentals, Engineering, and Applications (Wiley Series in Materials for Electronic & Optoelectronic Applications), Wiley, 2016.

[41] G. Knoll, Radiation detection and measurement, John Wiley, Hoboken, N.J, 2010.

[42] B. G. Yacobi, D. B. Holt, Cathodoluminescence Microscopy of Inorganic Solids, Springer US, 1990.

[43] R. Salh, *Defect related luminescence in silicon dioxide network: A review*, in: Crystalline Silicon - Properties and Uses, InTech, 2011.

[44] C. R. Ronda (Ed.), Luminescence: From Theory to Applications, Wiley-VCH, 2007.

[45] M. S. Akselrod, N. A. Larsen, V. Whitley, S. W. S. McKeever, *Thermal quenching of F-center luminescence in Al2O3:C*, Journal of Applied Physics 84 (6) (1998) 3364–3373.

[46] J. I. Pankove (Ed.), Electroluminescence, Springer Berlin Heidelberg, 1977.

[47] Y. Shu, B. S. Fales, W.-T. Peng, B. G. Levine, *Understanding nonradiative recombination through defect-induced conical intersections*, The Journal of Physical Chemistry Letters 8 (17) (2017) 4091–4099.

[48] W. W. Moses, et al., *Scintillator non-proportionality: Present understanding and future challenges*, IEEE Transactions on Nuclear Science 55 (3) (2008) 1049–1053.

[49] J. Allison, et al., *Recent developments in Geant4*, Nuclear Instruments and Methods in Physics Research Section A: Accelerators, Spectrometers, Detectors and Associated Equipment 835 (2016) 186–225.

[50] S. Agostinelli, et al., *Geant4—a simulation toolkit*, Nuclear Instruments and Methods in Physics Research Section A: Accelerators, Spectrometers, Detectors and Associated Equipment 506 (3) (2003) 250 – 303.

[51] B. Herold, *Simulation and measurement of optical background in the deep sea using a multi-PMT optical module*, PhD thesis, Friedrich-Alexander-Universität Erlangen-Nürnberg (FAU) (2017).

[52] W. R. Leo, Techniques for Nuclear and Particle Physics Experiments, Springer Berlin

Heidelberg, 1994.
[53] I. Zvara, P. Povinec, I. Sykora, M. Sakanoue, *Determination of very low levels of radioactivity (technical report)*, Pure and Applied Chemistry 66 (12).
[54] ProSpect Gamma Spectroscopy Software - User's Manual, Canberra, 2012.
[55] J. K. Shultis, R. E. Faw, Fundamentals of Nuclear Science and Engineering Third Edition, CRC Press, 2016.
[56] A. S. Singh, A. G. Wright, *The determination of photomultiplier temperature coefficients for gain and spectral sensitivity using the photon counting technique*, IEEE Transactions on Nuclear Science 34 (1) (1987) 434–437.
[57] *National nuclear data center- chart of nuclides*, `https://www.nndc.bnl.gov/chart/`.
[58] A. Obermeier, *The fluorescence yield of air excited by electrons measured with the AIRFLY experiment*, Master's thesis, Universität Karlsruhe (2007).
[59] R. Parmar, R. S. Kundu, R. Punia, N. Kishore, P. Aghamkar, *Fe2O3 modified physical, structural and optical properties of bismuth silicate glasses*, Journal of Materials 2013 (2013) 1–5.
[60] H. Richter, B. P. Rand, Organic Solar Cells: Fundamentals, Devices, and Upscaling, Pan Stanford, 2014.
[61] RIGOL, *DG1000Z series datasheet*. URL `http://beyondmeasure.rigoltech.com/acton/attachment/1579/f-033c/0/-/-/-/-/file.pdf`
[62] F. de Chaffaut, *The luminescence decay time of air and nitrogen-oxygen mixtures excited by alpha particles*, IEEE Transactions on Nuclear Science 19 (3) (1972) 112–118.
[63] J. Sand, et al., *Radioluminescence yield of alpha particles in air*, New Journal of Physics 16 (5) (2014) 053022.
[64] C. Thompson, E. Barritt, C. Shenton-Taylor, *Predicting the air fluorescence yield of radioactive sources*, Radiation Measurements 88 (2016) 48–54.
[65] P. Lecoq, A. Gektin, M. Korzhik, *Charged hadron radiation damage of scintillators*, in: Inorganic Scintillators for Detector Systems, Springer International Publishing, 2016, pp. 253–280.
[66] R. Abbasi, et al. (IceCube Collaboration), *Calibration and Characterization of the IceCube Photomultiplier Tube*, Nucl. Instrum. Meth. A618 (2010) 139–152, Preprint 1002.2442.
[67] N. Stanisha, *Characterization of low-dT non-poisson noise in the IceCube neutrino detector*, Bachelor Thesis, Schreyer Honors College (2014).
[68] D. F. Heereman, *HitSpooling: An Improvement for the Supernova Neutrino Detection System in IceCube*, PhD Thesis, Université Libre de Bruxelles (2015).

Acknowledgements
- *Agradecimientos* -

First, I want to thank my advisor Prof. Alexander Kappes for giving me the opportunity to work in this amazing group and the possibility to do research on a very exciting topic. Thank you for the constant support, advice and infinite patience.
I would also like to thank my second supervisor, Dr Carlos Guerrero Sánchez, who has kindly offered me his support despite the distance.
I am immensely grateful to Lew Classen, who taught me everything. Also, thank you and Cristian Lozano for proofreading most of this thesis. You both have always had an open ear for my - most of the time rather dumb - questions.
There are many people that helped me in the course of the last year. I would like to express my deepest gratitude to Prof. Alfons Khoukaz, Prof. Dieter Frekers, Volker Hannen, Oleg Kalekin, Pawel Mekarski, Anna Pollmann, Daniel Winzen and Michael Larson.
Furthermore, I want to thank all the working group[1]. You are truly awesome people, in spite of the fact that you are bad at Poker... and you still beat me.

Por último, pero no menos importante, quiero agradecer infinitamente a mi familia. A mis padres, Ana María y Bernhard, por su constante apoyo durante mis estudios. Siempre han sido un pilar fundamental en mi vida. También quiero dar gracias a Ani Cabello Zanahoria Lechuga Tomate, mi tío Martín y a Pilar, quienes a pesar de la lejanía siempre han estado a mi lado.

...und ich danke Franz Unland für die ganzen Pizzen.

[1] ...everyone is so nice...